THESIS FOR THE DEGREE OF DOCTOR OF PHILOSOPHY

Development, Implementation, Validation and Applications of a Method for Simulation of Damaged and Intact Ships in Waves

MARTIN SCHREUDER

Department of Shipping and Marine Technology

CHALMERS UNIVERSITY OF TECHNOLOGY

Gothenburg, Sweden 2014

Development, Implementation, Validation and Applications of a Method for Simulation of Damaged and Intact Ships in Waves
MARTIN SCHREUDER
ISBN 978-91-7385-972-1

Doktorsavhandlingar vid Chalmers tekniska högskola
Ny serie nr 3653
ISSN 0346-718X

Department of Shipping and Marine Technology
Chalmers University of Technology
SE-412 96 Gothenburg
Sweden
Telephone + 46 (0)31-772 1000

Printed by Chalmers Reproservice
Gothenburg, Sweden 2014

To Sara

Development, Implementation, Validation and Applications of a Method for Simulation of Damaged and Intact Ships in Waves

MARTIN SCHREUDER
Department of Shipping and Marine Technology, Chalmers University of Technology

Abstract

The safety of ships at sea is a key aspect of shipping. Tragic passenger vessel accidents during the years motivates that large effort is spent on understanding the mechanisms of survivability of damaged ships. In the past few decades the development and use of numerical tools have resulted in a steady increase of the understanding and ability to assess these complex mechanisms.

This thesis describes the mathematical model and numerical implementation of a tool for assessment of the behavior of damaged or intact ships in a seaway. It includes three validation studies, where the simulation results are compared to physical scale model tests. It also includes four applied studies.

The mathematical model for ship motions is based on potential flow theory and a hybrid method often referred to as non-linear strip method. The hydrodynamic radiation and diffraction forces are based on linear theory. The forces are transferred from the frequency domain to the time domain by the Impulse Response Function concept. The forces from the incident waves are treated in a non-linear manner through body-exact pressure integration. A damage opening is defined through a grid of points and the flow of water through each grid point is determined through a formulation based on the Bernoulli equation. The behavior of flooded water is based on quasi-static assumptions where the floodwater surface is horizontal. The impact of viscosity on roll damping is treated through coefficients determined through experimental roll decay tests.

The first validation study concerns capsize of a damaged Ro-Pax ship in waves, the second concerns progressive flooding of a barge with complex internal layout and the third study concerns parametric rolling of an intact container ship. The first two studies show a good agreement between simulations and experiments. The third study shows that the phenomenon of parametric roll is captured in the simulations but also that there are large discrepancies in roll amplitude for some of the tested cases.

The first two conducted application studies are extensions of the validation studies for the damaged Ro-Pax and the containership sustaining parametric roll. The third presented application study refers to the modeling of the damage opening due to ship-to-ship collision by a FEM simulation procedure. Finally, the fourth conducted application study includes an accident investigation by use of the developed software tool.

It is concluded that the tool can be used in many applications of practical interest in present stage of implementation. Opportunities for development of the tool to further increase the applicability and validity are also discussed.

Acknowledgments

I would like to express my gratitude to my supervisor Carl-Erik Janson for his support, especially for his dedication and guidance during the finalization of my thesis. I would also like to thank my previous supervisor Olle Rutgersson and also all colleagues, at the department and elsewhere, for creating a nice working environment the past years.

Nomenclature

$A_{ii}, A_{ij}, A(\omega)$	:	3-dimensional added mass coefficients
$A_{ij}^{\infty}, a_{ij}^{\infty}$	:	Added mass coefficients at infinite frequency
a_{ii}, a_{ij}	:	2-dimensional added mass coefficients
a_h, a_v	:	Instantaneous horizontal and vertical particle acceleration of the incident wave
$\bar{a}_h$,$\bar{a}_v$	:	Effective spatial mean accelerations of the incident wave
$B_{ii}, B_{ij}, B(\omega)$	:	3-dimensional damping coefficients
b_{ii}, b_{ij}	:	2-dimensional damping coefficients
$B_{ij}^{\infty}, b_{ij}^{\infty}$	:	Damping coefficients at infinite frequency
b_e	:	Effective hydrodynamic half beam of ship section
C_d	:	Discharge coefficient
CG	:	Center of gravity of intact ship
cg	:	Center of gravity of flooded water
cgx_a	:	Co-ordinate of cg in system a
d	:	Draught of intact ship in calm water
d_e	:	Effective hydrodynamic draught of ship section
F_i^{diff}	:	Diffraction forces and moments
F_i^{FK}	:	Froude-Krylov forces and moments
F_3^g	:	Ship weight
F_i^{rad}	:	Radiation forces and moments
F_i^{fw}	:	Forces and moments from flooded water
F_i^v	:	Viscous damping forces and moments
F_i^p	:	Forces and moments due to pressure loss over damage opening
Fn	:	Froude number
g	:	Gravitational acceleration
H_s	:	Significant wave height
I_4, I_5, I_6	:	Mass moment of inertia for roll, pitch and yaw respectively
i, j	:	Indices for ship motion, 1=surge, 2=sway, 3=heave, 4=roll, 5=pitch, 6=yaw
KG	:	Vertical center of gravity of intact ship
K_{ij}	:	3-dimensional kernel function
k_{ij}	:	2-dimensional kernel function

k	:	Wave number
$k_{x\prime}, k_{y\prime}, k_{z\prime}$	:	Radius of mass moment of inertia in body fixed coordinate system
M^s	:	Generalized mass matrix of intact ship
M^{fw}	:	Generalized mass matrix of flooded water
m	:	Mass of intact ship
m^{fw}	:	Mass of floodwater in a compartment
$\boldsymbol{n}$	:	Normal vector of hull
p	:	Fluid pressure
p_{atm}	:	Atmospheric pressure
T	:	Euler angle transformation matrix
T_{eg}	:	Natural period of roll
T_p	:	Peak period
t, τ	:	Time
$\boldsymbol{u}$	:	Local velocity of hull
v_h, v_v	:	Instantaneous horizontal and vertical particle velocity of the incident wave
$\bar{v}_h, \bar{v}_v$	:	Effective spatial mean velocities of the incident wave
$\boldsymbol{v}$	:	Fluid velocity vector
α	:	Linear roll damping coefficient
β	:	Quadratic roll damping coefficient
γ	:	Peak enlargement factor
$\eta_{1..6}$	:	Ship motions, 1=surge, 2=sway, 3=heave, 4=roll, 5=pitch, 6=yaw
λ	:	Wavelength
μ	:	Heading angle
$\xi, \hat{\xi}$	:	Free surface elevation, wave amplitude
ρ	:	Fluid density
$\phi_{(I,D,R)}$	:	Fluid velocity potential (Incident, Diffraction, Radiation)
χ	:	Velocity potential normalized with respect to displacement
ψ	:	Velocity potential normalized with respect to velocity
ω	:	Wave angular frequency
ω_e	:	Frequency of encounter

ω_{eg} : Natural frequency of roll

All vectors are expressed by bold font.
All quantities are expressed in SI units unless otherwise stated.
Trapezoidal integration is used unless otherwise stated.

Contents

1 Introduction 1

1.1 Background/Motivation of work 1

1.2 Objectives 2

1.3 Literature survey 2

1.4 Focus and limitations 4

1.5 Scientific contribution 4

1.6 Outline and summary of the thesis 4

2 Theory 9

2.1 Potential flow 9

2.2 Potential flow – linear approach 11

2.3 Hydrodynamic forces in the frequency domain – linear strip theory 14

2.4 Hydrodynamic forces in the time domain 15

3 Method 19

3.1 Coordinate systems and kinematics 19

3.2 Geometry of the ship 20

3.3 Waves 21

3.4 Equations of motion 22

3.5 Forces and moments 25

3.5.1 Radiation forces 25

3.5.2 Wave diffraction forces 26

3.5.3 Froude-Krylov forces 28

3.5.4 Viscous damping forces 31

3.6 Damage simulation 31

3.6.1 Compartments 31

3.6.2 Damage openings and flooding process 31

3.6.3 Progressive flooding 33

3.6.4 Excitation forces from floodwater 34

3.6.5 Inertia forces from floodwater 34

3.6.6 Pressure gradient over damage opening 35

3.7 Solution method and time stepping 36

4 Validation studies 37

4.1 Ro-Pax capsize in waves 37

4.2 Progressive flooding 42

4.3 Parametric roll 51

5 Applied studies 61

5.1 Ro-Pax capsize in waves 61

5.2 Parametric roll 66

5.3 Collision survivability in waves 73

5.4 Accident investigation 91

6 Discussion 101

7 Further work 103

References 105

Appendix 1 111

Appendix 2 115

1 Introduction

1.1 Background/Motivation of work

The safety of ships is a primary concern for ship designers, ship operators, regulatory authorities and the general public. The importance of ship safety is linked ultimately to the protection of human lives. It is also of importance with respect to protection of the economic value of cargo and ship and to protection of the environment from e.g. oil spill. Tragic passenger vessel accidents the past few decades have put a strong focus on ships ability to stay afloat and upright after flooding due to hull damage within the research community.

A special interest has been taken to the RoPax ship, a ship type that features roll-on/roll-off capacity for private cars and commercial vehicles as well as accommodation spaces for a large number of passengers. The RoPax ship is a very successful concept commercially due to its flexibility and efficient cargo handling. The typical arrangement on a RoPax is a large vehicle deck without watertight subdivisions serving as freeboard deck below which machinery/technical equipment is situated in subdivided spaces, possibly together with a narrow centrally placed lower ro-ro deck and/or passenger accommodation. The main part of the accommodation spaces resides in the superstructure above the freeboard deck and above any additional higher ro-ro deck. Although very successful the combination of large number of passengers and a typical and dramatic behaviour following flooding of the vehicle deck, i.e. rapid capsize of the ship, poses a high safety risk for the RoPax ship type.

The loss of MS Herald of Free Enterprise in 1987 and MV Estonia in 1994 are two examples of disastrous RoPax ship accidents. In both cases the ship developed a large list angle in very short time due to flooding of the vehicle deck. At large list angles safe and orderly abandoning of the ship is impossible and reaching this state in less time than needed for abandoning will have very severe consequences.

In 1997 the International Maritime Organization **(**IMO) adopted a methodology for evaluating and mitigating risks through Formal Safety Assessment (FSA). FSA is a structured and systematic methodology with the purpose of being a tool to aid the development and evaluation of regulations for maritime safety, Soares et al. (2009). In 2008, a FSA study on RoPax ships, carried out within the research project SAFEDOR (2005-2008) was submitted to IMO (MSC 2008a,b). The scope of the study was to investigate credible accident scenarios during RoPax operations based on worldwide accident experience, relevant past studies and judgement. Over all conclusions from the risk evaluation was that focus in order to reduce the risk of loss of life should be placed on (in order of importance):

- Measures related to improved damage stability and survivability after flooding.
- Measures related to improved navigational safety.
- Improved evacuation arrangement.
- Improved fire prevention and protection.

It was furthermore identified that rapid capsize as a consequence of various accident categories is the main contributor to ship losses and a cause of a large number of fatalities.

The importance of the time evolution alone makes it impossible to make a proper assessment of flooding events with traditional hydrostatic tools. The two accidents above also incorporate flooding above the mean water level which can only be explained and assessed through consideration of dynamic effects.

1.2 Objectives

The objective of the current thesis is to develop a numerical tool able to study, in the temporal domain, the process of flooding of a ship which has lost its water tight integrity due to grounding, collision or any other event resulting in a hull breach and to assess the response of the ship including full capsize and possibly until the ship leaves the surface of the sea.

In contrast to static damage stability calculations the present approach shall automatically and in a realistic manner consider intermediate stages of flooding which may result in a more dangerous situation e.g. larger heel angles than the final equilibrium. Progressive flooding i.e. flooding to and from spaces or compartments without direct connection to the sea e.g. through open doors shall also be possible to assess.

The tool shall further be able to consider the influence of waves in a damage scenario, both with respect to flooding process and ship response. In order to achieve this, the method needs to be non-linear at least in the sense of capturing the rightening abilities of a ship at large heel angles. The introduction of this non-linear effect makes it possible to study also pertinent dynamic stability problems for intact ships i.e. parametric rolling and direct loss of stability. It will also be a trivial task to implement non-linear damping which can be significant for the rolling motion of a ship.

To achieve the objectives a non-linear time domain strip theory approach together with formulations for handling flooding into and within the ship is employed. A detailed description of the method, hereafter called SIMCAP, is found in the following chapters.

1.3 Literature survey

The assessment of the behavior of damaged ships in waves through numerical simulation has been a very active field of research the last few decades. An important source of information on this and related research can be found in the series of proceedings from the *International Conference on the Stability of Ships and Ocean Vehicles (STAB)* and *International Ship Stability Workshops (ISSW)* which are currently publically available for download at www.shipstab.org. Related research is also summarized in proceedings of the International Towing Tank Conference e.g. ITTC (2008) and ITTC (2011).

In 1962 Cummins presented a method to describe the linear radiation and diffraction forces in the time domain. This method provides the possibility for development of time domain numerical tools for seakeeping assessments where non-linear effects can be introduced, e.g. Journeé (1993), de Kat et al. (1994), Matusiak (2003) and Fossen (2005). The method is very effective for practical applications compared to more sophisticated potential flow or CFD methods due to relatively low computational effort.

In the 1990's the development of time domain tools for the assessment of damaged ships in waves started. In 2008 four tools referenced below participated in a benchmark study on a damaged Ro-Pax ferry, presented in ITTC (2008). The tools share some basic features with the present SIMCAP tool i.e. linear potential flow approach for description of the radiation and diffraction forces and incident wave, and non-linear Froude-Krylov forces. They also share the Bernoulli in- and outflow approach. In Turan (1993) a numerical tool for the coupled roll-sway-heave motions in beam seas was introduced. The floodwater is assumed to be horizontal and the trim can be accounted for quasi-statically. The development of this tool has served as a base for the PROTHEUS simulation tool developed at the University of Strathclyde, with capabilities of six degrees of freedom simulations of arbitrary wave directions, see e.g. Jasionowski and Vassalos (2001). In Zaraphonitis et al. (1997) a tool for damaged ship assessment in six degrees of freedom was presented. The tool, named CAPSIM, is based on a 3-D mathematical model and is further developed at the National Technical University of Athens, see e.g. Spanos and Papanikolaou (2001). The ship and floodwater are described by a two mass system and the center of gravity of the flooded water can move along a predefined surface. Thus the phenomenon of sloshing is to some extent accounted for. This tool is also capable of progressive flooding assessments. The numerical tool FREDYN has mainly been developed at the Maritime Research Institute Netherlands (MARIN), see de Kat et al. (1994) and Van't Veer et al. (2004). It has the capability of progressive flooding and also maneuvering in waves. Instituto Superior Técnico has developed a simulation tool; see e.g. Santos and Guades Soares (2003), capable of progressive flooding and where the water on deck is modelled using shallow water theory.

The phenomenon of parametric roll has been recognized and investigated both by numerical and experimental models by naval architects for more than fifty years (Paulling 2006). All tools mentioned above have the capacity to study this non-linear phenomenon and have also been used for this purpose. This phenomenon has also been investigated through several other numerical tools, see e.g. Hua et al. (2006), Umeda et al. (2008), Bulian and Francescutto (2008), Vidic-Perunovic and Jensen (2009), and Neves et al. (2009), which all participated in the benchmark study on parametric rolling described in Spanos and Papanikolaou (2009a).

It is of paramount importance to validate numerical tools used to assess the behavior of intact and damaged ships in waves. Validation is typically done through comparison with dedicated scale model tests. There are also examples of full scale tests and experimental measurements e.g. Ruponen (2010), with full scale progressive flooding including air compression effects, and Hua et al. (2006), where the roll motions measured during a parametric roll incident was reported. The model tests by SSPA reported in Rask (2010), Allenström and Thorsson (2007)

and Allenström (2007) were used for the validation of SIMCAP regarding flooding and capsizing of RoPax ships. The model tests reported in Ruponen (2006), by the Ship Laboratory at Helsinki University of Technology (now Aalto University) were used for the validation of progressive flooding. The model tests carried out at CEHIPAR (El Pardo, Spain) and the tests carried out at INSEAN (Rome, Italy), both used in the benchmark in Spanos and Papanikolaou (2009a), were used for the validation of parametric roll.

1.4 Focus and limitations

The focus is to assess the behavior of the damaged ship and the flooding process after the hull integrity has been breached. In one of the studies however SIMCAP is linked to another model which simulates collision events between two ships through explicit finite element analysis (FEA). The FEA generates a damage opening geometry as input to the SIMCAP model.

Active response to an accident scenario such as maneuvering, counter flooding or measures to contain the damage e.g. closing of water tight doors, is not considered.

With the exception of an intact container ship and a simple barge only RoPax ships have been studied in this thesis. The only principal limitation on ship type is however that the hull is of displacement type and slender (sufficiently low beam to length ratio). These limitations are inherited from the frequency domain strip theory formulation.

Maneuvering of the ship is not studied. A fixed yaw angle is used in all applied studies in the thesis. Most studies also assume zero forward speed and beam waves, which can be considered as a worst case scenario. Prescribed forward speed and yaw motion to resemble a ship route/maneuvering is however possible. Only long crested waves is implemented in the present method and shifting of cargo is not considered. Further simplifications and limitations related to the chosen method are discussed in chapters 2 and 3.

1.5 Scientific contribution

A state of the art nonlinear time domain strip method for the simulation of damaged and intact ships in waves has been developed. The implementation together with validation and applications are presented and discussed.

Consequences of approximations and assumptions are discussed based on a detailed knowledge of the implementation of the method together with results from validations and applied case studies.

Computed results are explained resting on a full insight to the implemented theory together with knowledge of the real physics to be simulated. Knowledge gained through the analysis of the results contributes to the understanding of physical mechanisms related to the investigated scenarios.

An interdisciplinary simulation procedure, including the chain of events of ship-to-ship collision, flooding and ship capsize in waves, is presented together with sensitivity analyses and applied studies.

The impact of the width of side casings on capsize vulnerability of a Ro-Pax ship is studied and discussed.

The physical mechanisms of progressive flooding are described in some detail, together with consequences of limitations of the numerical model, based on the analysis of simulation results.

Several physical mechanisms pertaining to parametric roll are identified through the analysis of simulation results. They are also discussed in a comparison between scale model tests and simulations.

The final stages of a full capsize, including flooding of the superstructure, of a Ro-Pax ship is simulated and analysed.

1.6 Outline and summary of the thesis

This thesis presents the development, validation and applications of a time domain simulation tool for assessment of the behavior of damaged and intact ships in waves, called SIMCAP. The hydro-mechanic theory is outlined in chapter 2 and serves as a background for the method description in chapter 3 where the implementation of the tool is detailed. Three different validation studies and four application studies are presented in chapters 4 and 5 respectively.

The developed tool, SIMCAP, is based on a hybrid approach where the hydrodynamic radiation and diffraction forces are based on linear potential flow theory in the time domain while the excitation forces from the incident wave pressure are treated non-linearly though integration over the wetted hull surface. The latter makes it possible to retain all hydrostatic stability properties of a damaged ship when the ship is flooded. Through a quasi-stationary flooding process with a versatile and robust damage opening definition and through the inclusion of floodwater inertia in the equations of motion the most important mechanisms of the dynamic event of ship flooding in waves are included in the tool.

Section 4.1 describes a validation study where simulations of a damaged RoPax ship have been compared to model experiments, Rask (2010). The damage case is a traditional SOLAS two compartment damage where the ship is subjected to beam seas of different wave heights represented by a Jonswap spectrum. If the waves are sufficiently high water will accumulate on the vehicle deck which eventually leads to capsize of the ship. The time to capsize, from the initiation of the test/simulation, is used as the indicator for the validation. A plot of significant wave height versus time to capsize, show a high degree of agreement between simulations and tests. Prior to the simulations roll damping coefficients were determined

through a comparison with a roll decay test of the intact ship model. In section 5.1 the same ship has been investigated in a parametric study where an additional damage case, involving progressive flooding, was studied in conjunction with the fitting of side casings of variable breadth. The results show a substantial increase in the time to capsize when the casing breadth is increased from one to two meters, for both damage cases. Also some details of the simulations are discussed in terms of the governing physics.

Section 4.2 describes a validation study of the progressive flooding capabilities of SIMCAP where simulations have been compared to model tests, Ruponen (2006) in calm water of a barge for two different damage scenarios. The subdivision and internal openings connecting the spaces within the barge where designed to resemble progressive flooding of a passenger ship. In the model tests the time evolution of sinkage, trim and heel were measured as well as the height of flooded water in pertinent compartments. Specifically tailored experiments, Ruponen (2006), were made to produce discharge coefficients which were used in the simulations. The first damage scenario consists of a hull breach in one double bottom compartment with progressive flooding into seven compartments on two deck levels. In one of the compartments air was trapped. This effect cannot be captured by the simulation. The air entrapment influences the scenario as a whole and clear discrepancies can be seen between the results of experiment and simulation. It is however possible to describe and explain the physics governing the simulation result and the comparison between test and simulation is quite useful, thanks to rather than in spite of the discrepancies. In the second scenario a total of six compartments are flooded through a side damage. All compartments can be considered fully ventilated and there is no entrapment of air. The correspondence between test and simulation results is high. Gao et al. (2011) present a simulation of this scenario based on the Navier-Stokes equations. These results show a slightly better agreement at the cost of simulation time with a factor of about 10^4. However, even though the overall results are not significantly improved, these methods can resolve details of the flow not captured by SIMCAP.

The non-linear restoring needed for the simulation of a damaged ship also pave the way for studies of non-linear behavior of intact ships, for regular synchronous motions and also for specific stability issues such as parametric roll. In section 4.3 a validation study and in section 5.2 a parameter study, of parametric roll are described. In the validation study, simulations are compared to 20 model tests of a container ship, Spanos and Papanikolaou (2009a). The tests comprise variations in wave height and period for regular and irregular seas, ship speed, heading and loading condition. Qualitatively SIMCAP was able to reproduce the occurrence of parametric roll for the majority of the cases, albeit not all. Quantitatively, when steady state roll amplitudes were compared, the results were quite scattered. In order to find the reasons for these discrepancies a parametric investigation, described in section 5.2, was carried out where the wave height and period were varied systematically. In this manner regions of occurrence (and roll amplitudes) were produced around eight of the discrete test cases of the validation study. These test cases, all in regular waves, contained some of the best and worst results of the validation study. In the analysis of the results several physical mechanisms pertinent to parametric roll could be identified and possible explanations to the discrepancies

are discussed. A major result was that the boarders of occurrence could be very sharp i.e. for a very small change in the investigated parameters the result can change from non-occurrence to parametric roll with extreme roll amplitudes. This could explain the result with the largest discrepancy in the validation study.

In section 5.3, collision survivability in waves, an interdisciplinary calculation procedure and results of several investigations where the procedure has been used is presented and discussed, Schreuder et al. (2012). The investigations involve the chain of events of ship-to-ship collision, flooding and time to capsize. The structural mechanics of the collision are assessed through finite element method simulations which mimic the rupture and collapse of the struck ship, resulting in a hull breach. Information of the resulting damage opening is transferred to SIMCAP for flooding and capsize analysis. The investigations include a convergence study where the properties of the damage opening definition is analyzed, a case study where a RoPax-ferry have been struck by a similarly sized ship and were a range of parameters have been systematically varied. Finally, a sensitivity analysis where the impact of the number of wave seeds used to represent a sea state is investigated. In the convergence study it was concluded that the damage opening definition is robust and well fitted for its purpose. In the case study, capsize bands were produced through collection of the time to capsize for the studied parameters. The qualitative nature of the capsize bands corresponds with the expected results, i.e. the existence of a limit wave height below which capsize did not occur is demonstrated as well as the steady decrease of the time to capsize as the wave height increases. The influence of ship heading, damage case and loading condition on time to capsize is also presented and discussed. From the sensitivity study it is concluded that the use of 20 wave seeds to represent a sea state, which is used in section 4.1, seem to be appropriate regarding balance between statistical accuracy and computational cost. A study not conducted by the author but where SIMCAP has been utilized, Hogström and Ringsberg (2012), is also briefly presented and discussed. In this study a range of damage openings were produced based on variations of parameters in the collision scenario. Through SIMCAP simulations, a capsize band was produced for each opening. The results are analyzed through inspection of the opening and corresponding capsize band in an effort to reveal the impact of damage opening shape, size and location on the properties of the capsize band.

Section 5.4 describes the use of SIMCAP in a project where the sinking sequence of m/v Estonia was studied, Källström et al. (2008). The flooding was assumed to be initiated through the bow ramp opening as the ship was sailing at full speed in close to head waves. To include the effect of ship speed in the flooding calculation an ad-hoc formulation was added which resulted in a reasonable agreement with model tests conducted within the project, Allenström and Thorsson (2007) and Allenström (2007). At a later stage of the accident, when 2500 tonnes of water had entered the car deck and with about 40° of heel, other openings of the ship is subjected to flooding. At this stage ship blackout and a beam seas orientation with zero forward speed is assumed. A simulation where the ship, including super structure, is flooded until complete capsize and sinking is presented. The result is analyzed through inspection of snap shots from different instants of the simulation and several different mechanisms of the scenario are discussed and explained.

2 Theory

If the viscosity of water can be neglected and the flow is assumed to be irrotational and incompressible, the sea keeping problem can be described and assessed through potential flow theory. The above assumptions are very common for numerical sea keeping assessments and have proven to provide accurate results regarding the motions of the ship, with the exception of the roll motion close to resonance where viscous effects have a significant relative impact due to low potential damping. This can however be treated separately through an empirical addition to the roll damping, as described in section 3.5.4 of chapter 3.

In this chapter potential flow theory for assessment of ship motion is outlined. The chapter is intended to serve as a background to chapter 3 where SIMCAP is described in detail. The present chapter does not treat the effects of the loss of water tight integrity of the ship, which is treated in its entirety in chapter 3.

The first section of the chapter outlines the non-linear potential flow problem. In the second section the problem is linearized and in the third section the classical strip theory for the steady state frequency domain is briefly outlined. In the fourth section the transfer of the linear frequency domain problem to the time domain is outlined. For a more comprehensive description of potential flow theory Newman (1977), Faltinsen (1990) or Lewandowski (2004) are recommended.

2.1 Potential flow

If the sea water is considered to be inviscid, incompressible and irrotational it is convenient to use a scalar velocity potential ϕ defined to describe the fluid velocity vector $\boldsymbol{v}(x, y, z, t) = (u, v, w)$ at time t. The velocity potential is described in a right handed Cartesian earth fixed reference frame. The xy plane coincides with the calm water surface. The z-axis is directed upwards and the x-axis in the direction of incident wave propagation, such that:

$$\boldsymbol{v} = \nabla\phi = \left(\frac{\partial\phi}{\partial x}, \frac{\partial\phi}{\partial y}, \frac{\partial\phi}{\partial z}\right) \tag{2.1}$$

Now the continuity equation for an incompressible flow, $\nabla \cdot \boldsymbol{v} = 0$, will lead to the Laplace equation:

$$\nabla^2\phi = 0 \tag{2.2}$$

which is the governing equation for the flow in a fluid domain and together with proper boundary conditions can be solved for the velocity potential. The boundaries of the fluid domain is composed of the submerged hull surface, the sea bed, the free surface and a vertical boundary connecting free surface and sea bed far away from the ship.

The boundary condition on the hull surface can be described as a kinematic condition:

$$\frac{\partial \phi}{\partial n} = \boldsymbol{u} \cdot \boldsymbol{n} \tag{2.3}$$

where $\partial/\partial n$ represent differentiation with respect to the normal $\boldsymbol{n}$ of the hull surface and $\boldsymbol{u}$ is the local velocity of the hull (i.e. all rigid body motions are included in $\boldsymbol{u}$**)**. Thus (2.3) states that there is no fluid flow across the hull surface i.e. the hull is impermeable.

A similar boundary condition holds for the sea bed where the normal velocity must be zero:

$$\frac{\partial \phi}{\partial n} = 0 \tag{2.4}$$

The vertical far field boundary is located at an infinite distance from the ship. This ensures that the velocity potential is not affected by the presence of the ship i.e. the potential is defined by the incoming waves alone at this boundary.

At the free surface two boundary conditions will be implied, kinematic and dynamic. The kinematic condition states that a fluid particle on the free surface stays on the free surface. Let us define the free surface elevation by $z = \xi(x, y, t)$. Now let the function $F = z - \xi(x, y, t) = 0$ define the position of a particle on the free surface. If the particle is to stay on the free surface the substantial derivative of F must also be zero. Thus:

$$\frac{DF}{Dt} = \frac{\partial F}{\partial t} + \nabla\phi \cdot \nabla \mathrm{F} = 0 \tag{2.5}$$

i.e.

$$\frac{\partial \xi}{\partial t} + \frac{\partial \phi}{\partial x}\frac{\partial \xi}{\partial x} + \frac{\partial \phi}{\partial y}\frac{\partial \xi}{\partial y} - \frac{\partial \phi}{\partial z} = 0 \qquad \text{on} \qquad z = \xi(x, y, t) \tag{2.6}$$

The pressure p can be found through the Bernoulli equation which can be expressed:

$$\frac{(p - p_{atm})}{\rho} + gz + \frac{\partial \phi}{\partial t} + \frac{1}{2}(\nabla\phi)^2 = 0 \tag{2.7}$$

The dynamic free surface condition states that there is no pressure gradient over the free surface i.e. the pressure on the free surface is equal to the atmospheric pressure p_{atm}, herein defined as a constant reference pressure equal to zero, and from equation (2.7) we can write:

$$g\xi + \frac{\partial \phi}{\partial t} + \frac{1}{2}(\nabla\phi)^2 = 0 \qquad \text{on} \qquad z = \xi(x, y, t) \tag{2.8}$$

When the velocity potential is known forces on the hull can be calculated through Bernoulli's equation and pressure integration over the hull surface and by using Newton's second law the motion of the ship can be obtained. In practice however attaining the velocity potential is not a straight forward task and will also be computationally time consuming. The problem can instead be solved by adopting a linearization of the above equations and making an assumption that the flow around the ship is essentially two dimensional. This leads to the well known frequency domain strip theory for ships which is briefly outlined in sections 2.2 and 2.3.

2.2 Potential flow – linear approach

In a linear approach to the seakeeping problem it is assumed that the wave height and the oscillatory motions of the ship are small enough to justify a linear formulation of the hydrodynamic problem.

The ship motion problem can then be described by a linear superposition of two separable problems: the diffraction boundary value problem and the radiation boundary value problem. Also, the responses of the ship in an irregular seaway can be described by linear superposition of the responses to the regular wave components.

In the diffraction problem waves unaffected by the ship, incident waves, are encountering a ship that is considered restrained from oscillating and the waves will be disturbed or diffracted by the presence of the ship. In the radiation problem the ship is undergoing oscillatory motions in initially calm water and waves will be generated by the ship.

The velocity potential of the linear problem can be described as the sum of three potentials:

$$\phi = \phi_I + \phi_R + \phi_D \tag{2.9}$$

where:

ϕ_I: The incident wave potential representing the incoming undisturbed waves (Froude-Krylov waves)

ϕ_R: The radiation potential representing the waves that will be generated by the oscillating ship.

ϕ_D: The diffraction potential representing the disturbance of the incident waves due to the presence of the ship.

With above definition of the velocity potential the kinematic boundary condition on the hull surface can be decomposed in:

$$\frac{\partial(\phi_I + \phi_D)}{\partial n} = 0 \tag{2.10}$$

which holds for the diffraction problem where the ship is considered fixed in space, and:

$$\frac{\partial \phi_R}{\partial n} = \boldsymbol{u} \cdot \boldsymbol{n} \tag{2.11}$$

for the radiation problem where the ship is oscillating in calm water without the presence of incident waves.

The sea bed condition is:

$$\frac{\partial(\phi_I + \phi_R + \phi_D)}{\partial n} = 0 \tag{2.12}$$

The far field conditions for the radiation and diffraction waves are:

$$\lim_{r\to\infty} \phi_R = \lim_{r\to\infty} \phi_D = 0 \tag{2.13}$$

where r is the horizontal distance from the ship.

The free surface conditions will, after a transfer to the mean free surface $z = 0$ (by Taylor series expansion) and omitting the higher order terms, reduce to:

$$\frac{\partial \xi}{\partial t} - \frac{\partial \phi}{\partial z} = 0 \qquad \text{on} \qquad z = 0 \tag{2.14}$$

for the kinematic boundary condition and:

$$g\xi + \frac{\partial \phi}{\partial t} = 0 \qquad \text{on} \qquad z = 0 \tag{2.15}$$

for the dynamic boundary condition.

The incident wave potential of linear, long crested and deep water waves propagating in the horizontal x direction can be derived from the Laplace equation, free surface conditions and sea bed condition and is described by (e.g. Faltinsen 1990):

$$\phi_I = \frac{g\hat{\xi}}{\omega} e^{kz} \sin(kx - \omega t) \tag{2.16}$$

where $k = \omega^2/g$ is the wave number and $\hat{\xi}$ is the wave amplitude. The sign and phase angle of ϕ_I (here positive and zero) can be chosen freely and will determine the direction of wave propagation.

The dynamic pressure can be found through the linearized Bernoulli equation, where the last term on the left side of equation (2.7) is omitted:

$$p = -\rho \frac{\partial \phi_I}{\partial t} = \rho g \hat{\xi} e^{kz} \cos(kx - \omega t) \tag{2.17}$$

and the water particle velocities through:

$$\frac{\partial \phi_I}{\partial x} = \omega \hat{\xi} e^{kz} \cos(kx - \omega t) \tag{2.18}$$

$$\frac{\partial \phi_I}{\partial z} = \omega \hat{\xi} e^{kz} \sin(kx - \omega t) \tag{2.19}$$

and accelerations:

$$\frac{\partial^2 \phi_I}{\partial x \partial t} = \omega^2 \hat{\xi} e^{kz} \sin(kx - \omega t) \tag{2.20}$$

$$\frac{\partial^2 \phi_I}{\partial z \partial t} = -\omega^2 \hat{\xi} e^{kz} \cos(kx - \omega t) \tag{2.21}$$

The wave elevation of the incident wave can be found combining equations (2.15) and (2.17) yielding:

$$\xi = \hat{\xi} \cos(kx - \omega t) \tag{2.22}$$

With the above linearized boundary conditions and the governing equation (2.2) the radiation and diffraction problems can be solved separately and by use of the linearized Bernoulli equation the pressure can be integrated over the surface of the ship to obtain the forces.

2.3 Hydrodynamic forces in the frequency domain – linear strip theory

Further simplifications will be achieved if the hydrodynamic problem is viewed as a superposition of two dimensional problems where the ship is subdivided into transverse sections or strips. By this the fluid flow out of the plane of the strips is neglected and the dimensions of the strips need to be small compared to the ship length i.e. the ship needs to be slender. The strip method is however well proven and provides results that are accurate enough for engineering purposes for a wide range of hull forms and sea states.

The radiation forces consist of one component proportional to the acceleration ($\ddot{\eta}$) of the ship and one component proportional to the velocity ($\dot{\eta}$) and can be expressed:

$$F^{rad}(\omega,t) = -A(\omega)\ddot{\eta}(\omega,t) - B(\omega)\dot{\eta}(\omega,t) \tag{2.23}$$

A and B are called the 3-dimensional hydrodynamic added mass and damping coefficients respectively and are dependent on the oscillation frequency ω. Note that eq. (2.23) is a simplified generic expression; A and B are different for different modes of motions and that there are hydrodynamic coupling terms between the different modes. This is described in more detail in sections 3.4 and 3.5.

A and B are obtained through integration of the sectional 2-dimensional coefficients, a and b, over the length of the ship according to appendix 1, where also effects of a steady forward ship speed U is included. There are different numerical techniques to solve the radiation problem to obtain the 2-dimensional added mass and damping coefficients. They can also be found through physical model experiments. One of the techniques to obtain the coefficients is to first derive an analytical expression for the potential for an oscillating semi-circular hull section shape and use conformal mapping to transform the solution to ship-like section shapes, Lewis method, see e.g. Lloyd (1989). Another method is to use a pulsating source technique where the boundary conditions will be satisfied on the actual shape of the sections, Franks method, see e.g. Faltinsen (1990).

The diffraction forces can also be obtained through the use of the hydrodynamic 2-D coefficients from the radiation force calculation and the relative motion hypothesis, see e.g. Journée and Adegeest (2003) or Newman (1977). In principle the accelerations and velocities of the water particles in the incident wave at the position of the fixed ship can be viewed, through a change of reference frame, as an oscillating ship in calm water and we obtain:

$$F^{diff}(\omega,t) = \int_L [a(\omega)\bar{a}(\omega,t) + b(\omega)\bar{v}(\omega,t)]dx \tag{2.24}$$

where $\bar{v}$ and $\bar{a}$ are the effective, spatially constant velocity and acceleration representing the motions of the water particles of the incident wave at the ship section. Note that the

diffraction forces have to be calculated for each section, before they are integrated over the length (L) of the ship, due to the variation of water particle motions along ship, as opposed to the rigid body motion of the ship itself in the radiation problem. Similar to eq. (2.23), eq. (2.24) is a generic expression described in more detail in sections 3.4 and 3.5.

In linear strip theory the forces due to hydrostatic restoring and incident wave excitation forces are expressed linearly through constant hydrostatic coefficients and the steady state ship motions can now be calculated by using Newton's second law with the restoring, incident wave, diffraction and radiation forces as external forces.

2.4 Hydrodynamic forces in the time domain

The objective of the present work is to solve a problem that has both a non-linear and transient character which makes it necessary to describe and solve the problem in the time domain. Cummins (1962) provides a method to describe the linear hydrodynamic forces in the time domain through convolution integrals containing the frequency dependent hydrodynamic coefficients. A summary of the derivation of the hydrodynamic forces in the time domain is presented below.

Consider a floating object as a linear system with translational and rotational motions as input and the reaction forces and moments from the surrounding water as output. Let the object be at rest when a displacement Δx is given to the object at a constant velocity V during the time Δt and $\Delta x = V \cdot \Delta t$.

During this displacement the surrounding water will start to move. For irrotational flow this motion can be described by a velocity potential ϕ proportional to V: $\phi = V \cdot \psi$, where ψ is the normalized velocity potential.

After the displacement, when the object is at rest, the surrounding water will continue to move which can be described by a velocity potential ϕ proportional to the displacement: $\phi = \Delta x \cdot \chi$, where χ is the normalized velocity potential.

Thus the displacement of the object does not only influence the motion of the surrounding water during Δt but also further on in time. Also the motions of the water during Δt would also be affected by any motion of the object before this time.

Arbitrary motion in time by the object can be described by a series of small displacement and the resulting velocity potential $\phi(t)$ of the surrounding water during the interval $(t_n, t_n + \Delta t)$ will be:

$$\phi(t) = \sum_{j=1}^{6} \left\{ V_{j,n} \cdot \psi_j + \sum_{k=1}^{n} \left[\chi_{j,k} \cdot V_{j,k} \cdot \Delta t \right] \right\} \tag{2.25}$$

where:

n	number of time steps	
t_0	time at which first displacement starts	
t_n	$= t_0 + n\Delta t$	present time
t_{n-k}	$= t_0 + (n-k)\Delta t$	historic time
$V_{j,n}$	j^{th} velocity component during latest time step, $(t_n, t_n + \Delta t)$	
$V_{j,k}$	j^{th} velocity component during historic time step, $(t_{n-k}, t_{n-k} + \Delta t)$	
ψ_j	normalized velocity potential caused by a displacement in direction *j* during latest time step	
$\chi_{j,k}$	normalized velocity potential caused by a displacement in direction *j* during historic time step	

Letting Δt go to zero yields:

$$\phi(t) = \sum_{j=1}^{6} \left\{ \dot{x}_j(t) \cdot \psi_j + \int_{-\infty}^{t} \chi_j(t-\tau) \cdot \dot{x}_j(\tau) \cdot d\tau \right\} \tag{2.26}$$

where $\dot{x}_j(t)$ is the j^{th} velocity component at time t.

The dynamic pressure in the water is:

$$p = -\rho \frac{\partial \phi(t)}{\partial t} \tag{2.27}$$

Integration of the pressure over the wetted part of the object will render the radiation forces and moments F_i^{rad}, $i = 1..6$. After some rearrangement, see Journée (1993) for a more complete derivation, F_i^{rad} can be expressed as:

$$F_i^{rad} = -\sum_{j=1}^{6} \left\{ J_{i,j} \cdot \ddot{x}_j(t) + \int_{0}^{\infty} K_{i,j}(\tau) \cdot \dot{x}_j(t-\tau) \cdot d\tau \right\} \tag{2.28}$$

where $J_{i,j}$ and $K_{i,j}$ contain the contribution from ψ_j and χ_j in the pressure integration.

Now, assuming the floating object will carry out a harmonic oscillation with unit amplitude in direction j, $x_j(t) = cos(\omega t)$, a substitution in (2.28) and some trigonometric rearrangement result into:

$$F_i^{rad} = \omega^2 \cdot \left\{ J_{i,j} - \frac{1}{\omega} \cdot \int_0^\infty K_{i,j}(\tau) \cdot sin(\omega\tau) \cdot d\tau \right\} \cdot cos(\omega t) + \\ + \omega \cdot \left\{ \int_0^\infty K_{i,j}(\tau) \cdot sin(\omega\tau) \cdot d\tau \right\} \cdot sin(\omega t) \tag{2.29}$$

The corresponding equation describing the radiation forces in the linear strip theory frequency domain is:

$$F_i^{rad} = \omega^2 \cdot \{A_{i,j}(\omega)\} \cdot cos(\omega t) + \omega \cdot \{B_{i,j}(\omega)\} \cdot sin(\omega t) \tag{2.30}$$

where $A_{i,j}$ and $B_{i,j}$ are the frequency dependent added mass and damping respectively.

Comparing the time domain equation (2.29) with the frequency domain equation (2.30) following relationships are found:

$$A_{i,j}(\omega) = J_{i,j} - \frac{1}{\omega} \cdot \int_0^\infty K_{i,j}(\tau) \cdot sin(\omega\tau) \cdot d\tau \tag{2.31}$$

$$B_{i,j}(\omega) = \int_0^\infty K_{i,j}(\tau) \cdot cos(\omega\tau) \cdot d\tau \tag{2.32}$$

Equation (2.31) is valid for any value of ω and evaluation at $\omega = \infty$ lead to:

$$J_{i,j} = A_{i,j}(\infty) \tag{2.33}$$

Furthermore, an inverse cosine Fourier transformation of (2.32) results in:

$$K_{i,j}(\tau) = \frac{2}{\pi} \int_0^\infty B_{i,j}(\omega) \cdot \ cos(\omega\tau) \cdot d\omega \tag{2.34}$$

which is the kernel function of the convolution in the radiation forces in equation (2.28).

The diffraction forces can be treated in an analogous manner where e.g. the incremental displacement Δx will represent the wave elevation, see e.g. Lewandowski (2004). The motions of the water particles of the incident wave will generally vary in space in the vicinity

of the hull. These motions can however be considered to be spatially invariant around each section and be represented by some effective mean values, see e.g. Journée and Adegeest (2003). The diffraction forces can now be calculated as sectional forces integrated over the length of the ship, see equation (2.35) and Hua and Palmquist (1995).

$$F_2^{diff} = \int_L \left(j_{22}\bar{a}_h(t) + \int_0^\infty k_{22}(\tau)\bar{v}_h(t-\tau)d\tau \right) dx$$

$$F_3^{diff} = \int_L \left(j_{33}\bar{a}_v(t) + \int_0^\infty k_{33}(\tau)\bar{v}_v(t-\tau)d\tau \right) dx$$

$$F_4^{diff} = \int_L \left(j_{42}\bar{a}_h(t) + \int_0^\infty k_{42}(\tau)\bar{v}_h(t-\tau)d\tau \right) dx \qquad (2.35)$$

$$F_5^{diff} = \int_L -x\left(j_{33}\bar{a}_v(t) + \int_0^\infty k_{33}(\tau)\bar{v}_v(t-\tau)d\tau \right) dx$$

$$F_6^{diff} = \int_L x\left(j_{22}\bar{a}_h(t) + \int_0^\infty k_{22}(\tau)\bar{v}_h(t-\tau)d\tau \right) dx$$

where

$$j_{i,j} = a_{i,j}(\infty) \qquad (2.36)$$

and

$$k_{i,j}(\tau) = \frac{2}{\pi}\int_0^\infty b_{i,j}(\omega)\cdot cos(\omega\tau)\cdot d\omega \qquad (2.37)$$

where $a_{i,j}$ and $b_{i,j}$ are the sectional 2-dimensional added mass and damping coefficients respectively.

$\bar{a}_h$, $\bar{a}_v$, $\bar{v}_h$ and $\bar{v}_v$ are the effective mean accelerations and velocities of the incident wave in the vertical and horizontal directions respectively.

J, K, j and k can now be calculated prior to the start of the time domain simulation, through the frequency domain coefficients.

The Froude-Krylov forces and moments can be calculated through integration of the incident wave pressure over the momentarily wetted hull as described in section 3.5.

3 Method

3.1 Coordinate systems and kinematics

The kinematics of the ship wave system is described by three Cartesian right handed coordinate systems:

$OXYZ$: Global earth fixed system where the XY-plane coincides with the calm water surface. The Z-axis is directed upwards and the X-axis in the direction of incident wave propagation.

$oxyz$: System with origin in the centre of gravity CG of the ship. The z-axis is normal to the still water surface and directed upwards. The direction of the x-axis is defined by the constant heading angle μ with respect to the X-axis of the global system.

$o'x'y'z'$: Ship fixed system with origin in CG and the x'-axis pointing in the forward direction of the ship. This system handles the geometrical properties of the ship model.

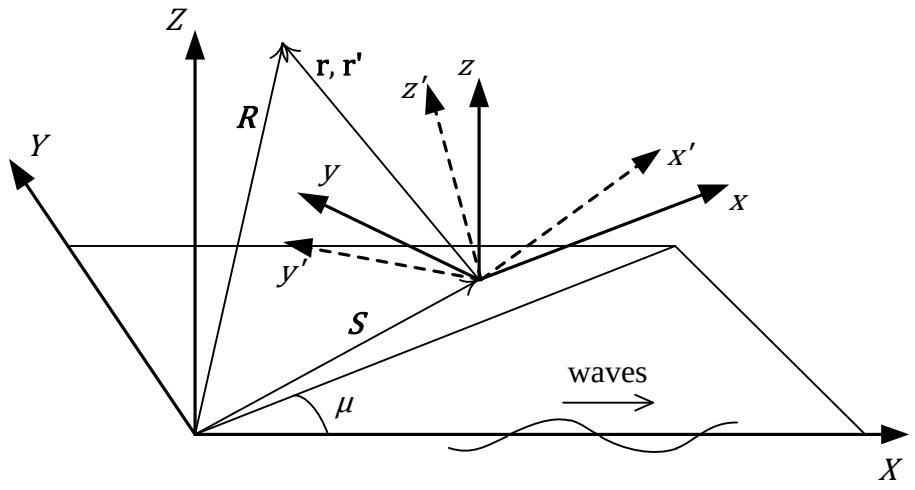

Figure 3-1 Coordinate systems for description of the geometry of ship and waves.

The relation between the $oxyz$ and the $o'x'y'z'$ system can be expressed by the Euler (zyx) transformation matrix T through which the system $o'x'y'z'$ is intrinsically rotated by the angle of yaw (η_6), pitch (η_5) and roll (η_4):

$$[T] = \begin{bmatrix} \cos\eta_6 \cos\eta_5 & \cos\eta_6 \sin\eta_5 \sin\eta_4 - \sin\eta_6 \cos\eta_4 & \cos\eta_6 \sin\eta_5 \cos\eta_4 + \sin\eta_6 \sin\eta_4 \\ \sin\eta_6 \cos\eta_5 & \sin\eta_6 \sin\eta_5 \sin\eta_4 + \cos\eta_6 \cos\eta_4 & \sin\eta_6 \sin\eta_5 \cos\eta_4 - \cos\eta_6 \sin\eta_4 \\ -\sin\eta_5 & \cos\eta_5 \sin\eta_4 & \cos\eta_5 \cos\eta_4 \end{bmatrix} \quad (3.1)$$

A vector $\boldsymbol{r}$ in the $oxyz$ system can be obtained by transformation of the corresponding vector $\boldsymbol{r'}$ in the $o'x'y'z'$ system, Figure 3-1:

$$\boldsymbol{r} = [T] \cdot \boldsymbol{r}' \tag{3.2}$$

Since the transformation matrix T is orthogonal, its inverse equals its transpose, $[T]^{-1} = [T]^T$, hence:

$$\boldsymbol{r}' = [T]^T \cdot \boldsymbol{r} \tag{3.3}$$

Transformation of $\boldsymbol{r}$ to corresponding vector $\boldsymbol{R}$ in $OXYZ$ is obtained through a rotation μ about the z axis followed by a translation according to vector $\boldsymbol{S}$, the location vector of the origin of $oxyz$ expressed in the $OXYZ$ system, Figure 3-1:

$$\boldsymbol{R} = \boldsymbol{S} + [T]_{\eta_6=\mu, \eta_5=\eta_4=0} \cdot \boldsymbol{r} \tag{3.4}$$

and

$$\boldsymbol{r} = [T]^T_{\eta_6=\mu, \eta_5=\eta_4=0} \cdot (\boldsymbol{R} - \boldsymbol{S}) \tag{3.5}$$

Heave (η_3) is the vertical motion of the CG (positive opposing gravity). Sway (η_2) is the horizontal motion of the CG, perpendicular to the ship fixed longitudinal axis and the heave motion (positive to port of the upright ship). Surge (η_1) is the horizontal motion of CG, perpendicular to sway (positive in the direction of the bow).

Manoeuvring forces are not implemented but the ships path on the surface of the sea can however be controlled through e.g. a predefined forward speed and rate of yaw and the position vector $\boldsymbol{S}(t) = \{S_1(t), S_2(t), S_3(t)\}$ of CG is obtained through:

$$\begin{Bmatrix} S_1(t) \\ S_2(t) \\ S_3(t) \end{Bmatrix} = \begin{Bmatrix} S_1(0) \\ S_2(0) \\ S_3(0) \end{Bmatrix} + \int_0^t \begin{bmatrix} \cos(\mu + \eta_6(\tau)) & -\sin(\mu + \eta_6(\tau)) & 0 \\ \sin(\mu + \eta_6(\tau)) & \cos(\mu + \eta_6(\tau)) & 0 \\ 0 & 0 & 1 \end{bmatrix} \cdot \begin{Bmatrix} \dot{\eta}_1(\tau) \\ \dot{\eta}_2(\tau) \\ \dot{\eta}_3(\tau) \end{Bmatrix} \cdot d\tau \tag{3.6}$$

where t is the time, a dot accent represents derivation with respect to time and $\boldsymbol{S}(0)$ are defined through the initial conditions of the simulation. See further section 3.4.

3.2 Geometry of the ship

The hull is defined by a number of sections in arbitrary longitudinal positions. Each section consists of a number of offset points. Straight line segments between these points define the outer hull of each section. The reference point for the ship geometry is the intersection of the

center line, aft perpendicular and base line. When the intact loading condition has been determined the ship geometry is transferred to the $o'x'y'z'$ system.

3.3 Waves

Waves in SIMCAP are derived from the linear theory. They are assumed to be long crested deep water waves.

In linear theory the properties of irregular waves can be obtained through superposition of corresponding regular wave properties. E.g. the wave elevation of an irregular wave is defined through:

$$\xi(\mathrm{X},t)=\sum_{i=1}^{n}\hat{\xi}_i\cos(k_i\mathrm{X}-\omega_i t+\varepsilon_i) \tag{3.7}$$

where ε_i is a random phase shift of the wave component, where the value is drawn from the standard uniform distribution on the interval $(0,2\pi)$.

When a wave energy spectrum is represented by discrete wave components a time domain representation of the spectrum will repeat the wave pattern after $2\pi/d\omega$ seconds if the frequency spacing $d\omega$ is constant. Herein a wave spectrum will be represented by wave components with equal energy content (wave heights). This leads to uneven frequency spacing and avoidance of repeating wave patterns, Belenky et al. (2008).

The wave energy spectra in SIMCAP are defined through:

$$S(\omega)=\alpha\frac{A}{\omega^5}e^{\left(\frac{-B}{\omega^4}\right)}\cdot\gamma^{\beta} \tag{3.8}$$

where

$$\begin{aligned}
&A=173\cdot\frac{{H_s}^2}{{T_1}^4}, \qquad B=\frac{691}{{T_1}^4}\\
&\beta=e^{\frac{-(\omega-\omega_m)^2}{2\sigma^2\omega_m^2}}, \qquad T_1=0.773\cdot T_p\\
&\sigma=0.08+0.01\cdot sign(\omega-\omega_m), \qquad \omega_m=\frac{2\pi}{T_p}
\end{aligned} \tag{3.9}$$

T_1: Period corresponding to average frequency of component waves $(=2\pi m_0/m_1)$
T_p: Peak (modal) period
H_s: Significant wave height
γ : Peak enlargement factor

Two different spectra have been used:

Pierson-Moskowitz (P-M) spectra with $\alpha = \gamma = 1$ and with H_s and T_p as input.
Jonswap spectra with γ=3.3 and α =0.658 and with H_s and T_p as input.

3.4 Equations of motion

The derivation of the equations of motions is based on the conservation of linear and angular momentum and can be expressed by:

$$\boldsymbol{F} = M\ddot{\boldsymbol{\eta}} + \boldsymbol{i} = (M^s + M^{fw})\ddot{\boldsymbol{\eta}} + \boldsymbol{i} \tag{3.10}$$

M^s is the generalized mass matrix of the intact ship, M^{fw} is the generalized mass matrix of the flooded water, $\boldsymbol{\eta}$ is the vector of ship motions and $\boldsymbol{i}$ is a vector containing additional inertial forces due to the non-inertial reference frames in which (3.10) is expressed. $\boldsymbol{F}$ is the vector of external forces and moments. A dot accent represents derivation with respect to time. Here $\boldsymbol{F}$ is divided into the following:

- Radiation forces, F_i^{rad} (section 3.5.1)
- Wave diffraction forces, F_i^{diff} (section 3.5.2)
- Froude-Krylov (including hydrostatic) forces and ship weight, F_i^{FK}, F_i^g (section 3.5.3)
- Forces from the flooded water, F_i^{fw} (section 3.6.4)
- Viscous damping forces, F_i^v (section 3.5.4)

where i is a component direction index corresponding to the motion of the ship. In the present numerical model the ships forward speed, U, is constant and surge motion is not simulated, thus i =2,3,4,5,6.

Equation (3.10) can be described as a system of five non-linear second order differential equations. These equations are rearranged to a set of ten first order equations that are solved numerically in the time domain by the fourth order Runge-Kutta method with initial conditions $\boldsymbol{\eta}(0)$ and $\dot{\boldsymbol{\eta}}(0)$, the position and velocities of the ship at the simulation start were time equals zero, see further section 3.7.

Hydrodynamic coupling through radiation and diffraction is only considered within the vertical plane of motion (between heave and pitch) and lateral motions (between sway roll and yaw) respectively. This is a well-established approach within numerical seakeeping predictions that has been shown to produce reasonably accurate results. The approach is based on geometrical symmetries and assumptions of small motions. SIMCAP must however be able to deal with large motions, specifically in roll, and must rely on that the radiation and diffraction hydrodynamic coupling between e.g. heave and roll for large roll motions are small compared to the Froude-Krylov forces, which are not herein limited by any assumptions on the coupling between the different degrees of freedom.

The coupled equations of vertical and lateral planes of motion are herein solved in two separate coordinate systems:

$o_1x_1y_1z_1$: This system is obtained from the $oxyz$ system through a rotation around the z-axis. This angle defines the yaw of the ship. The ship has a constant forward speed, U, along the x_1-axis. The equations of motion for heave and pitch are expressed in this system, Figure 3-2.

$o_2x_2y_2z_2$: This system is obtained from the $o_1x_1y_1z_1$ system through a rotation around the y_1 axis. This angle defines the pitch of the ship. Roll is defined as the rotation of the ship around the x_2 axis. The equations of motion for roll, sway and yaw is expressed in this system, Figure 3-2.

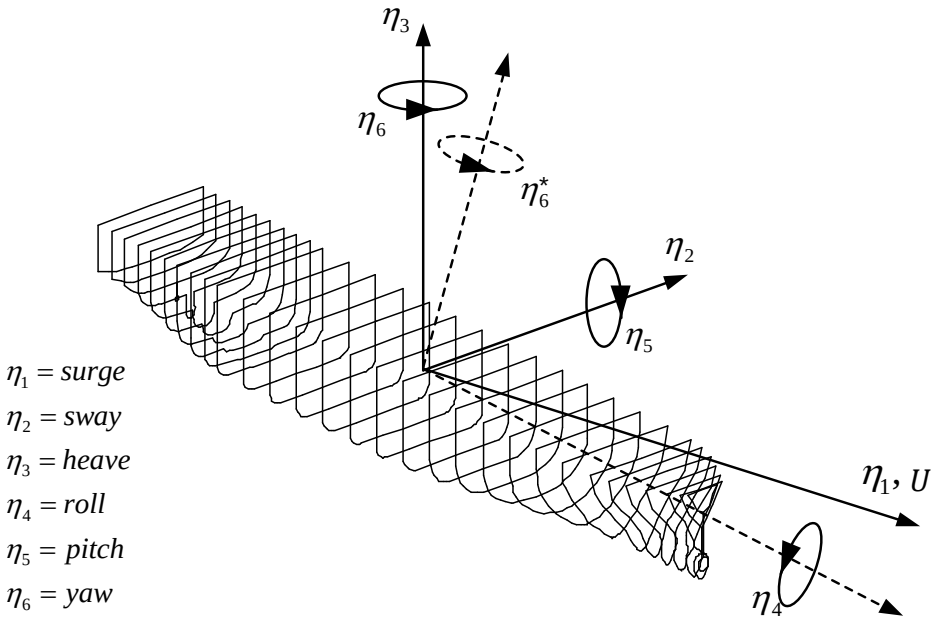

Figure 3-2 Definition of the six degrees of freedom. The $o_1x_1y_1z_1$ axes are solid and the $o_2x_2y_2z_2$ axes are dashed. The ship forward speed, U, is defined along the $x_1$axis.

The relation between η_6^* and η_6 of Figure 3-2 is $\eta_6 = \tan^{-1}(\tan(\eta_6^*)\cos(\eta_5))$ and $\eta_6 \approx \eta_6^*$ for small pitch angles. η_6 have thus been used in eq. (3.10) and:

$$\boldsymbol{\eta} = \{\eta_2\ \eta_3\ \eta_4\ \eta_5\ \eta_6\}^T \tag{3.11}$$

The product moments of inertia can be regarded as small for conventional ships due to small asymmetries in the starboard-port and forward-aft mass distributions. Thus the off diagonal terms of the generalized mass matrix of the intact ship are herein zero and the components of M^s is reduced to:

$$
\begin{aligned}
M_{22}^S &= M_{33}^S = m \\
M_{44}^S &= I_4^S = mk_{x'}^2 \\
M_{55}^S &= I_5^S = m(k_{y'}^2 \cos^2\eta_4 + k_{z'}^2 \sin^2\eta_4) \\
M_{66}^S &= I_6^S = m(k_{z'}^2 \cos^2\eta_4 + k_{y'}^2 \sin^2\eta_4)
\end{aligned}
\tag{3.12}
$$

where m is the mass of the intact ship and $k_{x'}, k_{y'}$ and $k_{z'}$ are the radius of mass moment of inertia for the intact ship expressed in the body fixed coordinate system. If these values are not known the default values of $k_{x'}$=0,35$\cdot B$ and $k_{y'}$=$k_{z'}$=0,25$\cdot L$ are used. M^{fw}, the generalized mass matrix of the flooded water, is defined in section 3.6.5.

Note that the coordinate systems in which the equations of motion for pitch and yaw are expressed are not body fixed and do not rotate in roll. To account for this the mass moment of inertia for pitch (I_5^S) and yaw (I_6^S) are calculated according to eq. (3.12) where a smooth transition between $k_{y'}$ and $k_{z'}$ is obtained as the ship is rolling/listing. E.g. $k_{y'}$=$k_{z'}$ will lead to I_5^S=I_6^S= $mk_{y'}^2$.

When the equations of motions of a rigid body are solved in a non-inertial reference frame there will be additional inertial forces due to cross coupling terms of linear and angular velocities of the reference frame, see e.g. Lewandowski (2004). If the equations of motions are expressed in a body-fixed coordinate system with origin in the center of gravity and with an assumption of a diagonal generalized mass matrix these forces will be:

$$
\boldsymbol{i} = \begin{Bmatrix}
m(\dot{\eta}_3\dot{\eta}_5 - \dot{\eta}_6\dot{\eta}_2) \\
m(\dot{\eta}_1\dot{\eta}_6 - \dot{\eta}_3\dot{\eta}_4) \\
m(\dot{\eta}_2\dot{\eta}_4 - \dot{\eta}_1\dot{\eta}_5) \\
(I_6^S - I_5^S)\dot{\eta}_5\dot{\eta}_6 \\
(I_4^S - I_6^S)\dot{\eta}_4\dot{\eta}_6 \\
(I_5^S - I_4^S)\dot{\eta}_4\dot{\eta}_5
\end{Bmatrix}
\tag{3.13}
$$

Herein the surge motion is not simulated ($\dot{\eta}_1$ will however correspond to a stipulated forward speed U) and the first row of equation (3.13) will vanish. Moreover since the remaining equations of motion are expressed in the $o_1x_1y_1z_1$ and $o_2x_2y_2z_2$ systems, terms in (3.13) involving $\dot{\eta}_4$ will vanish as will the second term of the third row (heave force) as $o_1x_1y_1z_1$ do not rotate in pitch. As a result equation (3.13) is simplified into:

$$
\boldsymbol{i} = \begin{Bmatrix}
mU\dot{\eta}_6 \\
0 \\
(I_6^S - I_5^S)\dot{\eta}_5\dot{\eta}_6 \\
0 \\
0
\end{Bmatrix}
\tag{3.14}
$$

3.5 Forces and moments

3.5.1 Radiation forces

The radiation forces of (3.10) are obtained from equations (2.28), (2.33) and (2.34) and can be expressed as:

$$F_i^{rad}(t) = -\sum_j \left\{ A_{ij}^{\infty}\,\ddot{\eta}_j(t) + B_{ij}^{\infty}\,\dot{\eta}_j(t) + \int_0^{t_c} K_{ij}(\tau)\,\dot{\eta}_j(t-\tau)d\tau \right\} \tag{3.15}$$

where:

$$K_{ij}(\tau) = \frac{2}{\pi}\int_0^{\infty} \left[B_{ij}(\omega) - B_{ij}^{\infty}\right] cos(\omega\tau)\, d\omega \tag{3.16}$$

and:

$j = 2,4,6$ for $i = 2$ (Sway force)
$j = 3,5$ for $i = 3$ (Heave force)
$j = 2,4,6$ for $i = 4$ (Roll moment)
$j = 3,5$ for $i = 5$ (Pitch moment)
$j = 2,4,6$ for $i = 6$ (Yaw moment)

A_{ij} and B_{ij} are the frequency dependent 3-D added mass and damping coefficients respectively. They are defined through the ordinary strip theory, see Appendix 1, since this is reported to produce more accurate results for moderate forward ship speeds compared to the modified strip theory, Journée and Adegeest (2003), and the simulated cases herein have a maximum forward speed of Fn=0.12.

In eq. (3.16) the damping at infinite frequency, B_{ij}^{∞}, has been subtracted to the damping term of eq. (2.34) which will be better from a numerical point of view (Fossen 2005), as the high frequency content of the kernel function will be reduced. The second term in eq. (3.15) has been added in order to retain the validity of the equation.

In theory the convolution term in the radiation forces should be calculated for an infinite time history, i.e. t_c=∞. The kernel function (3.16) will however be very small after a certain time. A value of t_c=40-50 seconds is found appropriate together with a time stepping of 0.25-0.50 seconds. (Formulation of a limit for t_c is suggested by Journée (1993) resulting in slightly lower values for a few test calculations.)

The hydrodynamic coefficients are calculated at discrete values of ω, typically between 0.05 and 2.5-5 radians/s with a step of 0.05 radians/s, which will also be the span of the calculation of the kernel function. A_{ij}^{∞} and B_{ij}^{∞} are calculated at the highest value of ω.

3.5.2 Wave diffraction forces

The diffraction forces in SIMCAP are obtained from equation (2.35) and can be expressed:

$$
\begin{aligned}
F_2^{diff} &= \int_L \left(a_{22}^{\infty}\bar{a}_h(t) + b_{22}^{\infty}\bar{v}_h(t) + \int_0^{t_c} k_{22}(\tau)\bar{v}_h(t-\tau)d\tau \right) dx' \\
F_3^{diff} &= \int_L \left(a_{33}^{\infty}\bar{a}_v(t) + b_{33}^{\infty}\bar{v}_v(t) + \int_0^{t_c} k_{33}(\tau)\bar{v}_v(t-\tau)d\tau \right) dx' \\
F_4^{diff} &= \int_L \left(a_{42}^{*\infty}\bar{a}_h(t) + b_{42}^{*\infty}\bar{v}_h(t) + \int_0^{t_c} k_{42}{}^{*}(\tau)\bar{v}_h(t-\tau)d\tau \right) dx' \\
F_5^{diff} &= \int_L -x_1 \left(a_{33}^{\infty}\bar{a}_v(t) + b_{33}^{\infty}\bar{v}_v(t) + \int_0^{t_c} k_{33}(\tau)\bar{v}_v(t-\tau)d\tau \right) dx' \\
F_6^{diff} &= \int_L x_2 \left(a_{22}^{\infty}\bar{a}_h(t) + b_{22}^{\infty}\bar{v}_h(t) + \int_0^{t_c} k_{22}(\tau)\bar{v}_h(t-\tau)d\tau \right) dx'
\end{aligned}
\tag{3.17}
$$

with the kernel functions:

$$
k_{ij}(\tau) = \frac{2}{\pi}\int_0^{\infty} \left[b_{ij}(\omega) - b_{ij}^{\infty} \right] cos(\omega\tau)\, d\omega \tag{3.18}
$$

The sectional hydrodynamic coefficients have been calculated with the still water surface as the vertical reference. The change of reference to the center of gravity of the ship is obtained through:

$$
\begin{aligned}
a_{42}^{*\infty} &= a_{42}^{\infty} + OGa_{22}^{\infty} \\
b_{42}^{*\infty} &= b_{42}^{\infty} + OGb_{22}^{\infty} \\
k_{42}^{*} &= k_{42} + OGk_{22}
\end{aligned}
\tag{3.19}
$$

where $OG = KG - d$.

$\bar{a}$ and $\bar{v}$ represent the spatial mean fluid particle acceleration and velocity of the incident wave over the boundary of the section. Index h refer to the horizontal component in the plane of the section and index v refer to the vertical component. $\bar{a}$ and $\bar{v}$ are calculated through eq. (3.20).

$$\begin{aligned}
\bar{a}_h &= \sum \frac{1 - e^{-kd_e}}{k \cdot d_e} \cdot \cos\big(k \cdot b_e \cdot \sin(\mu + \eta_6)\big) \cdot a_h \\
\bar{a}_v &= \sum e^{-kd_e} \cdot \frac{\sin\big(k \cdot b_e \cdot \sin(\mu + \eta_6)\big)}{k \cdot b_e \cdot \sin(\mu + \eta_6)} \cdot a_v \\
\bar{v}_h &= \sum \frac{1 - e^{-kd_e}}{k \cdot d_e} \cdot \cos\big(k \cdot b_e \cdot \sin(\mu + \eta_6)\big) \cdot v_h \\
\bar{v}_v &= \sum e^{-kd_e} \cdot \frac{\sin\big(k \cdot b_e \cdot \sin(\mu + \eta_6)\big)}{k \cdot b_e \cdot \sin(\mu + \eta_6)} \cdot v_v
\end{aligned} \tag{3.20}$$

The summation refers to the wave components of an irregular sea. b_e and d_e are the effective hydrodynamic half beam and draught of the section respectively. They are defined through:

$$\begin{aligned}
b_e &= \frac{S_A(t)}{2 \cdot d(t)} \\
d_e &= \frac{S_A(t)}{2 \cdot b_e}
\end{aligned} \tag{3.21}$$

where $S_A(t)$ is the submerged area of the section and $d(t)$ is the vertical extent of the submerged section.

a and v are the fluid particle accelerations and velocities of the incident wave, in the plane of the section, at the mean wave surface at the center of the section. They are calculated through:

$$\begin{aligned}
a_h &= \hat{\xi}\omega_e^2 \sin(kX(t) - \omega t) \sin(\mu + \eta_6) \\
a_v &= -\hat{\xi}\omega_e^2 \cos(kX(t) - \omega t) \\
v_h &= \hat{\xi}\omega_e \cos(kX(t) - \omega t) \sin(\mu + \eta_6) \\
v_v &= \hat{\xi}\omega_e \sin(kX(t) - \omega t)
\end{aligned} \tag{3.22}$$

where $X(t)$ is the mean of the co-ordinates of the wetted section points i in the global system; $X(t) = mean\big(X_i(t)\big)$. A derivation of the equations in (3.20) can be found in Appendix 2. ω_e is the frequency of encounter defined through:

$$\omega_e = \omega - \frac{\omega^2 U \cos(\mu + \eta_6)}{g} \tag{3.23}$$

The two-dimensional hydrodynamic coefficients a_{ij} and b_{ij} are obtained through an in-house code (Hua and Palmqvist 1995) where the Lewis conformal mapping technique is utilized. The coefficients are calculated prior to the simulation start for the floating position of the intact ship. The conformal mapping technique is a rather simplistic approach and cannot accurately represent modern hull forms with e.g. hard shines. A ship at large heel angles simulated through coefficients that are pre-calculated for an upright condition will however typically be a larger limiting factor than the calculation technique for the coefficients. The calculation technique could however easily be replaced by more sophisticated methods in further development of the code.

3.5.3 Froude-Krylov forces

For the Froude-Krylov force calculation the incident wave pressure is integrated over the momentarily wetted part of the ship hull. The incident wave pressure is herein defined by the sum of linear dynamic pressure and hydrostatic pressure:

$$p = -\rho \frac{\partial \phi_I}{\partial t} - \rho g Z \tag{3.24}$$

By the assumptions of linear wave theory follows that the dynamic pressure is constant from the mean free surface to the actual free surface. As suggested in Faltinsen (1990) the dynamic pressure is here defined through:

$$\begin{aligned} -\rho \frac{\partial \phi_I}{\partial t} &= \sum \rho g \hat{\xi} e^{kZ} \cos(kX - \omega t) \quad \text{for} \quad Z \leq 0 \\ -\rho \frac{\partial \phi_I}{\partial t} &= \sum \rho g \hat{\xi} \cos(kX - \omega t) \quad \text{for} \quad Z > 0 \end{aligned} \tag{3.25}$$

The hydrostatic component of eq. (3.24) is defined everywhere in the fluid. These definitions will result in zero incident wave pressure at the surface of a crest whereas there will be a small error at the surface of a trough. A representation of the pressure distribution is shown in Figure 3-3.

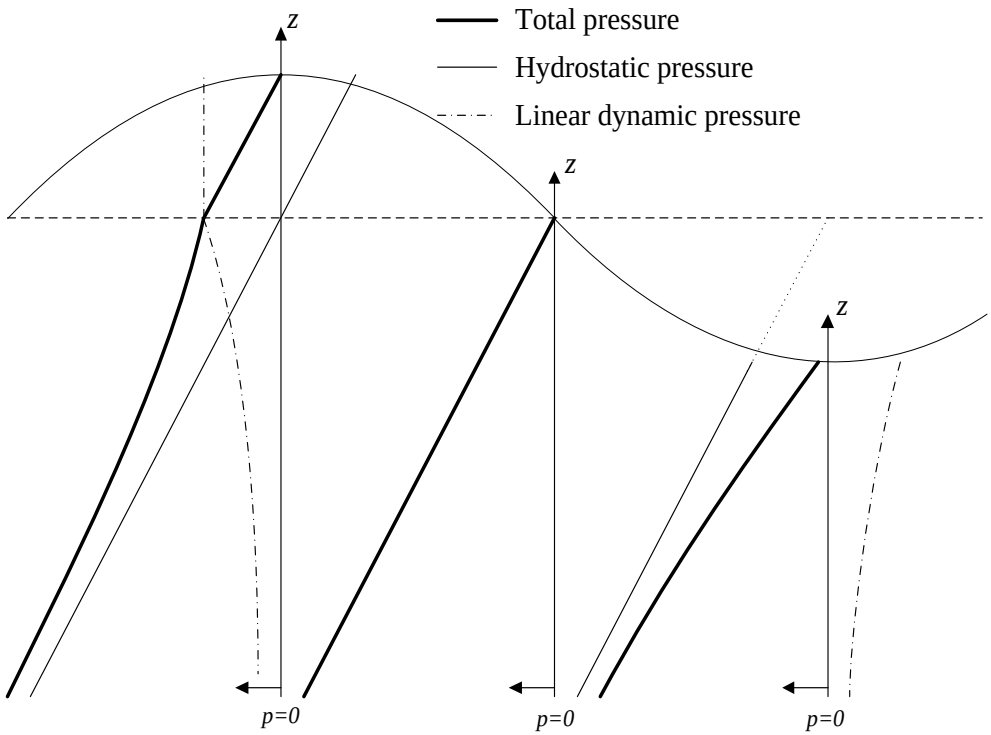

Figure 3-3 Pressure distribution for Froude-Krylov calculation in three vertical sections of a wave: crest, trough and at maximum wave slope. (The axes are not to scale.)

At the intersection points between the wave surface and the sections of the ship new offset points are created by linear interpolation. These offset points separate the underwater part of the hull from the upper part. In this manner the underwater part of the hull is extracted in each time step, Figure 3-4.

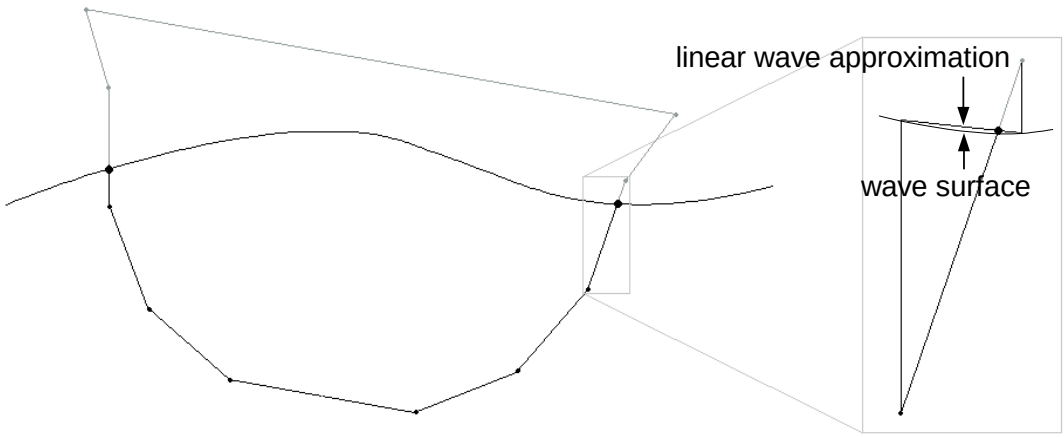

Figure 3-4 Wave intersection offset point on a ship section. The two offset points adjacent to the wave intersection are vertically projected on the wave. A straight line between these projected points intersects with the hull segment and defines the new offset point.

The Froude-Krylov forces are obtained through integration of the contribution from each section over the ship length and can be expressed:

$$F_2^{FK} = \int_L (f_2^{FK}) dx'$$

$$F_3^{FK} = \int_L (f_3^{FK}) dx'$$

$$F_4^{FK} = \int_L (f_4^{FK}) dx' \tag{3.26}$$

$$F_5^{FK} = \int_L -x_1 (f_3^{FK}) dx'$$

$$F_6^{FK} = \int_L x_2 (f_2^{FK}) dx'$$

The sectional forces and moment $f_{2,3,4}^{FK}$ are obtained from the sum of the contribution from the wetted hull segments of each section. The force and moment contribution from a section segment i can be expressed by:

$$\begin{aligned} f_2^{FK_i} &= n_{y_2} \int p(s) ds \\ f_3^{FK_i} &= n_{z_2} \cos(\eta_5) \int p(s) ds \\ f_4^{FK_i} &= \int p(s) \left(y_2(s) n_{z_2} - z_2(s) n_{y_2} \right) ds \end{aligned} \tag{3.27}$$

where s is a co-ordinate along the hull segment and $\boldsymbol{n}$ is the unit normal vector of the segment in the plane of the section and directed inwards (in the direction of pressure forces).

The equations in (3.27) are solved through Gaussian quadrature, where each segment is represented by three integration points, see e.g. Råde and Westergren (1988).

By using the total pressure in the Froude-Krylov force calculation the buoyancy force of the ship will be included and the weight of the ship is therefore added to equations of motion through: $F_3^g = -mg$.

3.5.4 Viscous damping forces

SIMCAP is based on potential flow theory where viscosity is neglected. For the roll motion of ships the potential damping is small however, and the viscous effects have a significant influence and need to be accounted for. This is done through a quadratic formulation where the coefficients are tuned to match experimental roll decay tests. If no experimental data is available the damping is expressed as a percentage of critical roll damping. The viscous damping is expressed as:

$$F_4^v = -B_{cr}\left(\alpha + \beta\left|\dot{\eta}_4\right|\right)\dot{\eta}_4 \tag{3.28}$$

Where $B_{cr} = 2\sqrt{(I_4^s + A_{44})mgGM}$ is the critical damping in roll and A_{44} is assumed to be 20% of I_4^s. α and β are the linear and quadratic tuning coefficients with default values $\alpha = 0.1$ and $\beta = 0$.

3.6 Damage simulation

In a damage simulation the amount of water in- or outflow through all floodable openings has to be determined for each time step. Also, the effect of the flooded water on the ships motions i.e. the forces and moments from the flooded water acting on the ship and the inertia of the flooded water have to be assessed. In addition, at any opening connecting the interior of the hull with the sea the pressure gradient over the damaged opening is accounted for in the Froude-Krylov excitation force calculation.

3.6.1 Compartments

Compartments susceptible to flooding are defined by a set of sections at different longitudinal positions in the same manner as the outer hull of the ship and by a uniform volumetric permeability. At each time step the geometry and the associated center of gravity of the flood water are determined for each compartment. The geometry is defined by the compartment geometry, volume of floodwater, permeability, ship position and with the constraint that the floodwater surface is flat and horizontal.

The geometry is found by an iterative process where the filling level is corrected based on the permeable surface area in the previous iteration step until the volumetric error satisfies a pre-set criterion. The floodwater is represented by polygons at the compartment sections and the center of gravity can be easily calculated.

3.6.2 Damage openings and flooding process

A damage opening connecting a compartment with the open sea or another compartment is defined through a set of points each associated with an opening area.

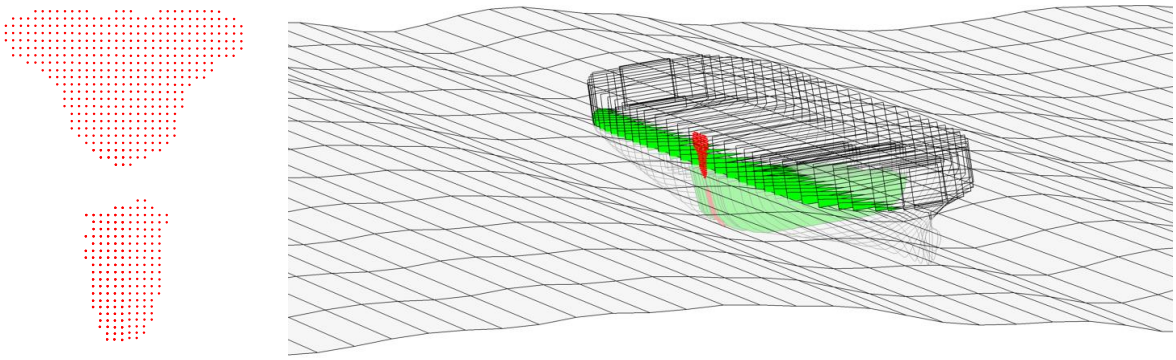

Figure 3-5 Damage represented by point openings (left). The damage is caused by a ship-ship collision and is situated amidships on the struck ship (right).

The damage depicted in Figure 3-5 is connecting the vehicle deck and two compartments below with the open sea and consists of three damage openings in the numerical model.

The flow through the damage openings is determined through a hydraulic formulation similar to that given in Vassalos and Turan (1994). It is based on the stationary Bernoulli equation resulting in:

$$\Delta V_A = \sum_{i=1}^{n} C_d \cdot sign(h_i^a - h_i^b)\sqrt{2g\left|h_i^a - h_i^b\right|} \cdot A_i \cdot \Delta t \tag{3.29}$$

where ΔV_A is the volumetric flow through damage opening A during time step Δt. The damage opening connects a and b which are two compartments or one compartment and the open sea. h_i^a and h_i^b are the pressure heights of point i on respective sides of the damage opening, see Figure 3-6. The pressure height is set to zero if the point is above the surface on corresponding side of the opening. A_i is the opening area of point i and C_d is an empirical discharge coefficient. An assumption has thus been made that the pressure below the wave surface is hydrostatic and dependent on the vertical distance from the incident wave profile.

The formulation is widely used in similar tools and has been shown to produce reasonable agreement with model tests regarding vehicle deck flooding, e.g. Vassalos et al. (1997). The values of C_d used in the studies of chapters 4 and 5 are based on experience from previous simulations or from measurements, as described in respective sections. If no measurements were available values of either 0,5 or 0,6 have been used.

The flooded compartments are assumed to be fully ventilated in SIMCAP and the effect of compression of air, trapped inside a compartment, is not accounted for.

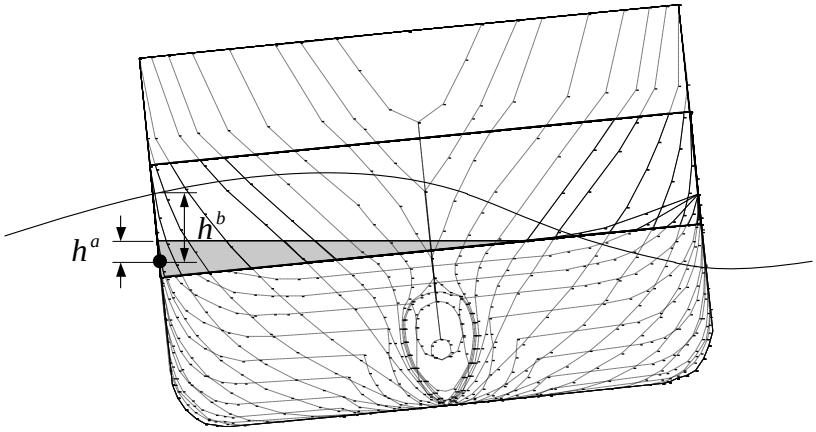

Figure 3-6 Pressure heights of a point opening.

3.6.3 Progressive flooding

Progressive flooding is the flooding of spaces through internal openings leading to other spaces within the ship e.g. open or damaged water tight doors or manhole covers or broken piping. Progressive flooding involving any number of compartments and openings can be simulated by SIMCAP. A fully automated procedure is however not implemented. The progressive flooding case in Figure 3-7 and the cases in section 4.2 is treated by conditional statements, specified prior to the simulations, based on the possible flooding paths and specifically tailored for these cases.

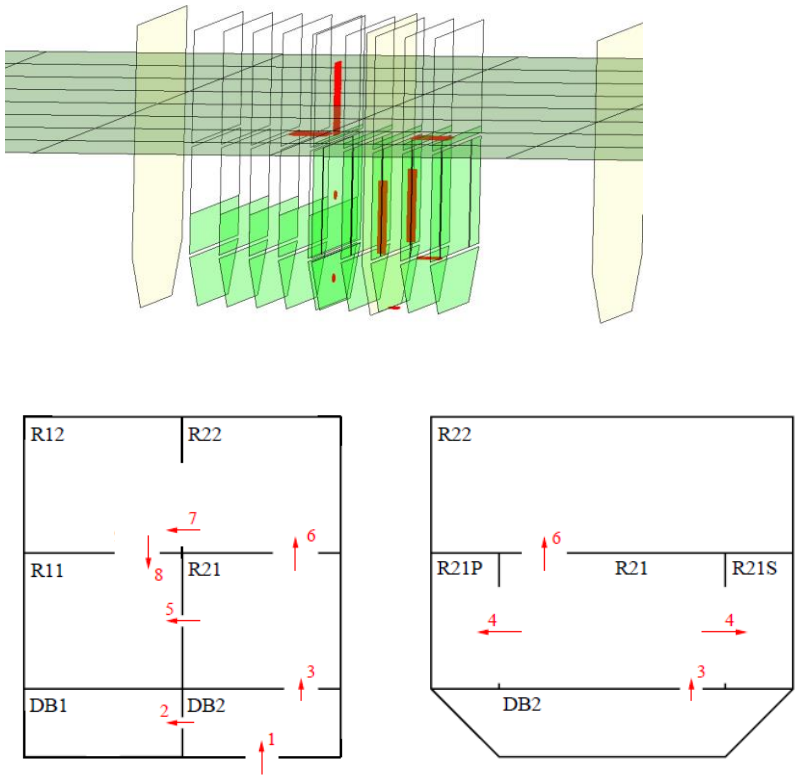

Figure 3-7 A group of compartments are flooded progressively through a bottom damage opening (from section 4.2). SIMCAP model during flooding (above) and a profile and section drawing of the compartments, with flooding indicated by arrows, (below).

3.6.4 Excitation forces from floodwater

The contribution to the excitation forces of the flooded water (F_i^{fw}) from the floodwater in a compartment, with the mass m^{fw} and the center of gravity cg, is calculated through eq. (3.30).

$$\begin{aligned} F_2^{fw} &= F_6^{fw} = 0 \\ F_3^{fw} &= m^{fw} \cdot g \\ F_4^{fw} &= -cgy_2 \cdot \cos(\eta_5) \cdot m^{fw} \cdot g \\ F_5^{fw} &= cgx_1 \cdot m^{fw} \cdot g \end{aligned} \tag{3.30}$$

Thus the exciting forces from the floodwater only include the floodwater weight. Forces due to the relative motions (velocities and accelerations) between the ship and the floodwater, i.e. Coriolis and Euler forces, are omitted in the present implementation of SIMCAP. They are believed to be small in general due to small relative motions. Also, when large motions are expected viscous effects are believed to become increasingly significant and as these effects are not included in the model, SIMCAP will over estimate these motions e.g. small amounts of floodwater rushing from side to side on a car deck.

3.6.5 Inertia forces from floodwater

The inertia forces of the floodwater are accounted for by updating the generalized mass matrix of the flooded water (M^{fw}) in each time step. In the translational motions the floodwater mass is simply added to the generalized mass.

In the rotational motions the generalized masses of the ship are updated by the Steiner contribution (parallel displacement of rotational axis) of the floodwater. This is an approximation in the sense that for any motion, relative to the ship, of the center of gravity of the floodwater in the tangential direction of corresponding rotation, the inertia will be affected, which is not included through the Steiner contribution. Compare e.g. a partly flooded compartment with a circular cross section centred at the center of gravity of the ship.

Note that under the assumption of a horizontal floodwater surface and absence of viscous effects, the floodwater “moves freely” and does not possess any inertia around an axis through its center of gravity.

The product moments of inertia have been omitted in the present simulations. It is believed that this will not have any significant effect on the results since the damage cases herein have a high degree of forward aft symmetry. An exception to this symmetry would be e.g. early stages of vehicle deck flooding, where the floodwater can gather close to one corner of the deck. The amount of floodwater and thus the inertia effect will however be relatively small in these cases.

The contribution to the generalized mass matrix of the flooded water (M^{fw}) from the floodwater in a compartment, with the mass m^{fw} and the center of gravity cg, is thus calculated through:

$$
\begin{aligned}
M^{fw}{}_{22} &= M^{fw}{}_{33} = m^{fw} \\
M^{fw}{}_{44} &= (cgy_2^2 + cgz_2^2) \cdot m^{fw} \\
M^{fw}{}_{55} &= (cgx_2^2 + cgz_2^2) \cdot m^{fw} \\
M^{fw}{}_{66} &= (cgx_2^2 + cgy_2^2) \cdot m^{fw}
\end{aligned}
\tag{3.31}
$$

3.6.6 Pressure gradient over damage opening

In the final stage of flooding in calm water, there will be equilibrium between the water inside the compartment and the water outside. There will be no pressure gradient over the damage opening and the hull can be treated as if it were intact in respect of forces from the water pressure acting on the hull. In the intermediate stages of flooding on the other hand, there will be a pressure gradient over the damage opening. This pressure gradient will not only drive the inflow process, described above, it will also change the forces on the ship since there is no hull surface for the outside water pressure to act upon.

In order to include this effect, Froude-Krylov forces are calculated for the portion of the damage opening below the wave surface but above the water level inside of the compartment. These forces are subtracted from the Froude-Krylov forces on the intact hull. This will have the effect of zero pressure over this part of the damage opening, see Figure 3-8.

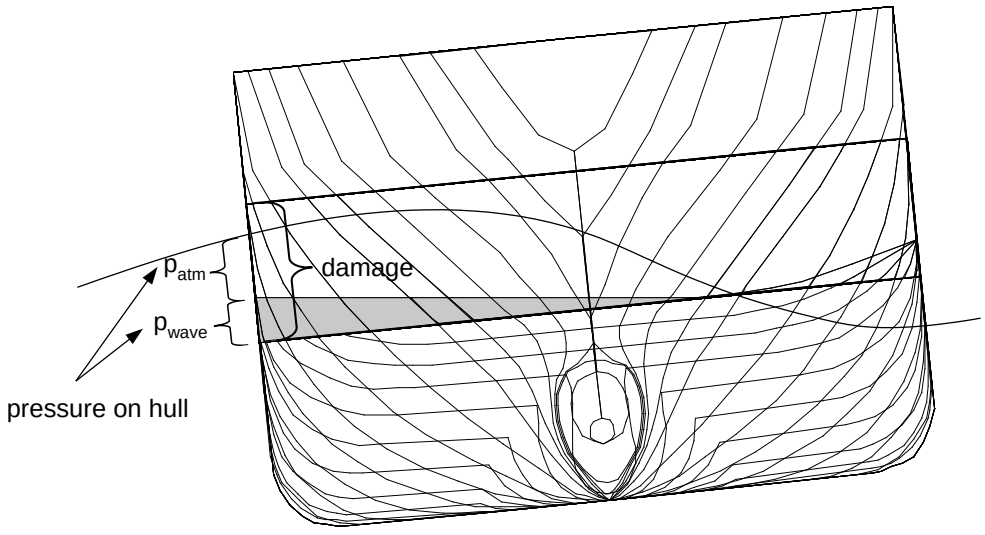

Figure 3-8 Simulation of pressure on hull at damage opening

3.7 Solution method and time stepping

Solution to the equations of motion is obtained through the fourth order Runge-Kutta method. The second order system of equations (3.10) is solved for the accelerations $\ddot{\boldsymbol{\eta}}$ and is transformed to a first order system $\dot{\boldsymbol{R}} = f(\boldsymbol{R})$ where:

$$\boldsymbol{R} = (\eta_4, \dot{\eta}_4, \eta_2, \dot{\eta}_2, \eta_3, \dot{\eta}_3, \eta_5, \dot{\eta}_5, \eta_6, \dot{\eta}_6\ ) \tag{3.32}$$

and

$$f(\boldsymbol{R}) = (\boldsymbol{R}(2), \ddot{\eta}_4, \boldsymbol{R}(4), \ddot{\eta}_2, \boldsymbol{R}(6), \ddot{\eta}_3, \boldsymbol{R}(8), \ddot{\eta}_5\ , \boldsymbol{R}(10), \ddot{\eta}_6\ ) \tag{3.33}$$

With the time stepping $t_{n+1} = t_n + \Delta t$ the Runge-Kutta scheme is described by:

$$\boldsymbol{R}_{n+1} = \boldsymbol{R}_n + \frac{1}{6}(\boldsymbol{k}_1 + 2\boldsymbol{k}_2 + 2\boldsymbol{k}_3 + \boldsymbol{k}_4) \tag{3.34}$$

where the substeps $\boldsymbol{k}_i$ are:

$$\begin{aligned}
\boldsymbol{k}_1 &= \Delta t \cdot f(t_n, \boldsymbol{R}_n) \\
\boldsymbol{k}_2 &= \Delta t \cdot f\left(t_n + \frac{\Delta t}{2}, \boldsymbol{R}_n + \frac{\boldsymbol{k}_1}{2}\right) \\
\boldsymbol{k}_3 &= \Delta t \cdot f\left(t_n + \frac{\Delta t}{2}, \boldsymbol{R}_n + \frac{\boldsymbol{k}_2}{2}\right) \\
\boldsymbol{k}_4 &= \Delta t \cdot f(t_n + \Delta t, \boldsymbol{R}_n + \boldsymbol{k}_3)
\end{aligned} \tag{3.35}$$

and the initial conditions are:

$$\boldsymbol{R}_0 = \left(\eta_4(0), \dot{\eta}_4(0), \eta_2(0), \dot{\eta}_2(0), \eta_3(0), \dot{\eta}_3(0), \eta_5(0), \dot{\eta}_5(0), \eta_6(0), \dot{\eta}_6(0)\right) \tag{3.36}$$

The initial conditions for the wave and ship motion histories, included in the convolution terms of the diffraction and radiation force calculations respectively, are zero. The histories are updated as the time stepping progresses.

4 Validation studies

4.1 Ro-Pax capsize in waves

A series of physical model experiments was carried out within the FLOODSTAND project by SSPA, Rask (2010). The purpose of the experiments was to establish the frequency distribution of the time to capsize for a damaged RoPax ship drifting in beam seas and to provide benchmark data for numerical codes. The results are used to validate the SIMCAP code and the main particulars of the physical and numerical model are shown in Table 4-1. All data presented are expressed in full scale.

Table 4-1 Main data of the intact ship

Parameter	**Unit**	**Physical model**	**Numerical model**
Length, Lpp	[m]	137.4	same
Breadth, moulded	[m]	24.2	same
Draft, aft	[m]	5.61	Same
Draft, forward	[m]	5.17	Same
Displacement	[m^3]	12046	11900 (99%)
VCG (above BL)	[m]	10.62	Same
GM	[m]	1.17	1.16 (99%)
Radii of gyration in air, roll	[m]	8.954 (0.37*B)	Same
Radii of gyration in air, pitch	[m]	37.1 (0.27*Lpp)	Same

The model was a 1:40 scale RoPax ship with a two compartment SOLAS damage on the port side, Figure 4-1. The damage opening on the physical model was created according to SOLAS damage opening standard by means of a V-cut in the hull from bottom to top. In the numerical model the damage opening is defined as the projection of the V-cut opening onto the intact hull, Figure 4-2. The damage connects four spaces with the open sea; the car deck (which is not flooded at the still water damage equilibrium), the main engine room (MER) and two spaces, separated by a deck, aft of the MER of which the lower space is asymmetric due to intact tanks on the starboard side. The other spaces have SB/PS symmetry. The permeability is assumed to be 1.0 for the car deck and 0.85 for the other spaces which will render a list just below two degrees at the damage equilibrium. The physical model had a slightly higher degree of asymmetry due to loss of buoyant material in the damage cut out which is not reflected in the numerical model. This difference is however not believed to have any significant impact on the results.

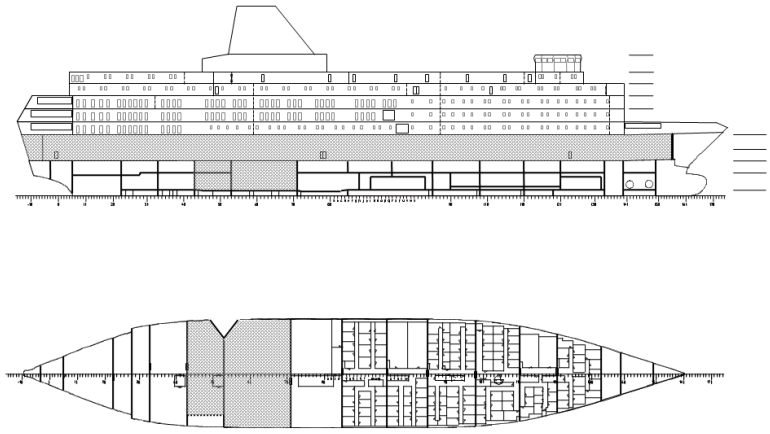

Figure 4-1 The two compartment damage case.

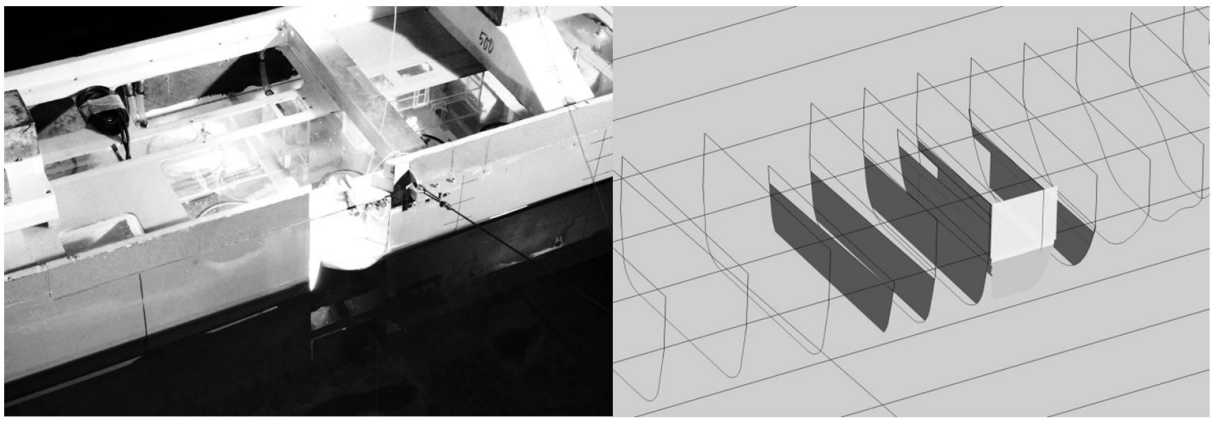

Figure 4-2 Damage opening in physical (left) and SIMCAP model, where the v-cut is projected on the outer hull.

The quadratic roll damping coefficients used in the numerical simulations were calibrated to match a roll-decay experiment of the intact ship model. These coefficient values are used throughout the simulations. The discharge coefficient was determined based on experience from previous simulations e.g. Spanos and Papanikolaou (2011) and de Kat and Paulling (2001) and is kept constant for all simulations with a value of C_d=0.6.

During the tests the model was floating freely with long crested beam waves and zero forward speed and floating at the damaged equilibrium at the start of each test. The yaw and surge motions were however very small throughout all tests why these degrees of freedom are captive in the simulations.

The sea states of the tests had a span of significant wave heights *(H_s)* between two and three meters and were represented by a Jonswap spectra with γ=3.3 and $T_p = 4 \cdot \sqrt{H_s}$. The simulations include wave heights up to four meters. For each sea state 20 tests and simulations respectively with different wave realizations were conducted. In Figure 4-3 the time series of car deck flood volume, roll angle and wave elevation for a typical capsize simulation is shown, where flood water on the car deck is accumulated until some critical

amount is reached followed by a rapid capsize and further flooding of the car deck through the increasingly large damage opening. It should be noted that no superstructure is modeled which would slow down the rapid capsize process. A non-watertight superstructure cannot however prevent capsize; it can only slow down the process towards an inevitable event.

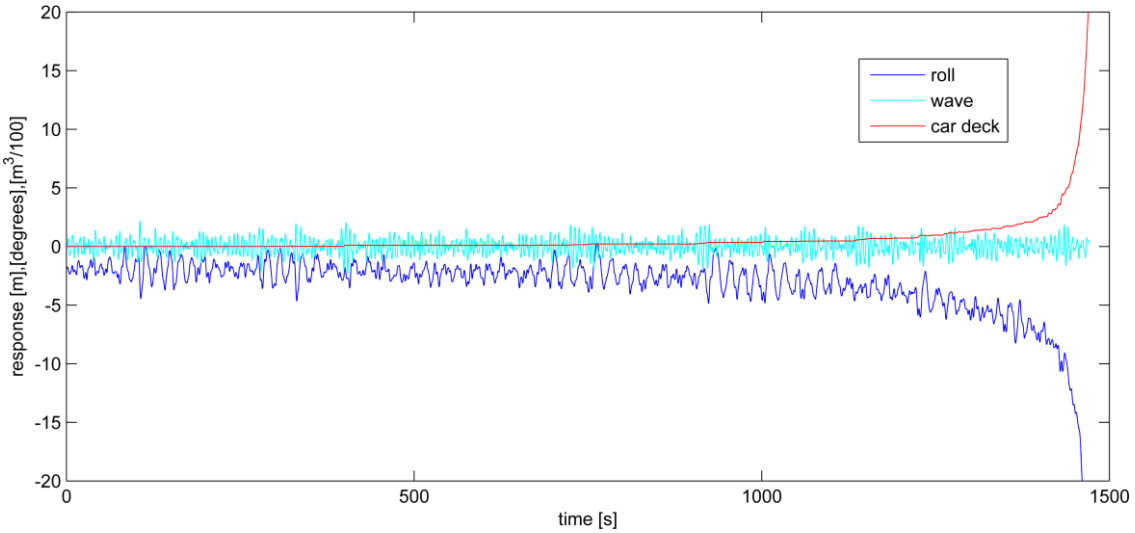

Figure 4-3 Time series of roll angle, wave elevation and car deck flood volume for a characteristic capsize simulation (H_s=2.6 m).

If no capsize occurred both tests and simulations were stopped after 30 minutes. The simulations are also stopped if the roll angle exceeds 180°. The time to capsize is however defined as when 20° is exceeded. The impact of alternative definitions of T_{cap} i.e. 30° and 180° is small and is presented in Figure 4-6. The tests were interrupted when the average heel angle exceeded 20°.

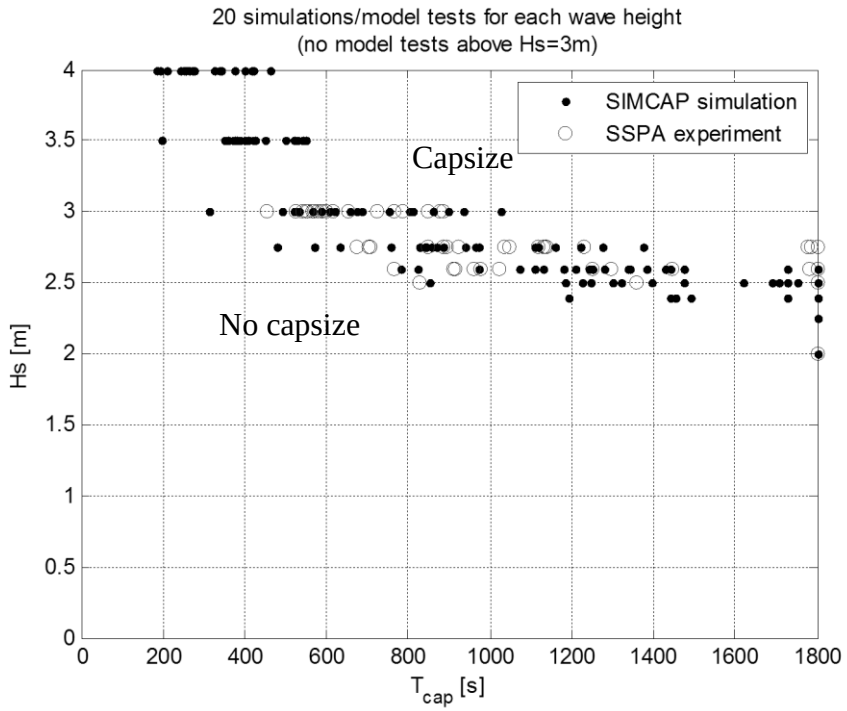

Figure 4-4 Experimental and numerical data on the time to capsize.

Figure 4-4 present all test and simulation results as significant wave height versus time to capsize (T_{cap}). More than an apparent fairly high correlation between experiments and simulations the figure show the typical behavior of a damaged RoRo ship with the vehicle deck subjected to flooding through wave action. All capsize events appear in a characteristically shaped region, above which there is no ship survival and below which there is no capsize, which have previously been denoted capsize band, see e.g. Jasionowski et al. (2003). This is also illustrated in Figure 4-5 where the results are presented as a probability of capsize versus wave height where the probability varies between 0 and 1 within the region. Inspecting the time series of the simulations with no capsize either the accumulation of floodwater on the car deck is too slow to result in capsize within 30 minutes or the floodwater seem to have reached a steady state with equal ingress/egress as time progresses (for sufficiently low wave heights there will be no flooding at all of the car deck). This suggests the existence of a time independent survival wave height below which capsize events have low probability, which have also been found in previous model tests and numerical simulations, van't Veer et al. (2004) and Spanos and Papanikolaou (2007). In e.g. the present study there are no capsize events in wave heights below 2.5 m and 2.4 m for the model tests and the simulations respectively.

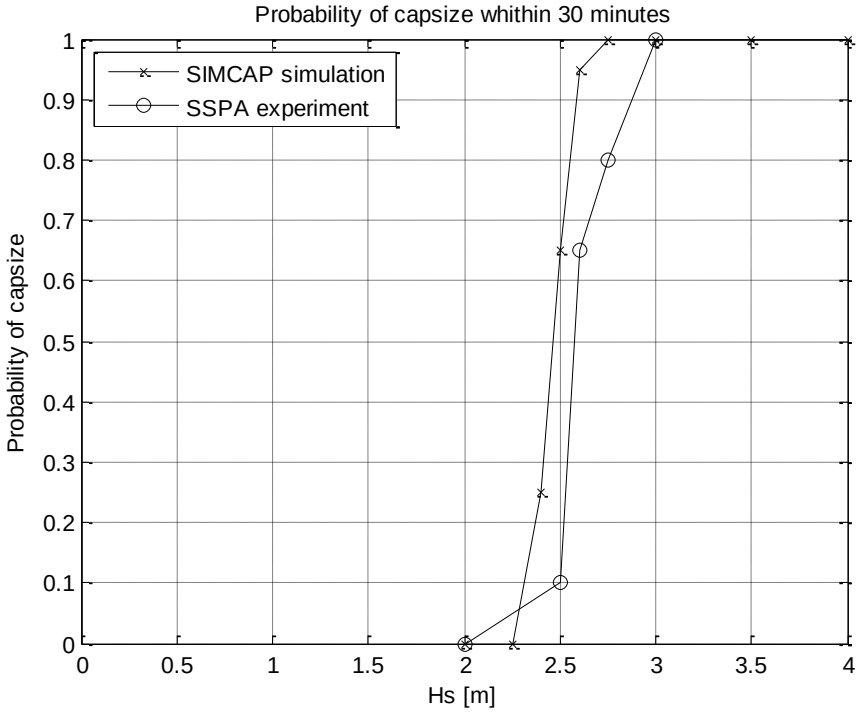

Figure 4-5 Probability of capsize within 30 minutes.

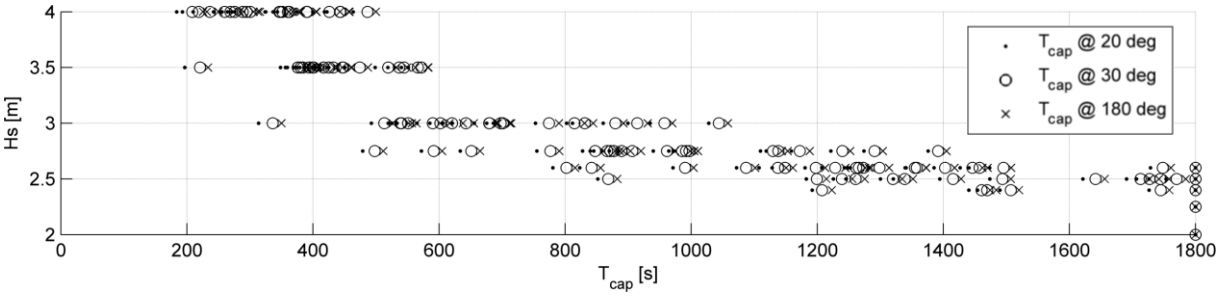

Figure 4-6 Impact of alternative definitions of T_{cap} dependent on the roll angle. Note that for each simulation the three different definitions are close compared to the spread of the different realizations.

The present study show that SIMCAP is able to reproduce, with satisfactory accuracy, the events where a RoPax ship is subjected to flooding in beam seas through a SOLAS standard damage opening and where water can be accumulated on the car deck resulting in ship capsize. This is shown through a comparison of the capsize bands of the simulations and corresponding model tests.

4.2 Progressive flooding

The capabilities of simulation of progressive flooding in calm water are validated through comparison with model tests of a box shaped barge. An in depth description of the model tests, carried out at the Ship Laboratory at Helsinki University of Technology (now Aalto University) can be found in Ruponen (2006).

The barge has tapered bow, stern and bilges and eight floodable compartments positioned slightly forward of amidships in a starboard/port symmetric configuration. A picture of the model barge and the configuration and names of the compartments are shown in Figure 4-7. The particulars of the intact model barge are listed in Table 4-2. All tests were carried out in calm water.

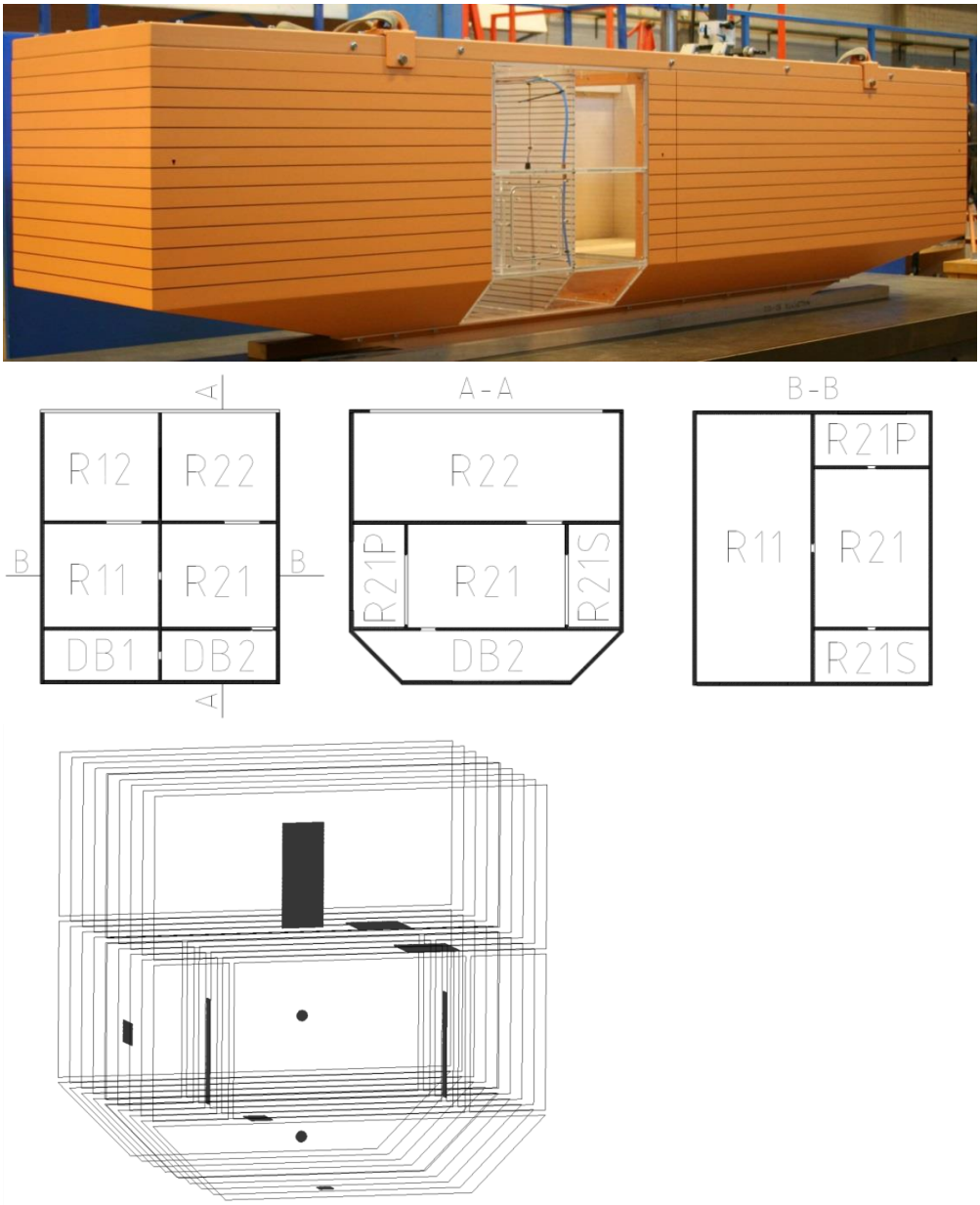

Figure 4-7 Picture of barge, compartment configuration (from Ruponen 2006) and damage openings in numerical model (below).

Table 4-2 Particulars of intact barge.

Length	4.000 m
Breadth	0.800 m
Height	0.800 m
Draft	0.500 m
Heel	0.08
Trim	0.08
Block coefficient	0.906
Volume of buoyancy	1.450 m^3
Vertical center of gravity, KG	0.278 m

The size of the compartments and the internal openings was choosen as to obtain a flooding process similar to progressive flooding inside a passenger ship and the nominal scale of the model is 1:10. The compartments were fitted with sensors in the lowermost corners measuring the water levels. The permeability of each compatment was estimated to be 1.0. A description of internal- and damage openings together with a discharge coefficient, C_d, produced through specifically tailored experiments, that is used as an input to the simulations are listed in Table 4-3. The doors have a 10 mm doorstep clearence.

Table 4-3 Internal- and damage openings in the barge.

Name (connect)	**Size**	**Description**	**C_d**
SEA-DB2	25 mm x 25 mm	Bottom damage (closed in Test06)	0.83
SEA-R21S	60 mm x 40 mm	Side damage (closed in Test03)	0.78
DB1-DB2	D = 20 mm	Broken pipe (N/A in Test06)	0.80
DB2-R21	60 mm x 40 m	Manhole (closed in Test06)	0.78
R21-R21S	20 mm x 200 mm	Partly open/leaking door	0.75
R21-R21P	20 mm x 200 mm	Partly open/leaking door	0.75
R21-R11	D = 20 mm	Broken pipe	0.80
R21-R22	100 mm x 100 mm	Staircase	0.72
R11-R12	100 mm x 100 mm	Staircase	0.72
R12-R22	80 mm x 200 mm	Open door (closed in Test06)	0.72

In the model experiments all compartments, with the exception of the aft double bottom compartment DB1, was considered to be fully vented i.e. the air pressure in the compartments is atmospheric at all times. DB1 can however only be ventilated through the damage opening DB1-DB2 which will eventually be below the water level of DB2 during the flooding process. This will hinder air to escape from DB1 which will slow down the flooding during an air compression phase and finally stop the flooding when an equilibrium between water and air pressure in DB1 have been reached. In the simulations all compartments are fully vented. A time step of 0.08 seconds is used in all simulations.

Two damage cases are simulated: Test03 is a bottom damage where all compartments are subjected to flooding and Test06 is a side damage where the double bottom compartments are intact and the water tight door on the upper deck is closed. At the start of the simulations the intact barge is floating at equilibrium when the damage opening appears. In the experiment a plug was pulled out of the opening which was considered to have the same effect.

In Test03 the barge is flooded through the damage opening in DB2 and then progressively to all compartments through the internal damage openings. Figure 4-8 shows the trim and sinkage of the barge during model test and simulation. The over estimation in the simulations can be explained through the lack of air compression when DB1 is flooded which leads to a quicker flooding and also that DB1 is completely filled as opposed to the model tests where DB1 was only filled to about half its volume when equilibrium was reached, Figure 4-9. There is a good agreement of the flooding of DB2 between simulation and experiment. The flood rate is high due to the large pressure head at the onset of the damage and is largely unaffected by the flooding into DB2 which has only reached a level of about 10 mm when DB2 is completely filled, Figure 4-9.

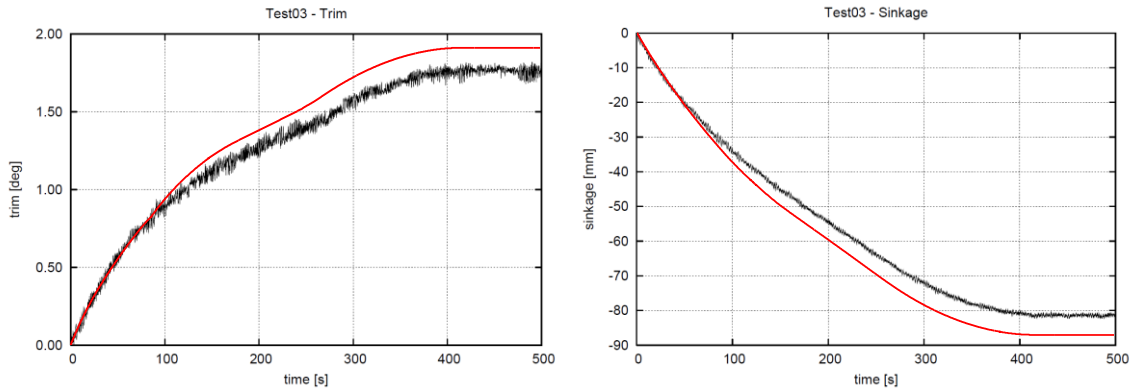

Figure 4-8 Trim (left) and sinkage of the simulation (red line) compared to model test.

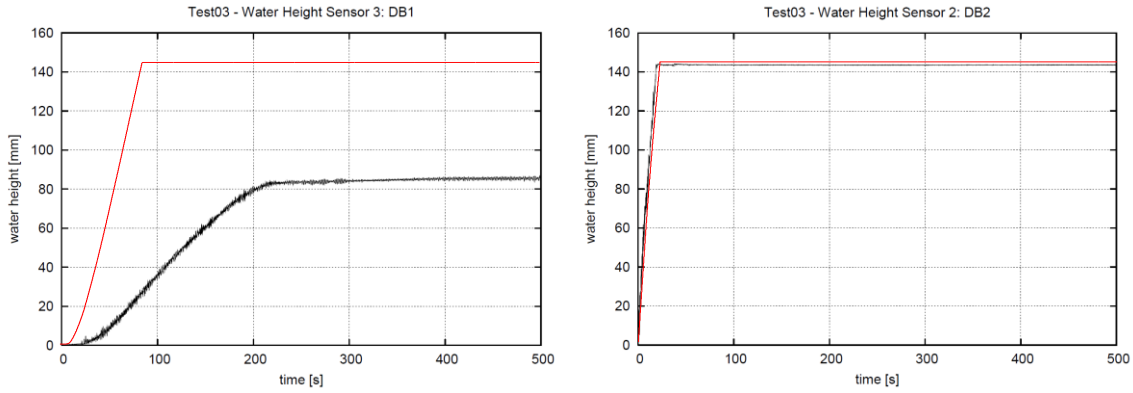

Figure 4-9 Flooding of the double bottom, DB1 (left) and DB2, of the simulation (red line) compared to model test. The difference in DB1 is due to an air compression effect, not accounted for in the simulation.

When DB2 is filled upflooding to R21 on the lower deck starts followed by flooding of the side compartments R21P/S a few seconds later when water level reaches the doorsteps, Figure 4-9 and Figure 4-10. At 69 seconds flooding of R11 commences as the broken pipe R21-R11 is reached by the floodwater and the flood rate of R21 (and R21P/S) consequently decreases slightly. At 86 seconds DB1 is compleatly filled and all floodwater entering the barge will go into R21 and the floodrate abruptly increases again. In the model test DB1 is flooded much slower and the flooding have no abrupt stop but a rather smooth appearance gouverened by the air compression phase, Figure 4-9.

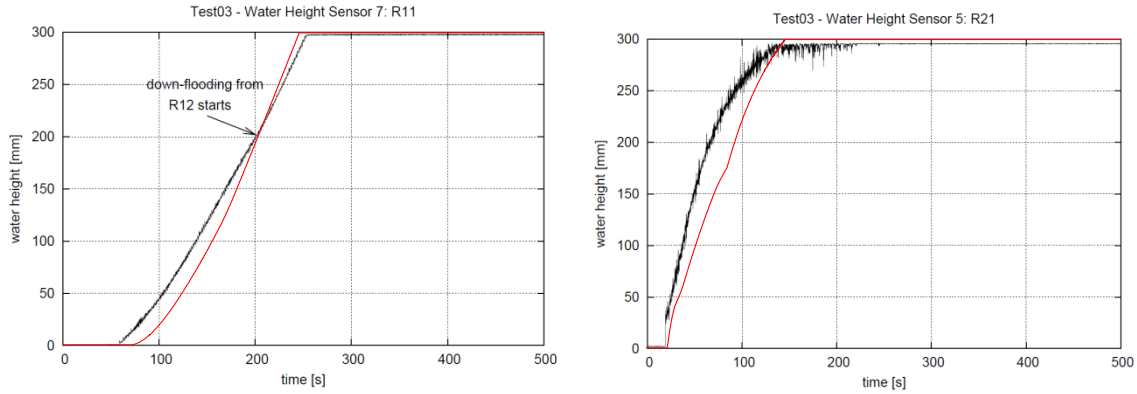

Figure 4-10 Flooding of the lower deck, R11 (left) and R21 of the simulation (red line) compared to model test.

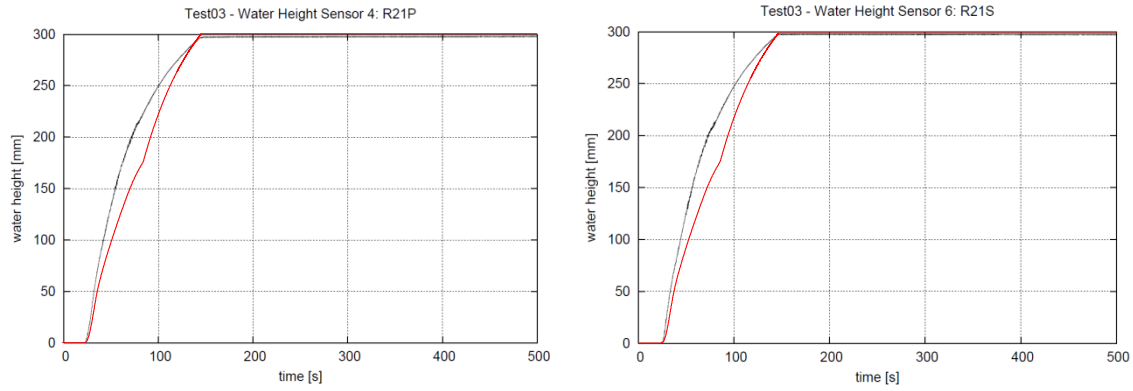

Figure 4-11 Flooding of the side compartments, R21P (left) and R21S of the simulation (red line) compared to model test.

In Figure 4-12 the flooding of compartments R12 and R22 on the upper deck is shown. R22 starts to flood from below through the staircase at 146 seconds when R21 is full. R12 starts to flood through the open door at 163 seconds but the water height in R12 remains too small to be seen in the figure before 246 seconds due to downflooding to R11. At this time R11 is completely filled and all additional floodwater will go into R12 and R22 until final equilibrium is reached at around 420 seconds.

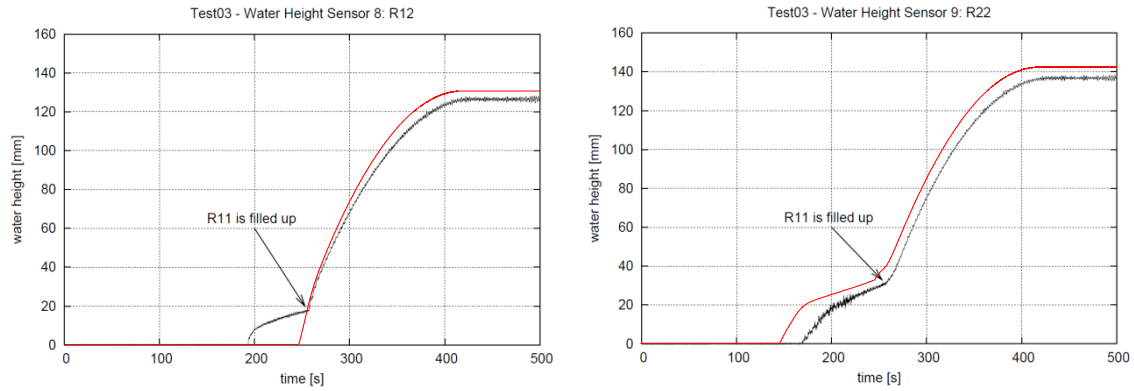

Figure 4-12 Flooding of the upper deck, R12 (left) and R22 of the simulation (red line) compared to model test.

In Test06 the barge is flooded through the side damage into R21S and then progressively to the compartments above the double bottom. The door on the upper deck is however closed. All the flooded compartments are ventilated and the correspondance of trim and sinkage between model test and simulations is high, Figure 4-13.

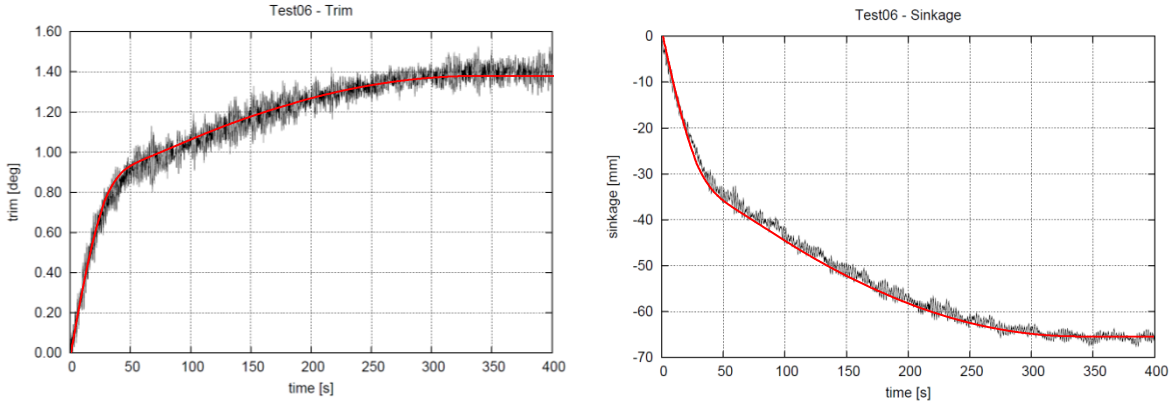

Figure 4-13 Trim (left) and sinkage of the simulation (red line) compared to model test.

The damage opening is longitudinally located in line with the doors leading to R21 and R21P, and the center is 185 mm below the waterline in the intact condition, Figure 4-7. During the first 20 seconds of the model test a water jet from the damage opening, partly going directly through the open door leading to R21 and splashing down on the deck in a rather violent manner, allowed for an almost simultaneous flooding of R21 and the side compartments. This is not captured in the simulation where R21S is flooded very rapidly followed by R21 and R21P. The difference of the test and simulation in the flooding of these comparments is not great but can be seen in Figure 4-15, where R21S is flooded more rapid then in the test and R21P is slightly lagging. This effect will result in a transient starboard heel in the simulation where the barge in the model test rolls more or less around zero heel due to the rather violent flooding, Figure 4-14.

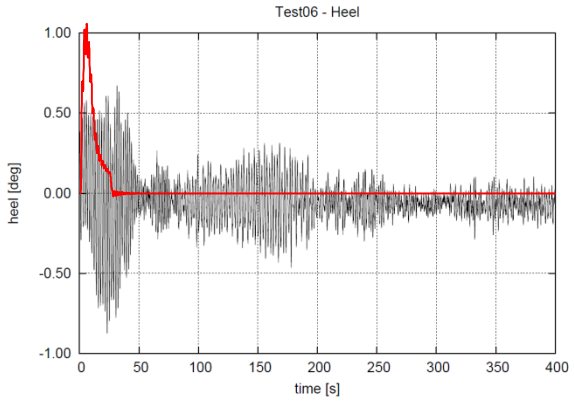

Figure 4-14 Heel in Test06 of the simulation (red line) compared to model test.

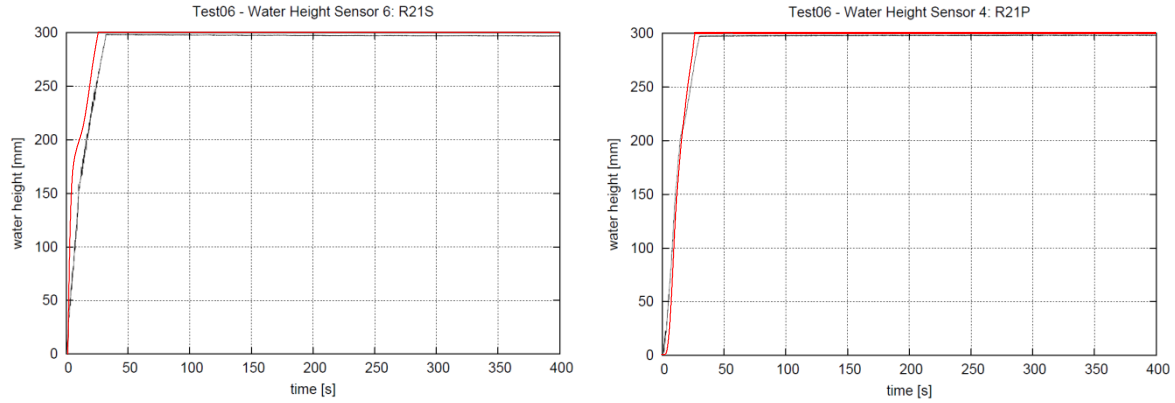

Figure 4-15 Flooding of the side compartments, R21S (left) and R21P of the simulation (red line) compared to model test.

R11 starts to flood when the water in R21 has reached the broken pipe at the water height of 140 mm at 11 seconds, Figure 4-16. At 27 seconds R21 is filled and up flooding to R22 starts and when R11 is filled at 183 seconds up flooding to R12 starts, Figure 4-17.

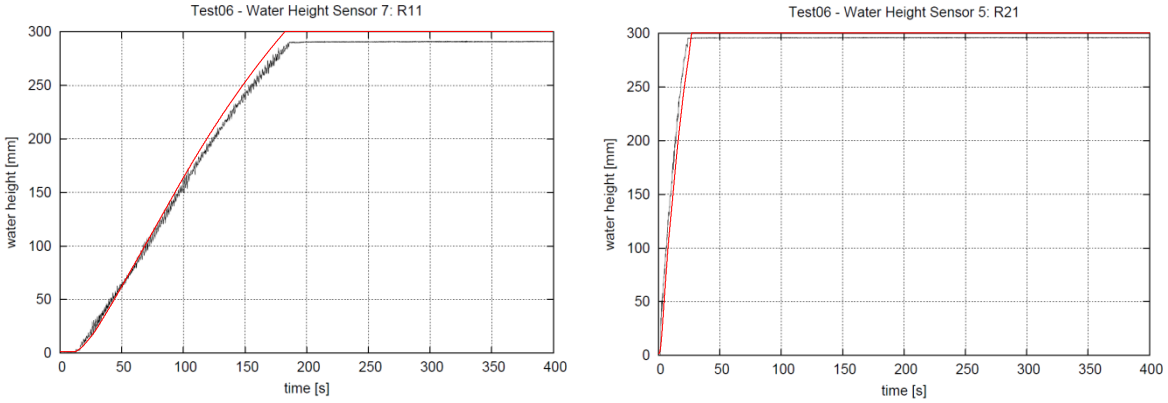

Figure 4-16 Flooding of the lower deck, R11 (left) and R21 of the simulation (red line) compared to model test.

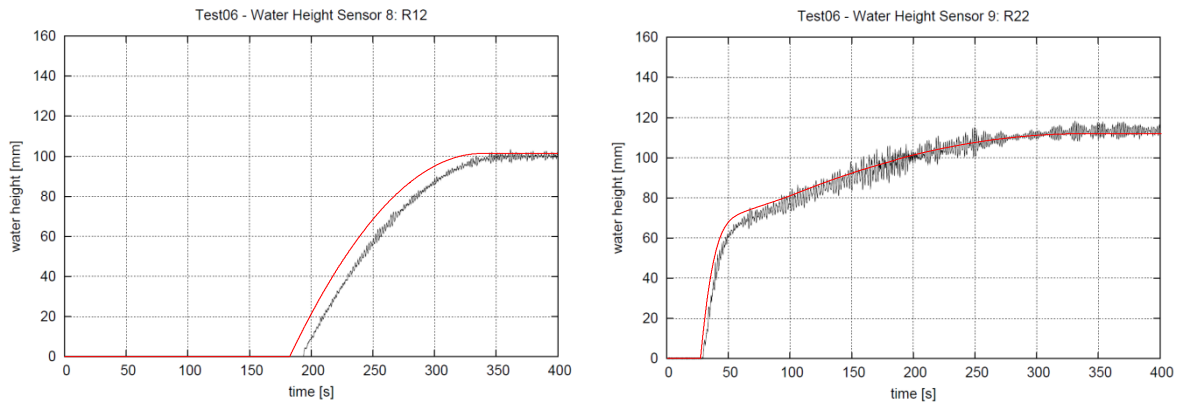

Figure 4-17 Flooding of the upper deck, R12 (left) and R22 of the simulation (red line) compared to model test.

In SIMCAP the openings have no extension in the normal direction of correspondig plating. They are positioned at the center of the platings which is 10 mm thick in the physical barge model. In general the effect of this is considered to be very small but in the present case, with a plate thickness of 100 mm full scale it could have some influence on the results.

Comparison with a simulation of Test06 using a more sophisticated method

Gao et al. (2011) presents a simulation of Test06 where a more sophisticated method of simulating the water flow based on solving the Navier-Stokes (NS) equations is used. Here the laminar NS equations were solved using the volume of fluid (VOF) method to capture the free water surface. Plots of the water heigths and the barge motions from the NS simulation and model tests, where also the SIMCAP results have been inserted, are presented in Figure 4-18 to Figure 4-22.

In general the NS simulation show a better agreement with the model test. This is particularly evident in Figure 4-20 where the water height in R21S, the compartment with the side damage is located, is shown. The rather violent first 20 seconds of the test described above could be better captured by the NS simulation which can reviel details of the water flow, that also seem to correspond well with pictures from the model tests, which are not captured at all by the SIMCAP simulation.

However as the flooding progresses and the violent flow at the beginning settles down, the discrepancies between the simulation methods (and the model test) is becoming very small which can bee seen in e.g. Figure 4-18 where the trim and sinkage of the barge is presented.

The SIMCAP simulation and the NS simulation were both performed on a personal computer of similar capacity (Intel Core2, 3,0 GHz processor) and the ratio of the simulation time between NS and SIMCAP simulations is about 10^4.

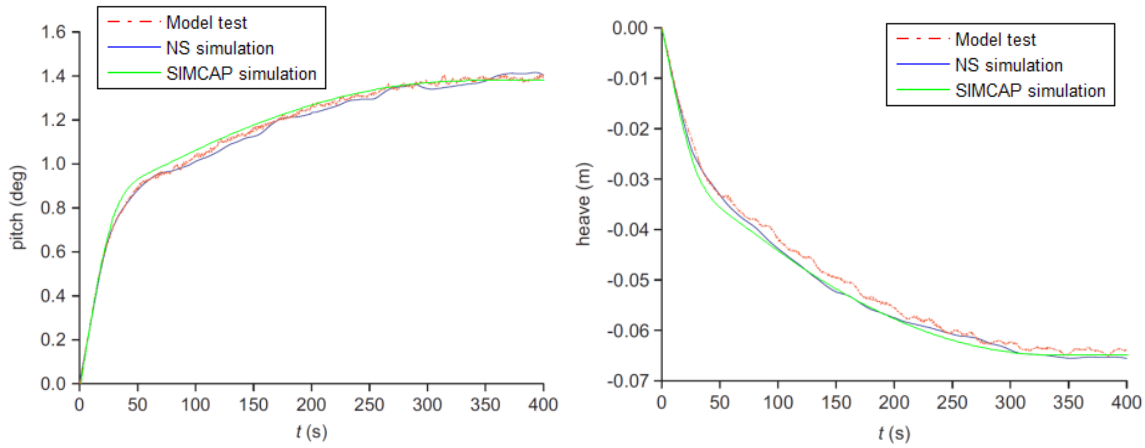

Figure 4-18 Trim (left) and sinkage of Test06.

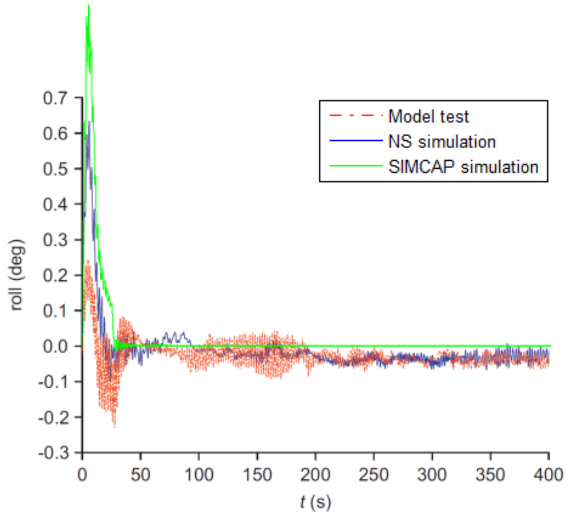

Figure 4-19 Heel in Test06.

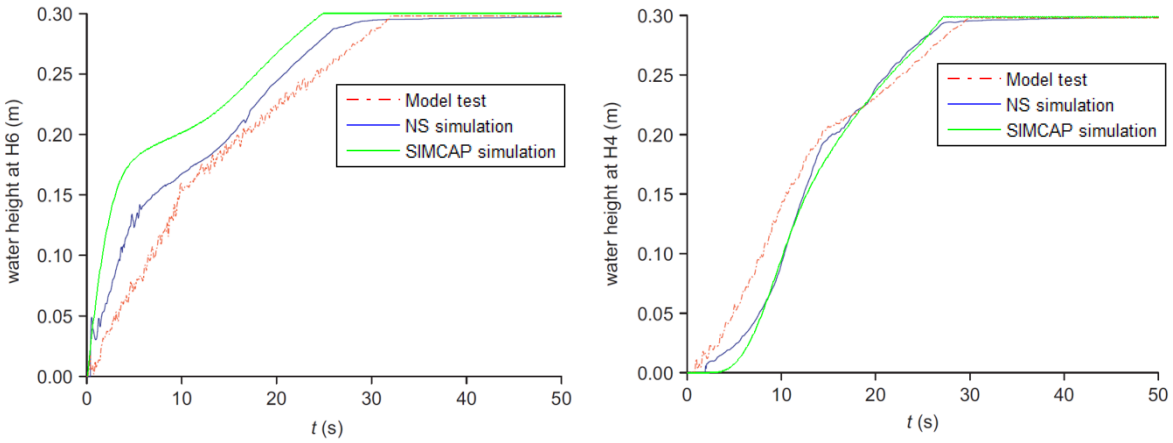

Figure 4-20 Flooding of the side compartments, R21S (left) and R21P, in Test06.

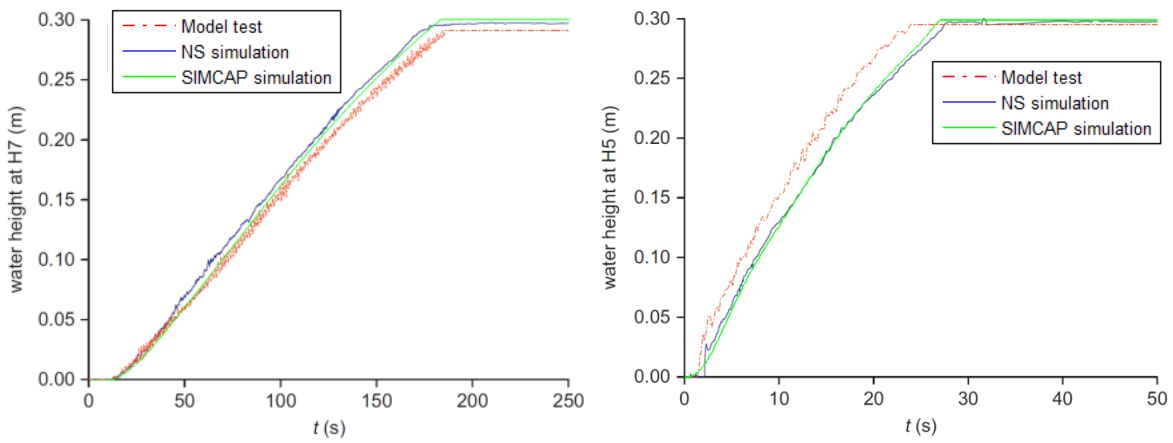

Figure 4-21 Flooding of the lower deck, R11 (left) and R21.

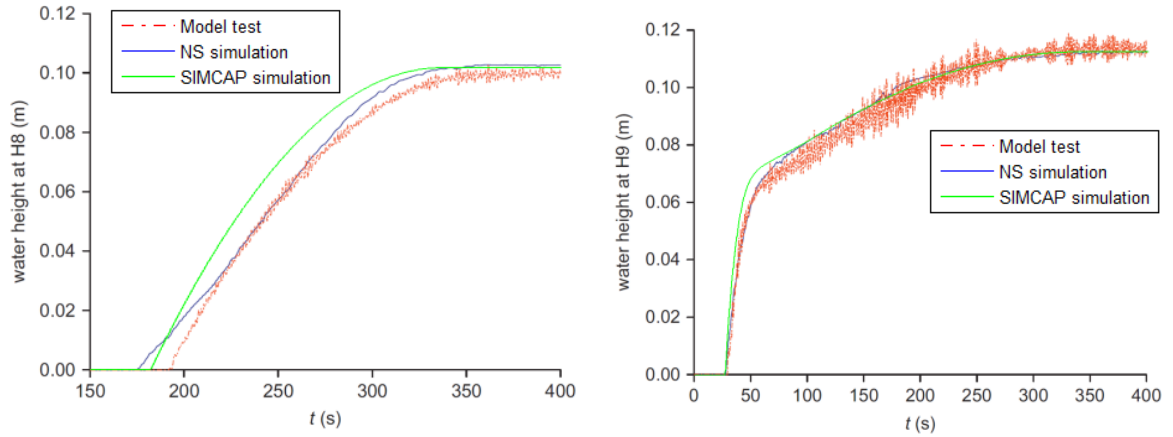

Figure 4-22 Flooding of the upper deck, R12 (left) and R22.

4.3 Parametric roll

Background

An increasing attention within the research community to the phenomenon of parametric roll has been given in the last decades following an increase of accidents and reported near-accidents. Large container ships and Pure Car and Truck Carriers (PCTC) have been reported to experience dangerously large roll angles developed in a very short time, in some cases only a few wave encounters. One example is the APL China incident in 1998 where more than sixty percent of the cargo was lost or damaged due to parametric roll. More recent examples of ships encountering parametric roll resonance is the Maersk Carolina in 2003 where more than 130 containers were lost and the PCTC Aida in 2004 where the time series of the roll motion also has been recorded on board (Hua et al.2006). Parametric rolling potentially has a very high cost in terms of damaged or lost cargo and even damage and loss of the ship and its crew.

The phenomenon of parametric roll has been recognized and investigated both by numerical and experimental models by naval architects for more than fifty years (Paulling 2006). The earlier work has been mainly focused on smaller working ships and costal cargo ships. More recent accidents with larger ships have both increased and shifted the focus of interest the recent decades, see e.g. Umeda (2008), Spanos and Papanikolaou (2009a) and Brunswig (2006).

The most basic explanation of the phenomenon of parametric roll will include the phenomenon of transverse stability variations experienced when a ship travels in longitudinal waves and the natural frequency of roll of the ship. A ship in a wave of approximately the same length as the ship will have an increased stability, compared to the stability in calm water, when two wave crests are close to the perpendiculars. This is due to the increased water line beam in the flared ends of the ship whereas the beam amidships is more or less constant. With wave troughs at the perpendiculars the ship will be less stable by the same arguments. The stability of the ship will vary between these extremes during a wave encounter and the effect is more pronounced for large flared ships such as modern container ships, PCTC's and some passenger ships.

In longitudinal waves the ship will not be excited in roll due to geometrical symmetry. In practice however some disturbance, e.g. a wind gust or some oblique waves, will always be present causing the ship to start rolling at the natural frequency. Now, if the frequency of encounter of the longitudinal waves is around twice the natural roll frequency parametric rolling may occur where the transverse stability is high when the ship is rolling towards upright and low rolling away from upright in a self-amplifying manner, Figure 4-23.

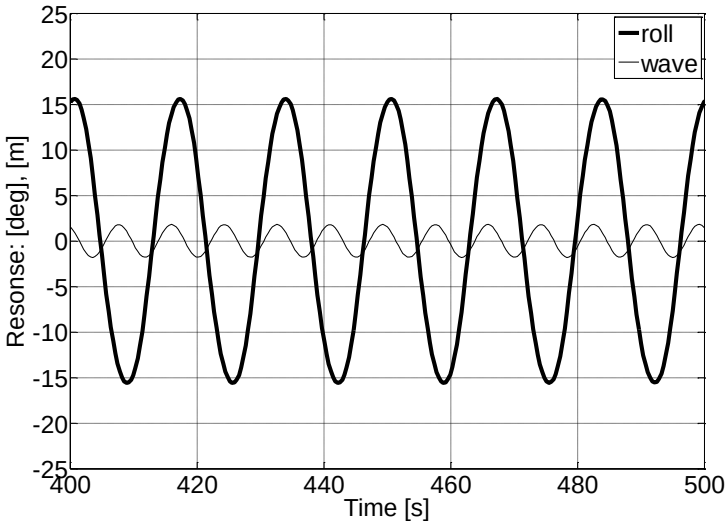

Figure 4-23 Typical simulation result of parametric rolling in regular waves. Wave elevation at the center of gravity (close to amidships) and the stability is high rolling towards upright and low rolling away from upright.

Apart from the above the roll damping of the ship is important for the susceptibility of parametric roll. If the energy loss from roll damping is greater than the energy gain due to the rolling with stability variations parametric roll will not develop.

The most basic way to examine parametric roll is by the assumption of a sinusoidal GM variation put into a linear one degree of freedom roll equation. After some rearrangement and substitutions the Matheiu equation can be derived. By varying the parameters of the Mathieu equation the stability of the equation can be studied through the well known Ince-Strutt diagram. The unstable regions of the diagram correspond to possible parametric roll, see e.g. ABS (2004).

Through the Mathieu equation an estimate of the susceptibility of occurrence of parametric roll can be made. However, no information about the severity, e.g. growth and steady state of roll, can be found from this approach. There is a need for more sophisticated methods in order to assess and understand the phenomena of parametric roll. A first step of refinement would be the inclusion of a representation of the ships righting ability at large roll angles e.g. through an analytical expression of the righting moment, e.g. Bulian (2008), or through direct integration of the pressure on the submerged part of the hull, e.g. Hua (1995). Other refinement could be to include the coupling to other degrees of freedom e.g. heave, pitch and surge and a proper representation of the roll damping. The refinements will of course come at a cost in cpu time, especially when closed form expressions are abandoned.

Validation study

An international benchmark study on the performance of numerical simulation tools regarding prediction of parametric roll was performed during 2008-2009, Spanos and Papanikolaou (2009a). The study comprised the simulation of motions of a container ship in predominantly longitudinal waves. The setup of a total of 22 test cases, see Table 4-4, were presented to the 13 independent participants prior to the study. Model tests of the test cases had been done but corresponding results from these tests were not known to the participants until all simulation results had been submitted to the benchmark coordinator. There was one exception, a roll decay test (T01) for one of the two loading conditions. The participants had the opportunity to use this test to determine the roll damping used in the simulation codes.

Table 4-4 Test cases of the benchmark study.

TEST	GM [m]	HEADING [deg] (180=head waves) (0= following waves)	Fn	Wave Height [m]	Wave Period, (T_p) [s]	Description
T01	1.38	-	0.00	-	-	Roll decay (calm water)
T02	»	180	0.08	3.6	10.63	Regular (1harmonic)
T03	»	»	»	5.7	»	»
T04	»	»	0.12	3.6	»	»
T05	»	»	»	5.7	»	»
T06	»	»	»	2.4 2.4 2.4	10.63 9.66 11.55	Group (3 harmonics)
T07	»	»	»	4.0 1.0 1.0	10.63 9.66 11.55	»
T08	»	»	»	5.0	»	Irregular (JONSWAP, γ=3.3)
T09	»	160	»	3.6	»	Regular (1harmonic)
T10	»	»	»	5.7	»	»
T11	»	»	»	4.0 1.0 1.0	10.63 9.66 11.55	Group (3 harmonics)
T12	1.00	-	0.00	-	-	Roll decay (calm water)
T13	»	0	0.08	3.6	8.00	Regular (1harmonic)
T14	»	»	»	6.0	»	»
T15	»	»	0.04	3.6	»	»
T16	»	»	»	6.0	»	»
T17	»	»	0.04	2.4 2.4 2.4	8.00 7.11 8.89	Group (3 harmonics)
T18	»	»	0.08	»	»	»
T19	»	»	»	5.0	8.00	Irregular (JONSWAP, γ=3.3)
T20	»	180	0.08	»	12.12	Regular (1harmonic)
T21	»	»	0.12	»	»	»
T22	»	»	0.08	4.0 1.0 1.0	12.12 10.77 13.47	Group (3 harmonics)

The benchmark ship is the container ship ITTC-A1 with main particulars and loading conditions listed in Table 4-5. Other parameters of the test cases were forward speed, heading, wave height and wave period. For most of the cases longitudinal regular waves were used but there were also cases with irregular waves and wave groups with three harmonics as well as a few cases with waves at a 20° angle on the bow.

Table 4-5 Main particulars and loading conditions of the ship used in the benchmark study.

Item	ITTC-A1
Length: L_{pp}	150.0 m
Breadth: B	27.2 m
Depth: D	13.5 m
Draught at FP: T_f	8.5 m
Mean draught: T	8.5 m
Draught at AP: T_a	8.5 m
Block coefficient: Cb	0.667
Prismatic coefficient: Cp	0.678
Water plane coefficient: Cw	0.787
Wetted surface area: S	5065 m^2
Loading condition 1	
Metacentric height: GM	1.38 m
Roll radius of gyration: I_{xx}	10.33 m
Pitch radius of gyration: I_{yy}	37.5m
Loading condition 2	
Metacentric height: GM	1.00 m
Roll radius of gyration: I_{xx}	10.33 m
Pitch radius of gyration: I_{yy}	38.2 m

In all test cases the ship was restrained to move in only three degrees of freedom; roll, heave and pitch and thus does not suffer from uncertainty in course and speed keeping. Also any influence of natural speed variations in waves is excluded in the model tests and simulations.
All test cases were simulated by the SIMCAP code and the roll angle was set to one degree at the start in order to trigger a possible parametric roll. The results presented herein are from simulations made after the completion of the benchmark study and includes a correction of an error, discovered after the original benchmark, in the pertinent code.

The roll decay model test T01 was used to determine the coefficients of the quadratic roll damping in the numerical code. A comparison between model test and simulation after tuning is shown in Figure 4-24. The time series of the decay test of the second loading condition GM=1.00 m is not known and only the simulated result, with the damping coefficients obtained from the tuning of T01, is shown in Figure 4-25. The natural period of the test (just above 22 s, corresponds well with the simulated result, however. In the present simulations forward speed effect on roll damping is not considered due to pertinent low speeds, Froude number is not higher than 0.12, and the damping coefficients are kept constant throughout the study.

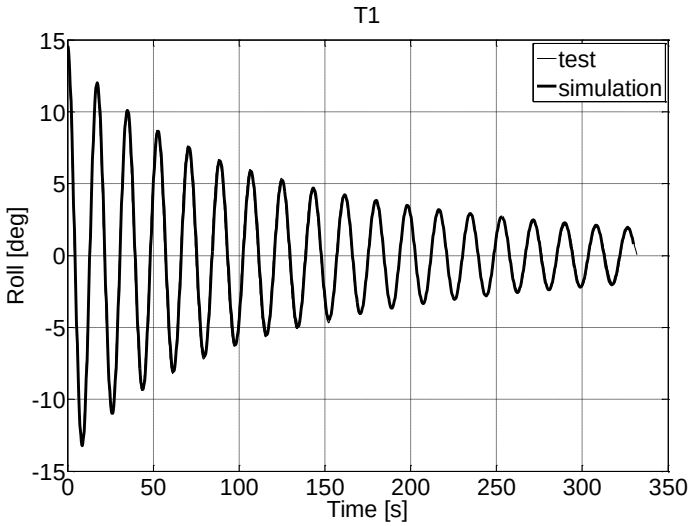

Figure 4-24 Roll decay simulation and model test for GM=1.38 m: T_{eg}=18.3 s, ω_{eg}=0.34 rad/s. (Test and simulation practically coincide.)

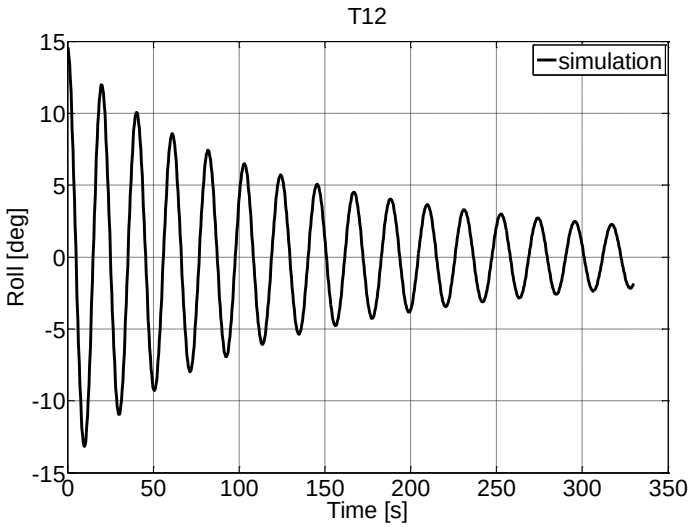

Figure 4-25 Roll decay simulation for GM=1.0 m: T_{eg}=21.7 s, ω_{eg}=0.29 rad/s

The simulations of the benchmark test cases produce time series of roll, heave, pitch and wave amplitudes. The mean roll amplitude of the steady state is used for comparison with the experimental results, Figure 4-26.

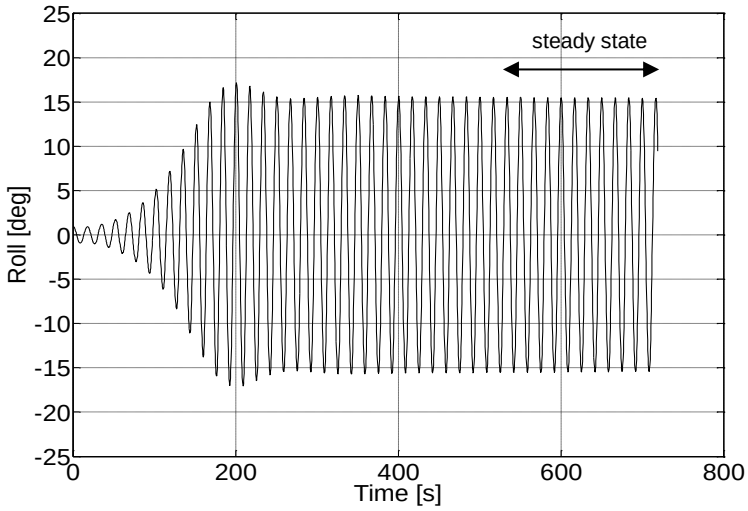

Figure 4-26 The time series of typical parametric roll development in a simulation with regular waves. The mean roll amplitude of the steady state is compared with experimental results.

It can be noted that all regular wave cases that resulted in a steady state roll angle above one degree also had a roll period equal to two encounter periods which is characteristic for principal parametric roll. The same tendency is observed also for the non-regular cases. See examples in Figure 4-23 and Figure 4-27, respectively. Figure 4-28 show the time series from an irregular seas simulation where the parametric roll is first excited by a group of waves with the right "tuning" and then decreasing and disappearing after a few minutes. Similar behaviour has been observed in actual incidents at sea and was recorded and reported in Hua et al. (2006).

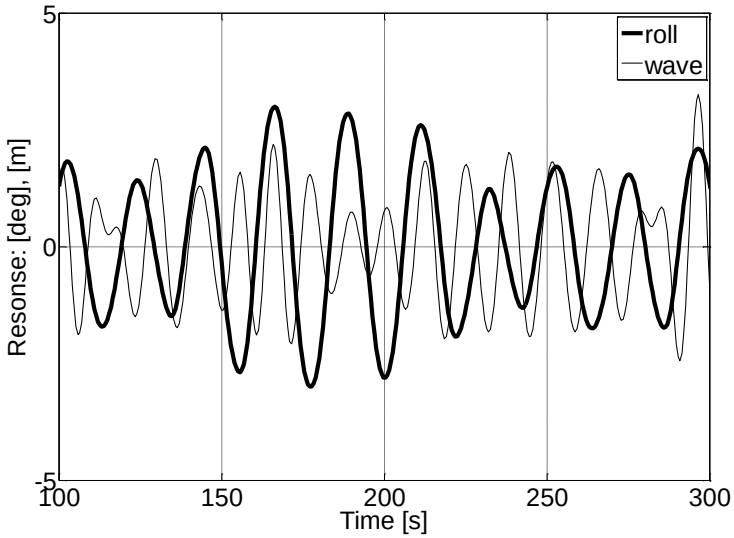

Figure 4-27 Typical simulation result from a test case with parametric rolling in irregular waves.

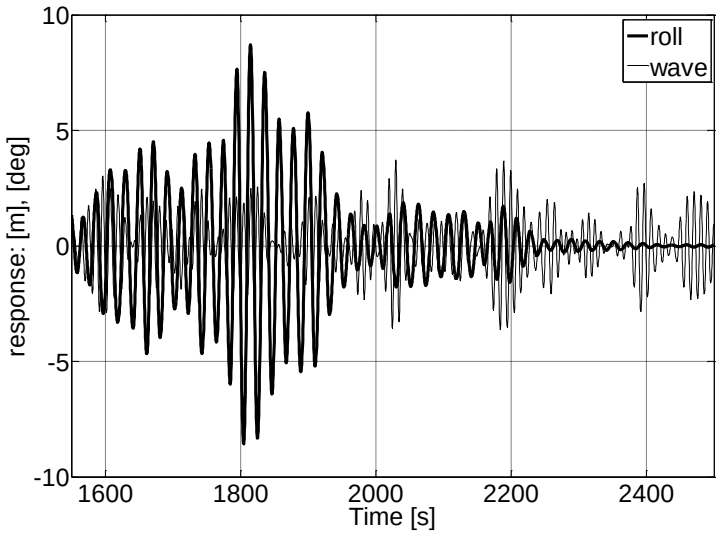

Figure 4-28 Example of parametric roll growth and decay in an irregular seas simulation.

The result of the validation is presented in Figure 4-29 where the steady state roll amplitudes of the SIMCAP simulations are presented together with corresponding model test roll amplitudes. T01 and T12 are the roll decay tests and are consequently not represented in Figure 4-29.

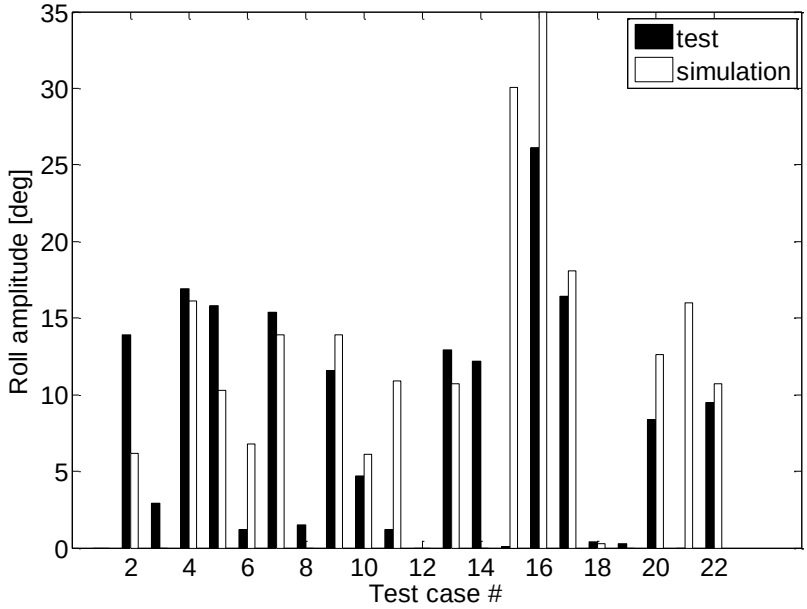

Figure 4-29 Results of the test cases from the SIMCAP simulations and model tests. T1 and T12 are the roll decay tests. The simulation of test case 16 resulted in ship capsize.

The simulations of the irregular test cases, T08 and T19, were done using three different wave realizations of each test case. The results are presented as time series of roll and wave elevation in Figure 4-30 and Figure 4-31 respectively. It is believed that additional realizations and/or longer simulations are needed in order to make appropriate comparisons with the corresponding model tests. The simulations are therefore excluded in Figure 4-29. It

can be concluded however that in two out of three simulations of T08 parametric rolling occurs and the same holds for one or possibly all three of the simulations of T19, Figure 4-30 and Figure 4-31.

For 14 of the 18 remaining cases the simulations are able to correctly predict the occurrence of parametric roll. For many of the cases there is however a rather large discrepancy of the magnitude of the steady state roll angles. There is however no obvious trends of these discrepancies, such as a consistent under or over estimation. The model test with the highest roll amplitude, T16, resulted in capsize in the simulation, Figure 4-32. Possible explanations for most of the discrepancies, as well as for the cases where the occurrence could not be predicted, is found through analyzing the results of a parameter study, where a systematic variation of wave height and wave frequency around eight of test cases are made. See further section 5.2 where also the discussion of the validation results is continued.

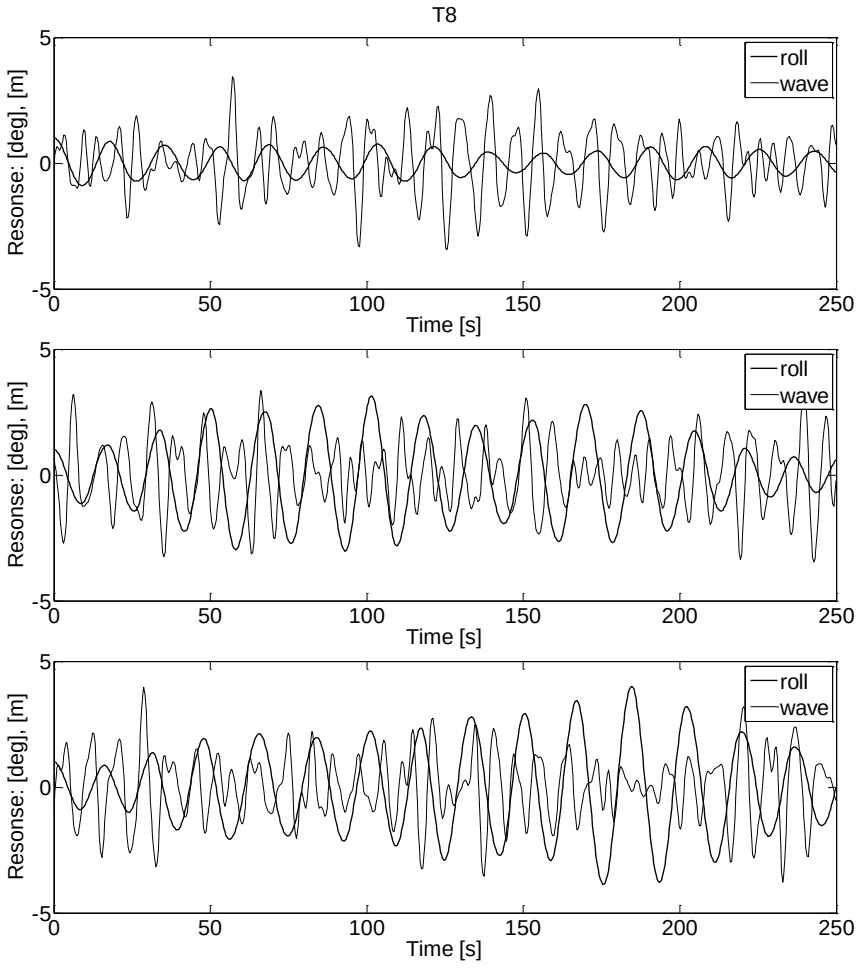

Figure 4-30 Simulation results from the three wave realizations of test case T08.

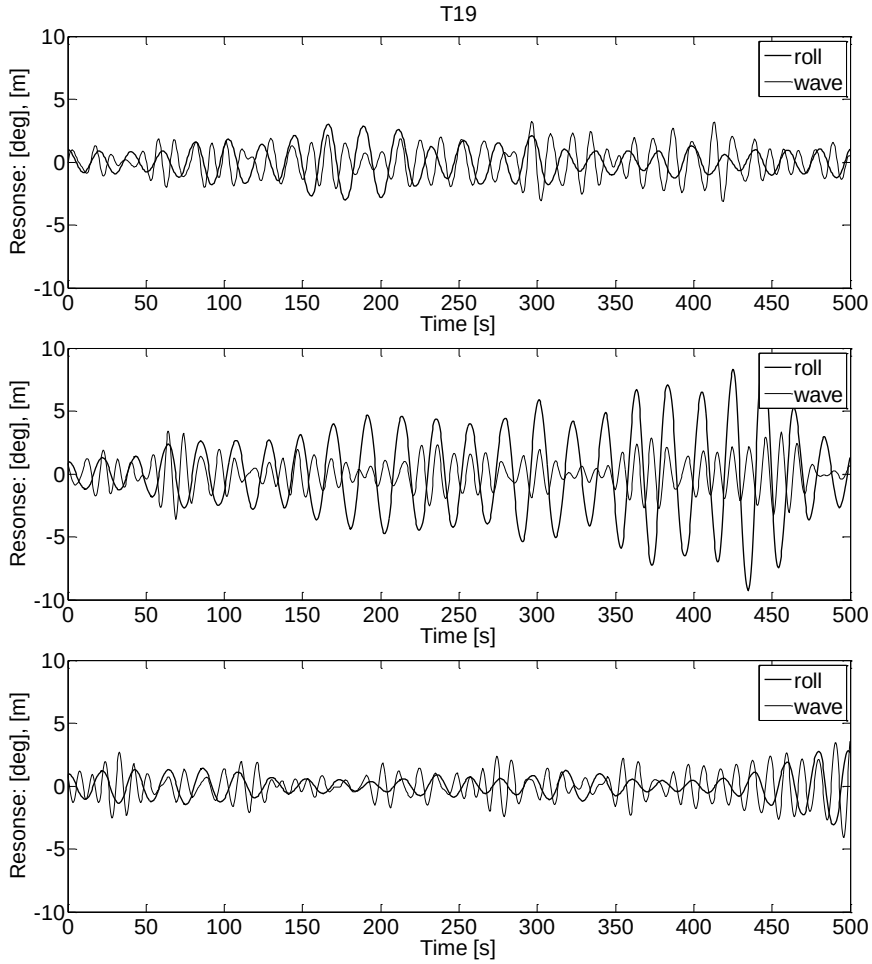

Figure 4-31 Simulation results from the three wave realizations of test case T19.

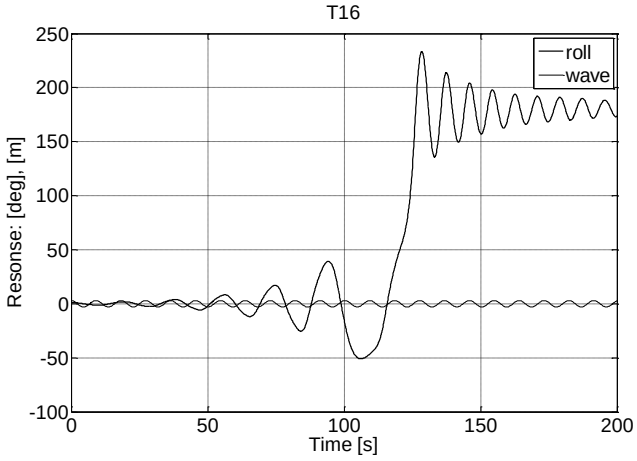

Figure 4-32 Time series of the simulation of test case T16 where the ship capsizes.

5 Applied studies

5.1 Ro-Pax capsize in waves

The ship from the validation study in section 4.1 is here used for further numerical investigation in a parameter study including an additional damage case with progressive flooding and the fitting of side casings on the car deck in order to study the reduction of capsize vulnerability of the ship.

The damage opening is the same as in the validation study while two water tight doors in the forward bulkhead of the main engine room are assumed to be open allowing for flooding of the auxiliary engine room (AE) and the engine control room/work shop (ECR/WS),

Figure 5-1 and Figure 5-2. The damage case corresponds to a 3-compartment damage.

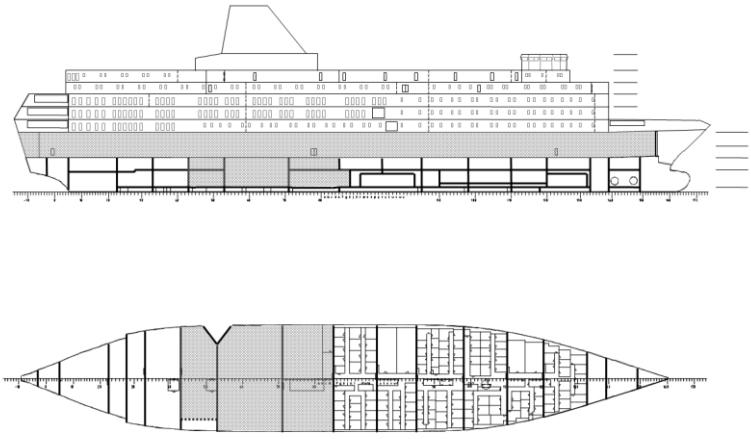

Figure 5-1 Damage case with progressive flooding of spaces forward of the main engine room

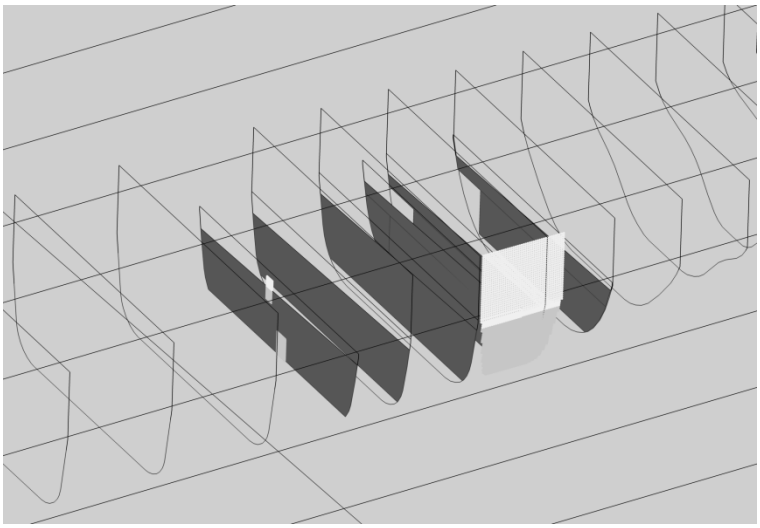

Figure 5-2 Progressive flooding trough two open water tight doors in the main engine room indicated in the left part of the figure. (The ship is floating at the damage equilibrium of the 2-compartment damage case.)

Originally the ship was built with a single casing close to the center line which only has a marginal contribution to the transverse stability in case of flooding of the car deck. Here the ship is instead fitted with side casings along the entire length of the car deck and with the same transverse subdivision as below the deck in order to improve the stability. In the simulations the casings are modeled through adjustment of the car deck width i.e. the casings will remain fully intact. This simplification is believed to only have a small impact and to maintain the trends of the results. The damage size is not dependent on the casing width i.e. the longitudinal extent of the damage opening is constant. Three different casing widths are simulated and a simulation setup is presented in Table 5-1. The combination of all parameters results in 240 simulation runs.

Table 5-1 Simulation setup

Parameter	quantity	value
H_s	3	3, 3.5, 4 m
Damage configuration	2	2-3 compartments
Width of side casings	4	0, 1, 1.5, 2 m
Spectrum seeds	10	random

The two additional spaces in the 3-compartment case have a permeability of 0.85. The ship's weight and center of gravity are assumed not to be effected by the fitting of side casings. At the simulation start the ship is intact and the damage opening appears after 10 seconds. If the ship does not capsize the simulations are stopped after three hours real time.

In Figure 5-3 all simulation results are presented in a plot of side casing width versus T_{cap}. As expected the casing width has a strong influence on the time to capsize and with two meter wide side casings all cases are survived for at least three hours. In contrast, with no side casing T_{cap} is between one and three minutes for the 3-compartment damage and less than 30 minutes with side casings of one meter for both damage cases. In Figure 5-4 the results for the most severe sea state are shown together the mean and standard deviation of T_{cap} for the different wave spectrum seeds. The indefinite results, no capsize after three hours, are excluded in this plot.

It can be noted that a two meter casing is about what is needed to accommodate stair cases, lifts, funnels, fire stations etc. and will also be very effective to reduce capsize vulnerability; an increase in T_{cap} from a few minutes to at least three hours in the cases of the 2 and 3-compartment damages. However these side casings will be far from enough to prevent capsize if more severe damages, where the car deck will be (partly) submerged in a hydrostatic sense; e.g. to maintain a positive GM after reduction from a fully developed free surface on the car deck would require casings about three times wider, reducing the width of the deck with 50%.

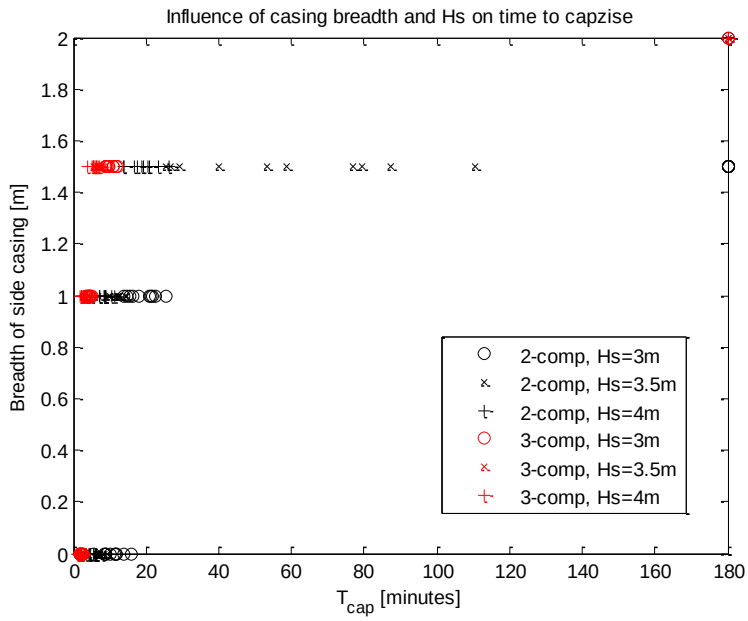

Figure 5-3 Influence of side casing width, damage case and H_s on T_{cap}.

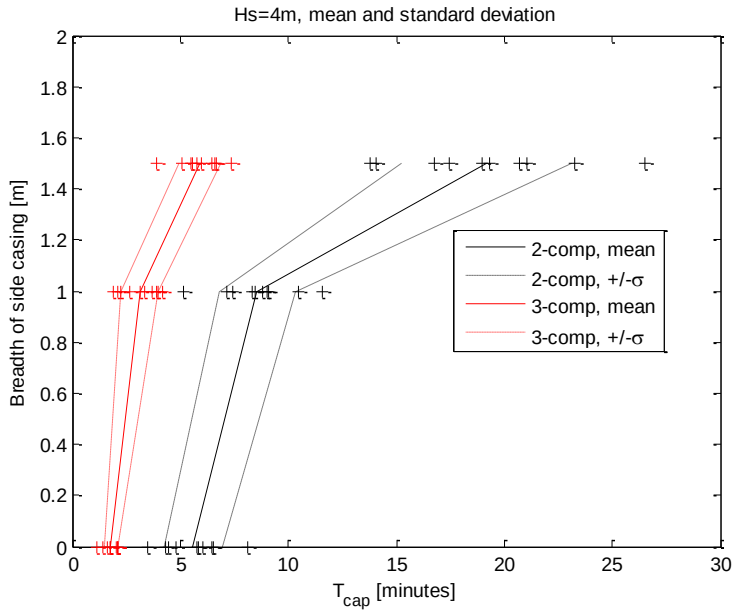

Figure 5-4 Individual, mean and standard deviations of T_{cap} for the different seeds of the four meter sea state.

Simulations in calm water, where the damage opening suddenly appears, result in time series presented in Figure 5-5. The transient behavior in these simulations arises mainly from the abrupt and dramatic added weight of from the floodwater but also from the sudden pressure loss over the large damage opening. During the flooding the ship is rolling towards the damaged side with an angle of almost three times the equilibrium heel angle while the heave and pitch show a smooth transition between intact and damage equilibrium. There is also a slight shift in sway to the port/damage direction due to the pressure loss. The abrupt change in

roll motion for the 3-compartment case just over 100 seconds is caused by the transition of the center of gravity of the flooded water within the symmetric AE as it gets completely flooded.

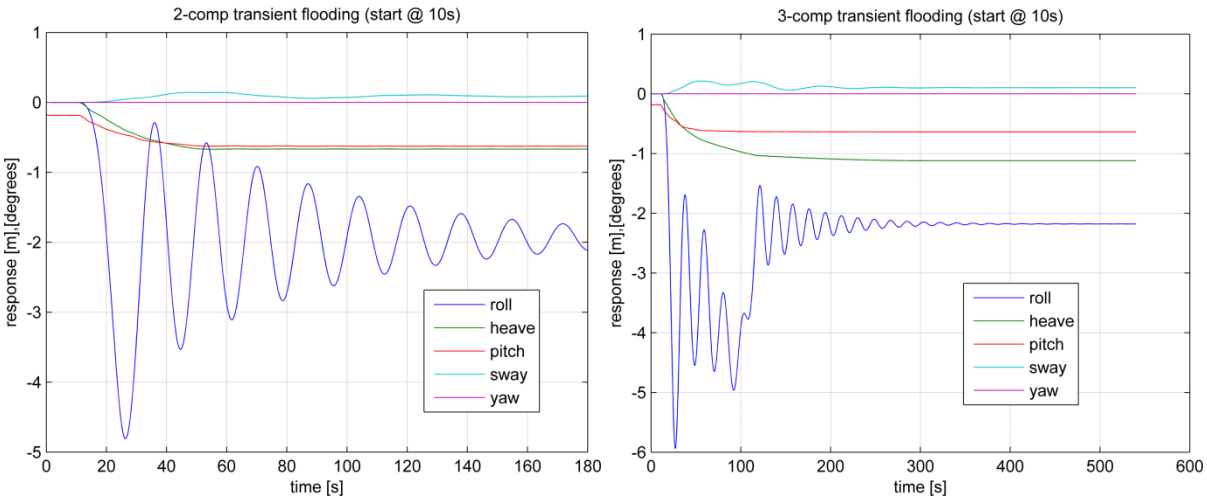

Figure 5-5 Time series of flooding simulations in calm water for the 2-compartment (left) and 3-compartment damage.

It can only be concluded here that the results of the simulation are qualitatively reasonable. However, the scale model experiments presented in de Kat et al. (2000) with a ro-pax ship with similar intact GM and the same construct of SOLAS damage opening also show a roll transient of about three times the equilibrium heel angle in a calm water testing with a sudden damage occurrence, which indicates that current simulations are also quantitatively reasonably accurate.

These roll transients could not be clearly identified in the simulations in waves, where the roll motion seemed to be mainly governed by the wave action at the onset of the hull breach. In contrast to this the flood rates of the compartments below the car deck was found to be essentially independent of the wave climate as can be seen in Figure 5-6 which shows two typical simulations of the flooded water in waves for the 3-compartment damage together with the calm water simulation.

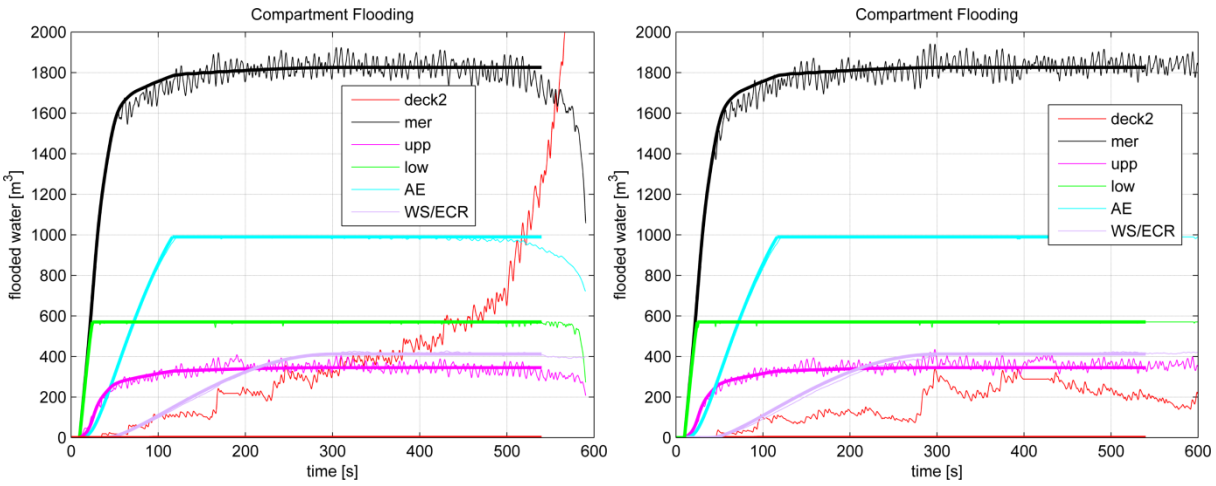

Figure 5-6 Typical time series of floodwater volumes for the 3-compartment damage. A simulation in H_s=4 m (the ship capsizes as the flooded water on the car deck increases rapidly) is shown to the left and a simulation in H_s=3 m (without capsize) to the right. The coarse lines show the floodwater from the calm water simulation.

5.2 Parametric roll

In order to investigate the mechanisms of parametric rolling and the reasons for the discrepancies between simulations and model tests in the parametric roll validation study, a parameter study is made. The study consists of a variation of wave height and wave period around eight of the discrete test cases in regular waves of the benchmark study. The test cases are defined in Table 5-2 and the results from validation are shown in Figure 5-7.

Table 5-2 Test cases of the benchmark study. The cases involved in the parameter study are indicated in grey.

TEST	GM [m]	HEADING [deg] (180=head waves) (0= following waves)	Fn	Wave Height [m]	Wave Period, (T_p) [s]	Description
T01	1.38	-	0.00	-	-	Roll decay (calm water)
T02	»	180	0.08	3.6	10.63	Regular (1harmonic)
T03	»	»	»	5.7	»	»
T04	»	»	0.12	3.6	»	»
T05	»	»	»	5.7	»	»
T06	»	»	»	2.4 2.4 2.4	10.63 9.66 11.55	Group (3 harmonics)
T07	»	»	»	4.0 1.0 1.0	10.63 9.66 11.55	»
T08	»	»	»	5.0	»	Irregular (JONSWAP, γ=3.3)
T09	»	160	»	3.6	»	Regular (1harmonic)
T10	»	»	»	5.7	»	»
T11	»	»	»	4.0 1.0 1.0	10.63 9.66 11.55	Group (3 harmonics)
T12	1.00	-	0.00	-	-	Roll decay (calm water)
T13	»	0	0.08	3.6	8.00	Regular (1harmonic)
T14	»	»	»	6.0	»	»
T15	»	»	0.04	3.6	»	»
T16	»	»	»	6.0	»	»
T17	»	»	0.04	2.4 2.4 2.4	8.00 7.11 8.89	Group (3 harmonics)
T18	»	»	0.08	»	»	»
T19	»	»	»	5.0	8.00	Irregular (JONSWAP, γ=3.3)
T20	»	180	0.08	»	12.12	Regular (1harmonic)
T21	»	»	0.12	»	»	»
T22	»	»	0.08	4.0 1.0 1.0	12.12 10.77 13.47	Group (3 harmonics)

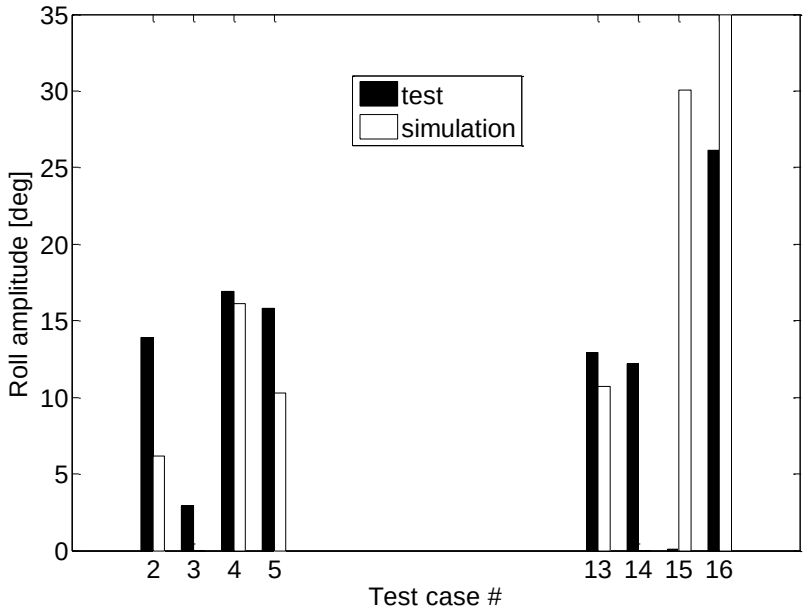

Figure 5-7 Results from the validation study of the eight test cases chosen for the parameter study.

The chosen test cases include head and following seas, both loading conditions and three different speeds and the test cases can be arranged in a matrix shown in Table 5-3. The cases in the same positions in the matrix are only separated by wave height and will thus be in the same region in the parameter study.

Table 5-3 Setup of parameter study

Ship speed, *Fn*	0.04	0.08	0.12
Head seas (Loading condition 1)		T2, T3	T4, T5
Following seas (Loading condition 2)	T15, T16	T13, T14	

The wave height and wave frequency are varied as to capture the regions of occurrence of parametric roll around the test cases. The results of the parameter study are shown in Figure 5-8. The occurrence and magnitude (steady state roll amplitude) of parametric roll are shown in a gray scale. The regions are plotted for both wave height versus non-dimensional encounter frequency (ω_e/ω_{eg}) and wave height versus non-dimensional wave length (λ/Lpp). The discrete test cases are indicated by circles in the plots. Note that the scales for the roll angle are different for the four regions and that a roll angle of 40° represent ship capsize, which occur only in the region with Fn=0.4 and following seas. The frequency of roll is half the frequency of wave encounter for all simulations with parametric roll. This is the most typical case of parametric roll and referred to as principal parametric roll.

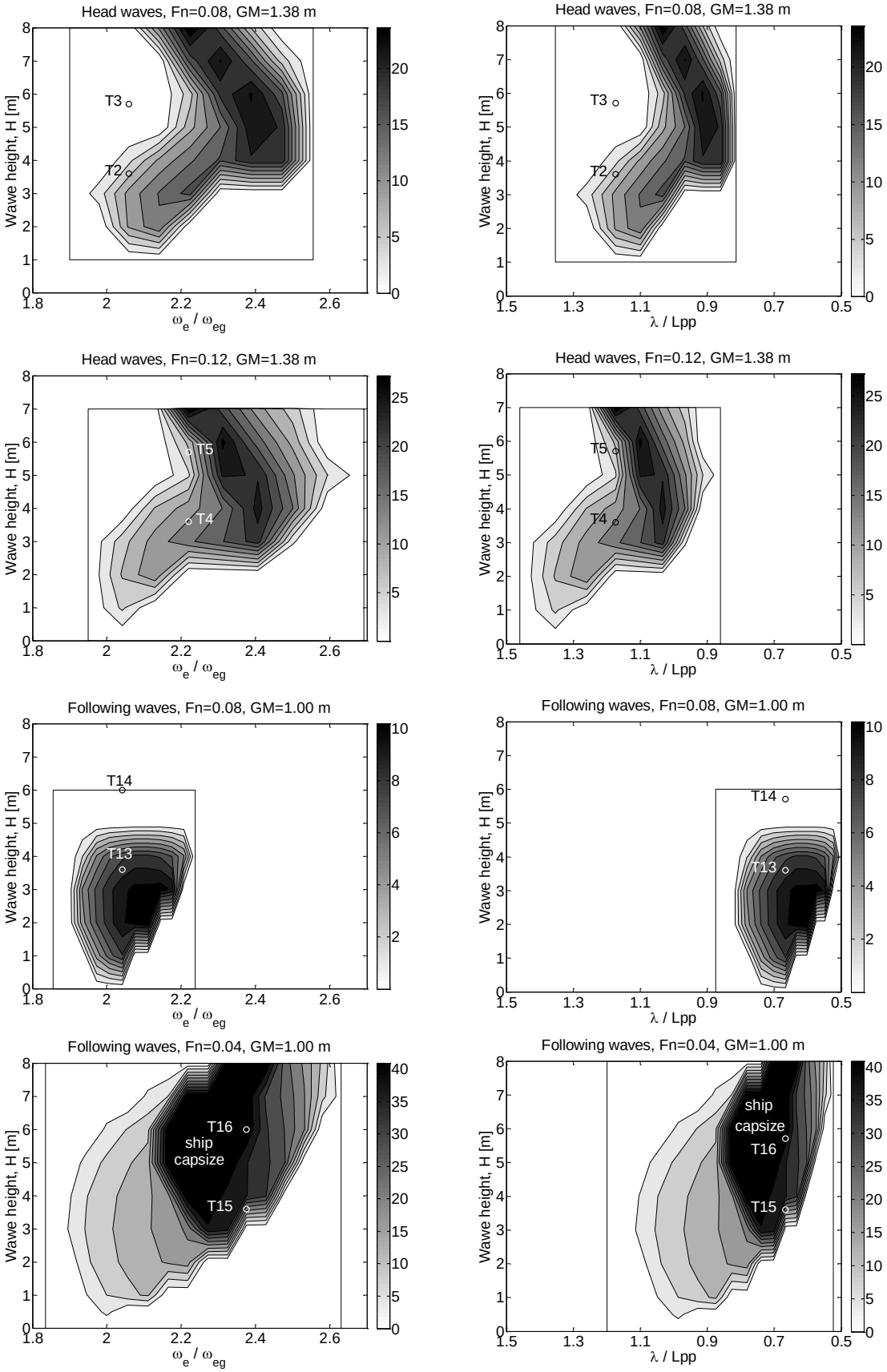

Figure 5-8 Results from the parameter study. The grey scale represents roll amplitude. The four upper plots: head waves. The four lower plots: following waves. Left: encounter frequency on abscissa. Right: wave length on abscissa. The range of parameter variation is represented by the inner boxes. The test cases of the benchmark study are indicated by circles.

In Figure 5-9 the results are condensed to only include the occurrence of parametric roll and are presented in a wave frequency versus frequency of encounter plot with forward speed as a parameter. The range of occurrence is represented by thick line segments. In the enlarged right plot the wave frequency corresponding to the ship length has been plotted as a vertical dotted line and twice the frequency of natural roll (ω_{eg}) for the two loading conditions have been plotted as horizontal dotted lines (ω_{eg} was determined from roll decay test/simulations in section 4.3).

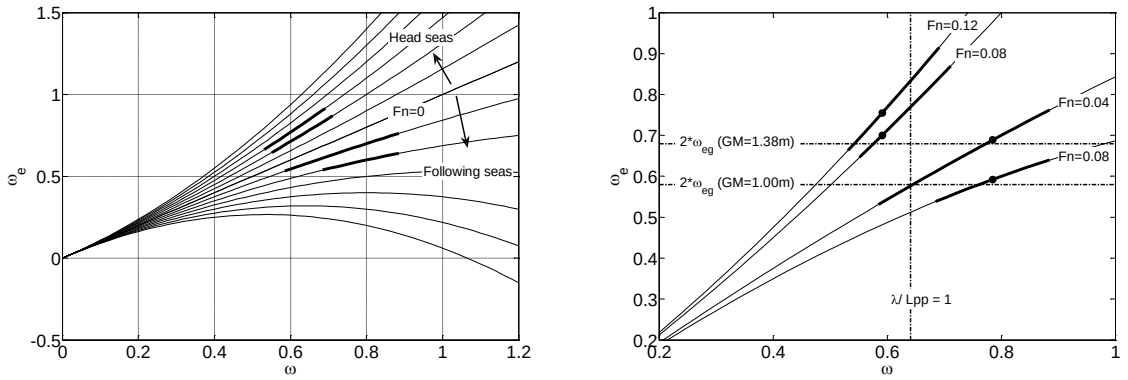

Figure 5-9 Occurrence of parametric roll from the parameter study. Left: the frequency of encounter is plotted against wave frequency for a range of ship speeds in head and following seas. On the four lines corresponding to the cases in the study the occurrence of parametric roll is indicated by thick line segments. Right: an enlargement of the left plot where also λ/Lpp=1 and twice the frequencies of natural roll have been indicated by dotted lines and the discrete cases from the benchmark study are indicated by dots.

A set of quasi-static calculations of properties known to influence parametric roll is also made in order to be used in the discussion of the simulation results of the parameter study, below.
The calculations consist of GZ curves and GM values in waves where the ship is free to trim in a "static wave" in which the pressure varies linearly with the vertical distance to the surface. Together with the hydrostatic GZ curves of the two loading conditions, curves are produced for two different wave heights, 4 m and 8 m, and with a wave length of 85% of Lpp. The longitudinal position of the ship is fixed with wave trough and wave crest amidships respectively and the curves are presented in Figure 5-10. Similarly, the quasi-static GM is calculated for a range of wave lengths, wave heights and for 16 different instances of one wave encounter, for the loading condition GM=1.00 m. The maximum and minimum values occur when wave trough and wave crest are situated amidships respectively. The span, δGM eq. (5.1), and mean values, $\overline{GM}$ eq. (5.2), are shown in Figure 5-11 and Figure 5-12.

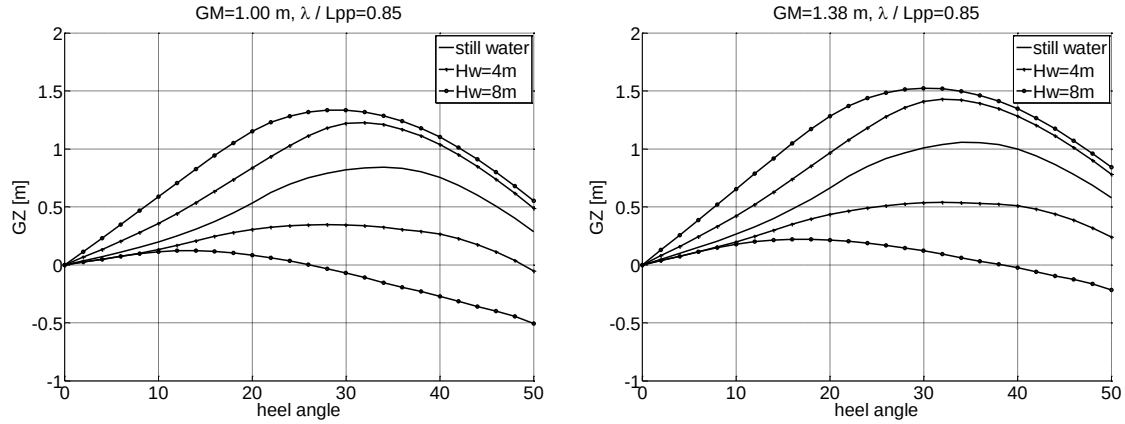

Figure 5-10 GZ curves of the two loading conditions: GM=1.00 m (left) and GM=1.38 m. Curves above still water curve: wave trough amidships. Curves below still water curve: wave crest amidships.

$$\delta GM = GM^{max} - GM^{min} \tag{5.1}$$

$$\overline{GM} = \frac{1}{T_p}\int_0^{T_p} GM(t)dt \tag{5.2}$$

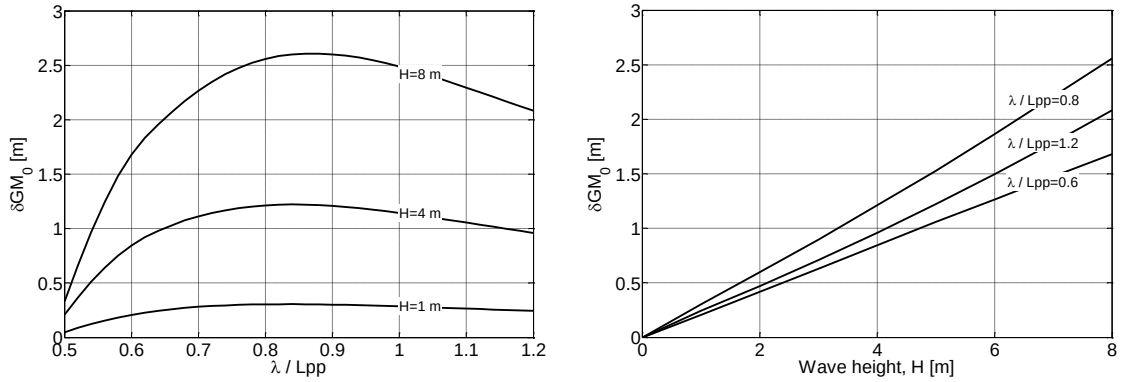

Figure 5-11 The span of GM plotted against wave length (left) and wave height. Static GM=1.00 m.

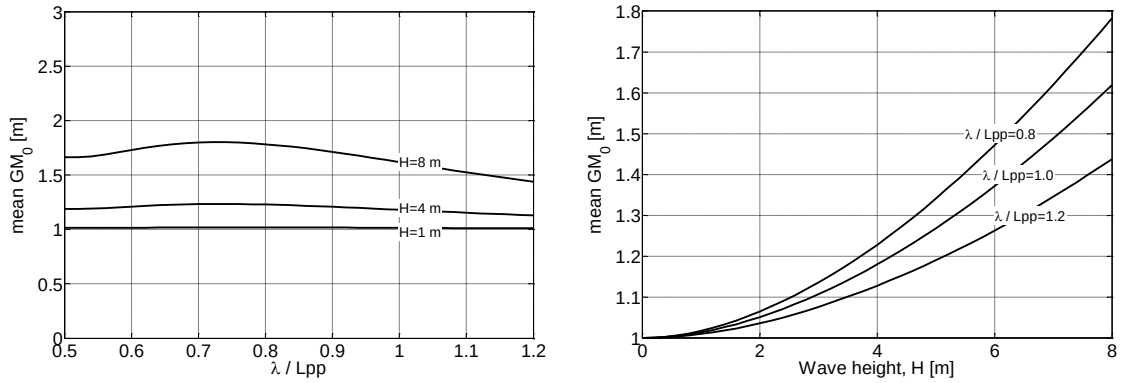

Figure 5-12 The mean value of GM during a wave encounter plotted against wave length (left) and wave height. Static GM=1.00 m.

Discussion of parameter study

All plots of Figure 5-8 show a single continuous area where parametric rolling occurs but show otherwise little resemblance. Some common observations can however be made:

a) The largest roll angles occur at frequencies larger than the principal ratio $\omega_e/\omega_{eg}=2$. When parametric roll occur at low wave heights the frequency is close to $\omega_e/\omega_{eg}=2$, however.
b) Starting from the lowest wave heights the largest roll angle for each wave height is shifted towards higher frequencies up to the maximum roll angle, i.e. there is a rightward upward trend of parametric roll occurrence in the plots.
c) There are abrupt changes in roll angle in the lower right boundaries of occurrence.

A couple of observations can also be made that are common to some but not all of the plots:

d) The largest roll angles occur at a wave length $\lambda/Lpp<1$ for the following seas cases.
e) In the Fn=0.08 following seas case the roll angle starts to decrease for wave heights above 3 m and the parametric roll disappears completely for waves above 5 m. This behavior is also partly present for the other cases in the lower frequency range of parametric roll.

Figure 5-10 show that the slope of the GZ curves is increased for increased angles up to about 20° and for wave heights up to about 4 m. In Figure 5-12 it can also be seen that the mean value of GM is increased with the wave height i.e. both increased wave height in upright condition and increased roll angle leads to increased stiffness and thus the natural roll frequency of the ship. At low wave heights the mean GM has a low rate of change and is close to the static value and occurrence of parametric roll will be close to $\omega_e/\omega_{eg}=2$. Even though all dynamic effects of ship motions are excluded in the calculations behind these figures, these qualities are believed to be the dominant causes to the behavior in a) and b).

Observation d) can be explained by inspection of Figure 5-11 where the span of GM has a maximum value below λ/Lpp=1 at about 0.85. However for the head seas cases it seems that the encounter frequency is governing for the parametric roll excitation i.e. wave lengths with maximum GM span will render a too high frequency of encounter for parametric roll to be excited, see Figure 5-9. The opposite seems to hold for the Fn=0.08 following seas case. Here the maximum GM span will render a too low frequency of encounter.

The decay and disappearance of parametric roll as the wave height increase as observed in the present study, e), have also been observed in experimental results, e.g. Spanos and Papanikolaou (2009a). From Figure 5-12 it can be seen that for a given wave length the mean GM and thus the natural frequency of roll will increase with increased wave height. By this the parametric roll will be "detuned" and the roll angle decrease as the wave height is increased. A similar explanation is also discussed in Spanos and Papanikolaou (2009b) and Neves et al. (2009).

The model test results of test case T2 and T3, T4 and T5 and T13 and T14, Figure 5-7, show decreasing roll amplitude with increasing wave height. The same trend can be seen in the simulation results at corresponding frequencies. The simulations of T3 and T14 are however outside the simulated regions of occurrence and show no parametric roll, Figure 5-7 and Figure 5-8. Test case T15 has the largest discrepancy of all the cases of the validation study with a 30° steady state roll angle in the simulations and no parametric roll in the model test. Inspection of Figure 5-8 reveals that T15 is very close to the steep boundary of occurrence, predicted by simulations, and that with only a slight increase of encounter frequency or a reduction of wave height by about 0.5 m would result in a change of a very severe parametric roll to no parametric roll at all.

5.3 Collision survivability in waves

Introduction

One of the largest causes of severe ship flooding is collision with another ship resulting in a breach in the water tight integrity of one or both ships. Large research efforts are being made toward understanding the mechanisms involved and prevention and mitigation of the consequences of collision events through simulation. The problem is however complex and involves different research disciplines and have to a large extent been treated in separated parts, reflecting the different disciplines, with very limited interaction. In Schreuder et al. (2012) an investigation of the chain of events of ship collision, flooding and time to capsize, following an interdisciplinary calculation procedure, was presented. In a case study calculations were made to study the influence of various parameters, e.g. wave climate and impact speed, in a collision event between a RoPax ferry and a ship of similar size. Below follows a summary of the calculation procedure and a description of the study pertinent to present thesis.

The calculation procedure concerns the interaction between two tracks: structure and stability. Figure 5-13 show the interaction scheme between the two tracks where the information from a collision scenario calculated by the structure track is transferred to SIMCAP for further analysis of the behaviour of the damaged ship. The feedback loop outlined in the figure, where the loads in the structure track model are updated through the SIMCAP simulation for further analyses of possible damage propagation, was not explored by actual calculations.

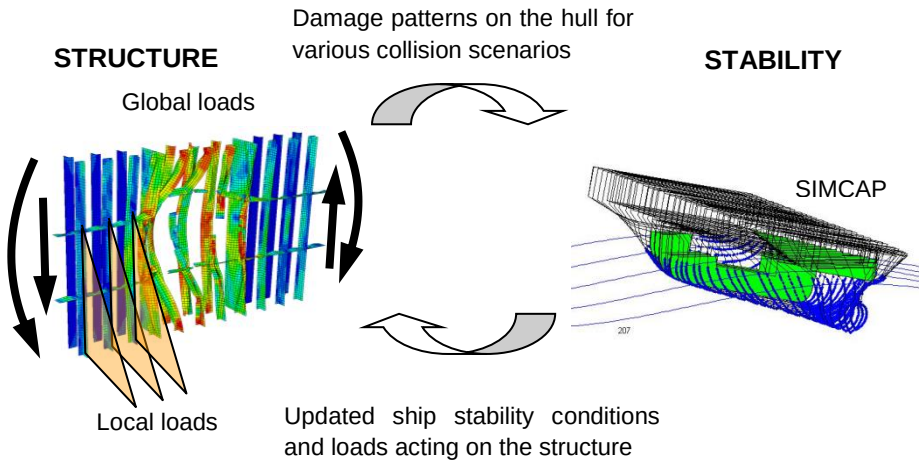

Figure 5-13 Iteration scheme between structure and stability tracks. The structure track delivers the damage pattern caused by the collision to the stability track, which calculates the ship's behaviour in the damage situation. There is also a possibility to update the load condition in the structure model and thus create a feedback loop between the two tracks (Schreuder et al. 2012).

In the structure track explicit nonlinear finite element (FE) method simulations are used together with phenomenological models, which can mimic the collapse and rupture phenomena in ship-to-ship collision, with satisfying reliability. An elasto-plastic material model was combined with a failure model, which eventually brings the material in the FE

model to fracture through erosion. The FE analyses were restricted to the internal mechanics during the collision. The struck ship model was held fixed as the striking ship was given an initial kinetic energy which was gradually lost during the collision event as energy is dissipated through friction, plastic deformation and as fracture develops in the hull structure. The striking ship was assumed to be rigid, see Hogström (2012) for further details of the FE model simulations. The assumption of the struck ship held fixed is conservative.

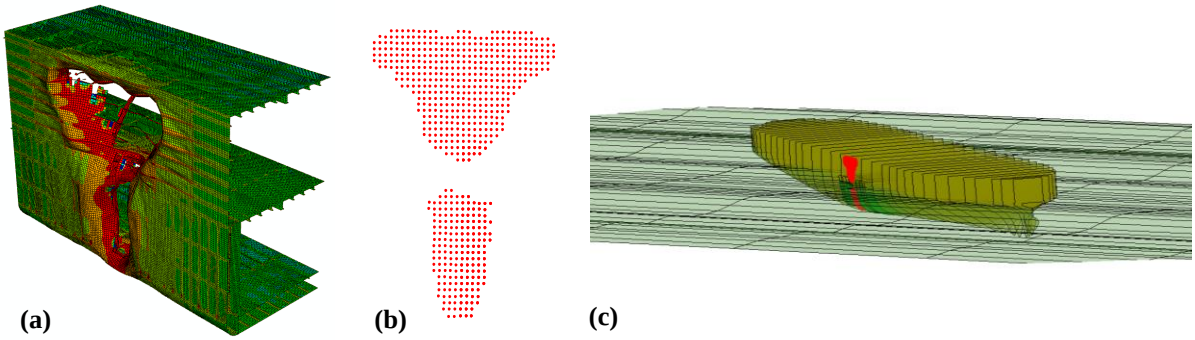

Figure 5-14 **(a)** Structural damage and damage opening from FE analysis; **(b)** illustration of representation of damage opening by grid (area) points used for flooding calculations; **(c)** illustration of damaged ship in a seaway (Schreuder et al. 2012).

After a collision event have been simulated by the structure track the information about the resulting damage opening is transferred to the stability track trough projection of the opening onto the un-deformed side shell of the struck ship where it is defined as a set of points each associated with an opening area, see section (damage opening definition). An illustration of a damage opening in the structure and stability track is shown in Figure 5-14. A convergence study was made in order to determine the minimum resolution that is needed for a proper representation of the damage openings in SIMCAP.

Convergence Study

In the convergence study a one-compartment asymmetric damage case of RoPax ferry was simulated in calm water and with a few additional simulations in waves. Figure 5-15 show the ship in the equilibrium floating position of the damage case. The study was carried out considering five different resolutions in conjunction with the influence of the resolution on the size and vertical position of the damage opening. The damage case configurations used in the study are presented in Table 5-4. All damage openings were geometrically similar, with the exception of the lowest one point resolution, and were generated by an FE simulation with a half-sphere indenter representing a bulbous bow penetration of the struck ship. Figure 5-16 shows the sizes and positions of the SIMCAP representation of the damage openings. At the start of each simulation the ship was floating at the intact equilibrium when the damage opening suddenly appeared.

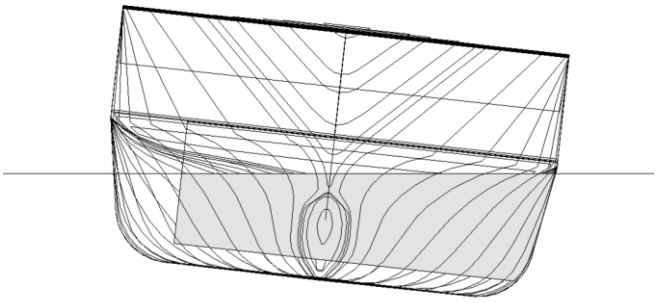

Figure 5-15 Ship at final static equilibrium (Schreuder et al. 2012).

Table 5-4 Damage opening parameters.

Resolution		
#1	1	point
#2	157	points
#3	571	points
(#4	2189	points)
(#5	8572	points)
Size		
L (1:1)	39.25	m^2
M (1:2)	9.81	m^2
S (1:4)	2.45	m^2
Position (centre of opening from keel line, KL)		
Upper (a)	6	m
Middle (b)	5	m
Lower (c)	3	m

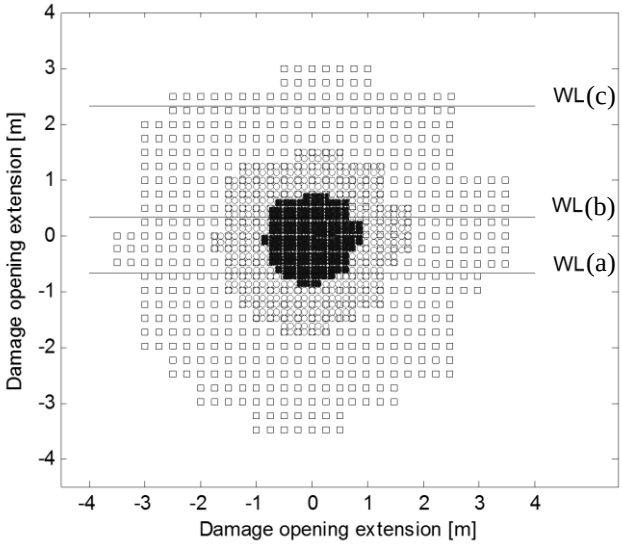

Figure 5-16 Damage opening size (resolution #3) and vertical positions (WL = water line) (Schreuder et al. 2012).

Figure 5-17 shows the time series of the original 27 simulations in calm water. The simulations consist of a variation of three resolutions (#1-3), three sizes and three vertical positions according to Table 5-4. The level of convergence was estimated by inspection of the difference between the different resolutions of the time series of the roll motion and the flooded water. For eight of the nine variations of size and position there is an almost ideal agreement between the different resolutions; in fact, the curves are almost completely overlapping and the difference cannot be seen in Figure 5-17.

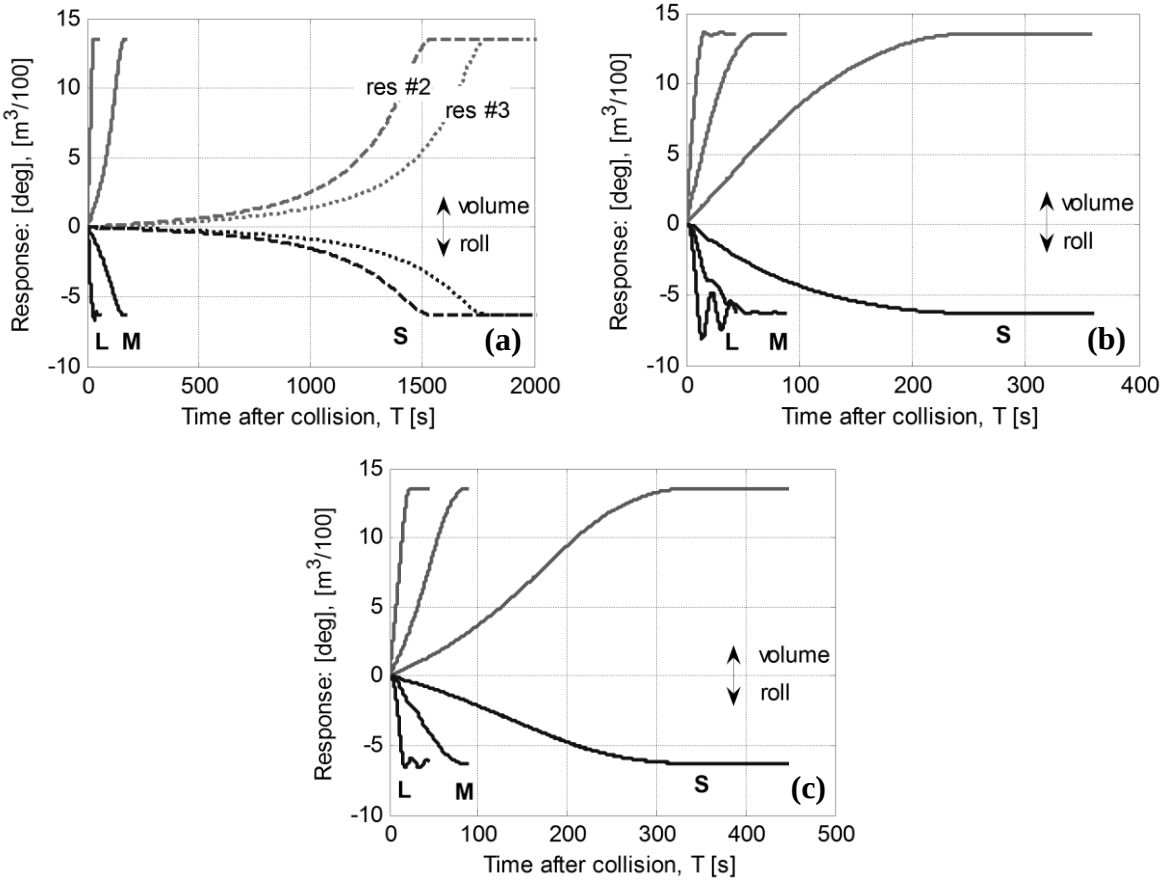

Figure 5-17 Time series of the original 27 simulations in the convergence study for the three different positions: **(a)** upper, **(b)** middle and **(c)** lower. Shown are the ship roll response (lower curves) and flooded volume (upper curves). Three sizes of the damage opening: small (S), medium (M) and large (L), as well as three different resolutions, #1, #2 and #3, see Table 5-4. Note that results from different resolutions in **(b)** and **(c)** overlap (Schreuder et al. 2012).

The exception is for the case with the smallest damage opening in the uppermost position where the time series of resolution #2 and #3 are clearly separated, Figure 5-17 (a). This resolution dependence is believed to be threefold; 1) there is a relatively low resolution of the initially submerged part of the opening, 2) since the opening is close to the water surface there is a relatively large discrepancy of the pressure heights of the different resolutions, 3) there is a direct feedback loop in which an error will propagate and thus enhance the resolution dependence i.e. the amount of floodwater determine the floating position which determine the submerged opening size which determine the flood rate.

Simulation in waves for the same damage case configuration, however, shows a reasonable convergence, as can be seen in Figure 5-18. Additional refinement in resolution (#4 and #5) as well as lowering the damage opening in small increments also shows converging results. Also the progressive flooding in section 4.2, with flooding over doorsteps and through broken pipes, share the features of the present case with the exception of the feedback loop described above, and shows practically no sensitivity to resolution. Thus it is believed that this case is rather exceptional and of little practical importance.

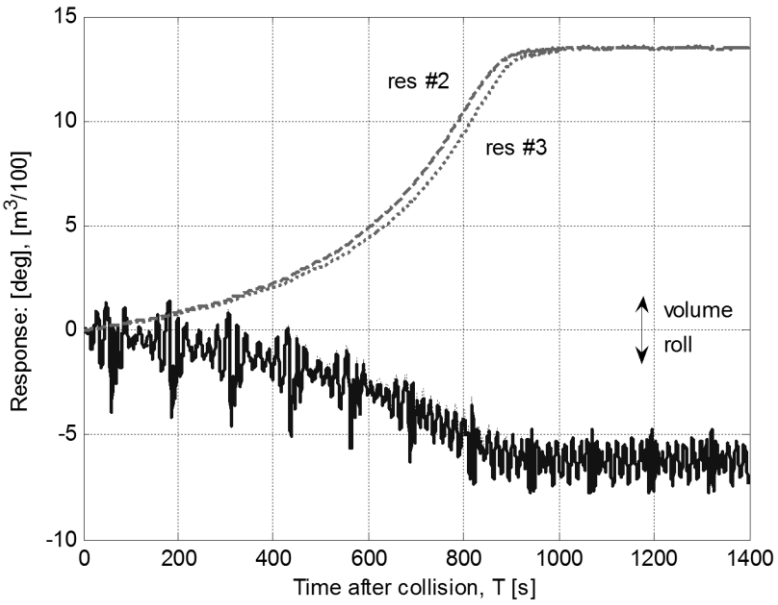

Figure 5-18 Response and water flow for simulation in waves with small damage opening in upper position (Schreuder et al. 2012).

Description of a case study

The case study comprises the chain of events from ship-to-ship collision to ship capsize due to flooding in waves. The main focus was to investigate the influence of various parameters on the time span from the collision to ship capsize, T_{cap}.

In the study a RoPax ferry was struck around amidships and at a 90° angle of attack by a striking ship of similar size. A damage opening resulting from a collision at an initial speed of six knots of the striking ship can be seen in Figure 5-14.

Table 5-5 Main particulars of the RoPax ferry (Schreuder et al. 2012).

Particulars		
Length over all, L_{OA}	179	m
Length between perpendiculars, L_{pp}	170	m
Breadth, B	27.8	m
Draught, T	6.25	m
Depth, $D_{cardeck}$	9.00	m
Displacement, Δ	17300	metric tonnes
Center of gravity, KG_{intact}	12.89	m
Metacentric height, GM_{intact}	2.63	m

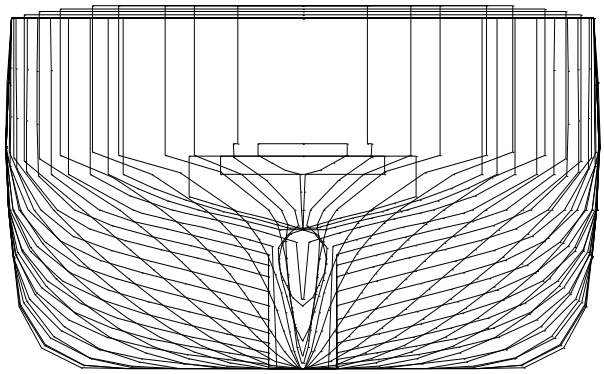

Figure 5-19 Hull lines of the RoPax ferry (Schreuder et al. 2012).

The main particulars and hull lines of the struck ship is presented in Table 5-5 and Figure 5-19. Two damage cases were used in the study, which corresponded to SOLAS one- and two compartment damages (IMO 1997). In the one-compartment damage the vehicle deck and a void space (void) below the vehicle deck could be flooded. Floodable spaces in the two-compartment damages also included a machinery space (mach), aft of the void space, and the starboard heel tank (SB htk), see Figure 5-20. The one-compartment case is symmetric and the two-compartment case is asymmetric, with a list angle of three degrees at static equilibrium. Furthermore, SIMCAP was validated for the two-compartment case regarding hydrostatic properties and response amplitude operators for intact and damaged ship in Schreuder (2005), following the benchmark study in ITTC (2002), see Figure 5-21. The damage opening in Figure 5-14 was used to create both the one- and the two-compartment damage case.

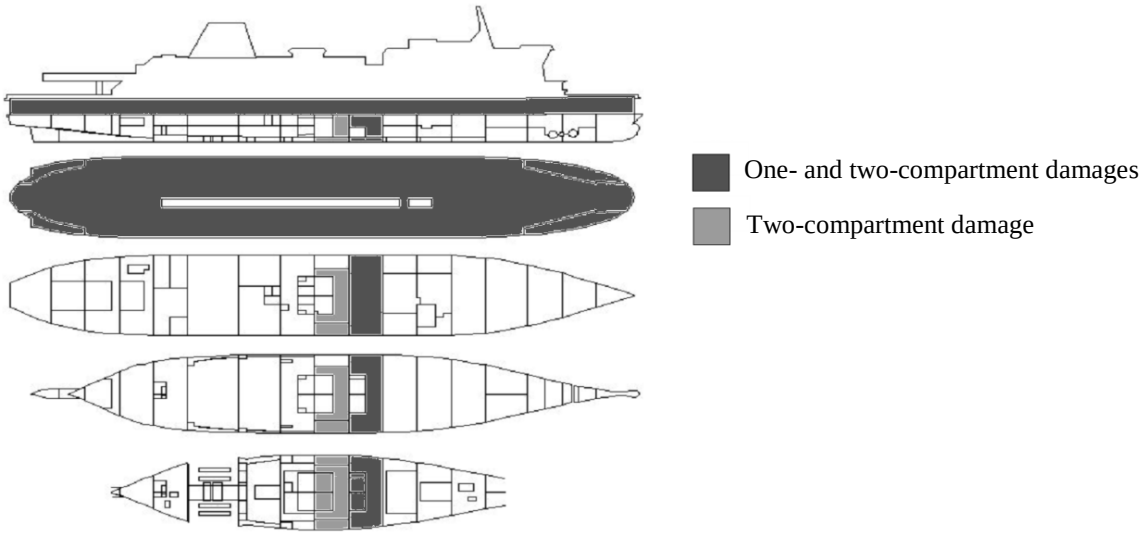

Figure 5-20 The RoPax-ferry with the damaged compartments shaded (Schreuder et al. 2012).

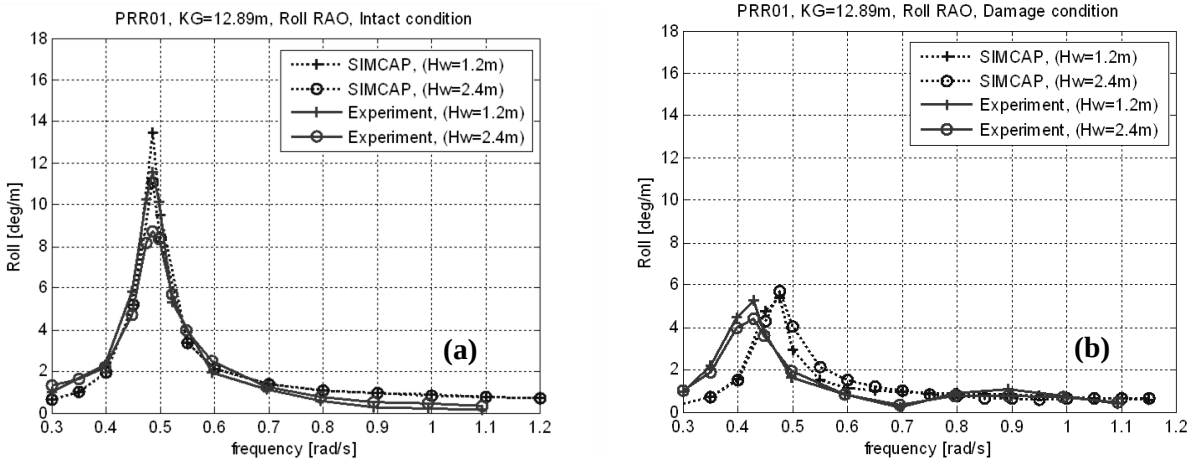

Figure 5-21 Experimental and numerical roll response amplitude operator (RAO) of the RoPax-ferry for two wave heights (Hw), see Schreuder (2005): **(a)** RAO for intact ship, and **(b)** the two-compartment damage.

Table 5-6 show the parameters for which the influence on T_{cap} was studied. For each case where the parameters had been fixed, called damage case configuration, eight simulations with a random phase shift between the components of the wave spectrum was made in order to account for the natural variation in the sea state. In order to investigate if eight wave seeds are sufficient to represent the impact of a random sea state on T_{cap} a sensitivity study, where 50 additional wave seeds were simulated for one of the damage case configurations, were made and is presented below.

Table 5-6 Parameters in the case study.

Parameter	Quantity	Value
Wave spectrum	2	Jonswap/P-M
Wave height	11	3-8 m
KG	3	12.89±1 m
Heading	16	0°-360°
Damage	2	1-2 compartment

In calm water or moderate sea states, the two-compartment damage is not critical from a stability point of view. In more severe sea states however, waves will reach the damage created by the upper bow of the striking ship and accumulation of floodwater on the car deck is possible, which will finally result in capsize of the ship. The capsize mode of the two damage cases is furthermore of quasi-static character, i.e. ship capsize is essentially determined by the amount of water on the car deck. This mode of capsize has been recognised in model test e.g. Tagg & Tuzcu (2003) and is typical for ships with large open vehicle decks.

Figure 5-22 shows the time series of roll motion and flooded volume on the car deck of a simulation resulting in capsize. The appearances of the time series are typical in the sense that that there is a fairly slow list development and accumulation of floodwater followed by a very rapid capsize and flooding, after about 330 second in this case. This transitional behaviour is due to the quasi-static nature of the event; the rapid capsize occur close to when the amount of floodwater on the car deck is the same as when the stability is lost in a static calculation on corresponding damage case. The rapid capsize process can partly be explained by the absence of superstructure, and hence temporarily buoyant spaces, in the numerical ship model. However, an essentially non-watertight superstructure cannot prevent capsize; it can only slow down the process toward an inevitable event (Schreuder 2008).

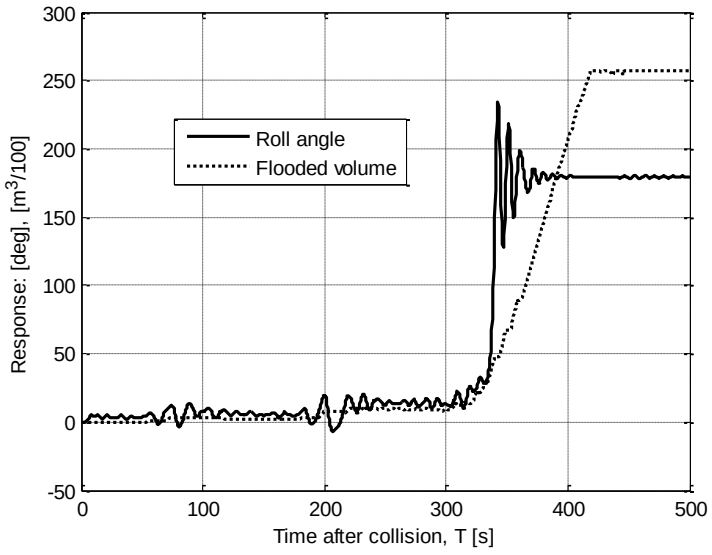

Figure 5-22 Time series of typical capsize simulation (Schreuder et al. 2012).

Assumptions in the simulations

It was assumed that there was no flooding during the FE simulations of the collision event and that there was no water in the floodable spaces at the start of the SIMCAP simulations. It was further assumed that the striking ship did not obstruct the damage opening. T_{cap} was defined as when the floodwater volume on the car deck reached 2000 m^3. The list of the ship was then about 25°. Beyond this angle a possible evacuation procedure would be very difficult and the absence of superstructure also makes the simulations unrealistic. The ship did always reach a roll angle of 180° within a few wave encounters after T_{cap} and this is also a robust definition since the floodwater volume increased monotonically before 2000 m^3 was reached as opposed to e.g. the fluctuating roll angle. A dead ship condition without forward speed was assumed. The simulations were made with an earlier version of SIMCAP, where the memory effect had not yet been implemented, and the hydrodynamic coefficients were constants in each simulation and were evaluated at the peak period (T_p) of the wave energy spectrum. The wave spectra were represented by discrete components of a constant width; $\Delta\omega$=0.05 radians/s. The roll damping was linear and tuned as to match corresponding intact roll decay model test in ITTC (2002).

Capsize probability

A set of simulations were conducted for the two-compartment damage with a loading condition corresponding to KG=12.89 m, in order to investigate the influence of wave direction and wave height on T_{cap}. The sea states of the tests had a span of significant wave heights (H_s) between three and eight meters with an increment of 0.5 m and were represented by a Jonswap spectrum with $T_p = 4 \cdot \sqrt{H_s}$, (H_s/λ =0.04), and γ=3.3 and a Pierson-Moskowitz (P-M) spectrum with T_p =12 s. Eight different headings were used, one every 45°. For the Jonswap spectrum an additional eight headings were simulated, one every 22.5° in total.

It was noted that the compartments below the vehicle deck were flooded rather rapidly after the start of the simulations; they were flooded to the mean outside water level after about three minutes. The flood rates were essentially invariant to the wave height an example of which can be seen in Figure 5-23.

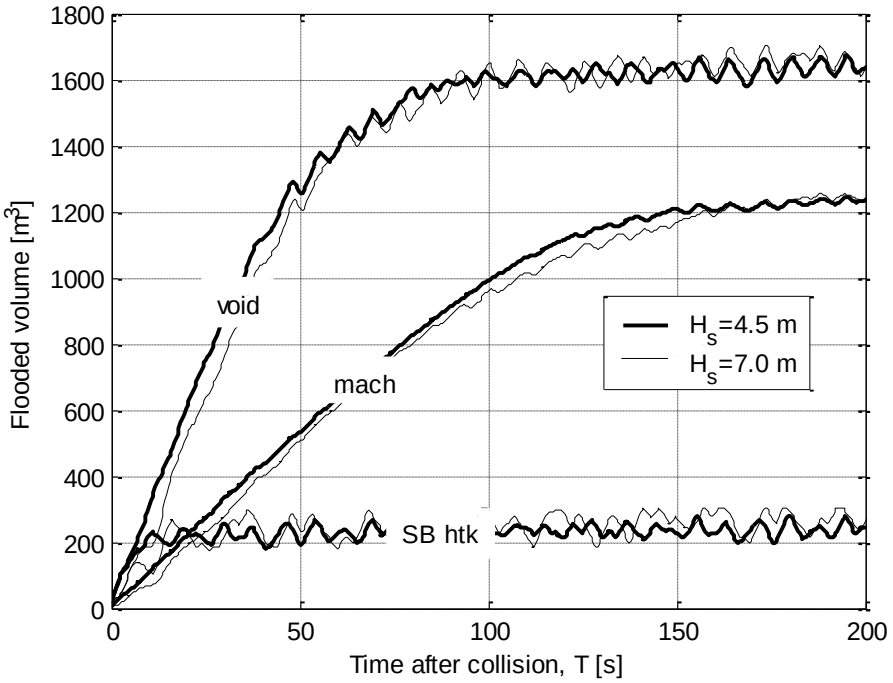

Figure 5-23 The flood rate of the spaces below the vehicle deck is independent of wave height (Schreuder et al. 2012).

The time to capsize was collected from each simulation and in Figure 5-24 T_{cap} for each of the eight wave seeds is plotted against H_s in following seas for the Jonswap spectrum, to provide an example. Note that the simulations were stopped at 30 minutes of simulated time and that the results here are indefinite; the ship could be close to capsize or "survive" for infinite time.

If the significant wave height is sufficiently small there will be a balance between in- and outflow of water on the vehicle deck and if H_s is further decreased there will be a low probability that any individual wave will be able to reach the vehicle deck, due to the residual freeboard of the damage case. This, together with the appearance of the curves of Figure 5-24 suggests the existence of a limiting wave height below which capsize only occur with a very low probability; see also, for example, Spanos and Papanikolaou (2007).

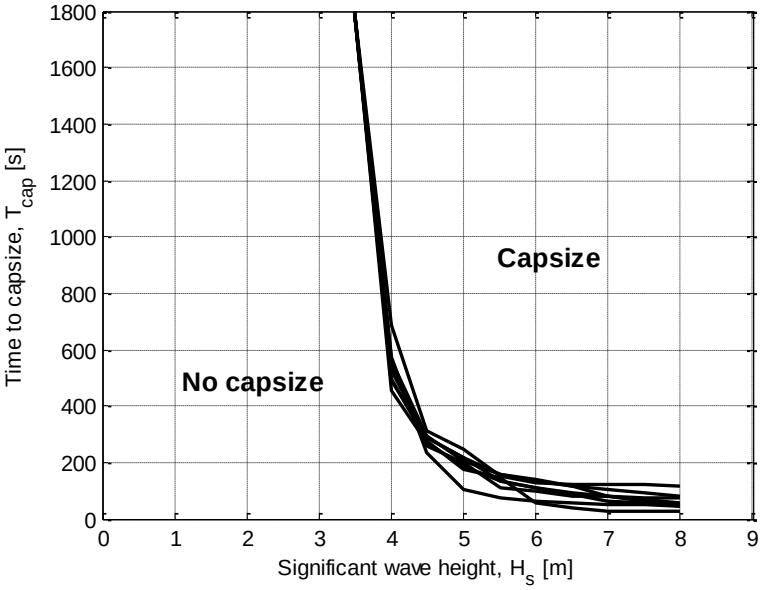

Figure 5-24 Capsize band from 8 wave seeds of following seas simulation with Jonswap spectrum (Schreuder et al. 2012).

The area enclosed by the wave seed traces in Figure 5-24 can be denoted "capsize band" (Jasionowski et al. 2003); i.e., the probability of capsize within this area increases with wave height and time and fore a finite number of simulations will change from 0 to 1 as indicated in Figure 5-24. This is also exemplified in Figure 5-25 where cumulative density functions of capsize probability are plotted for three different wave heights. The plots in Figure 5-25 include 50 wave seeds in addition to the eight seeds in Figure 5-24.

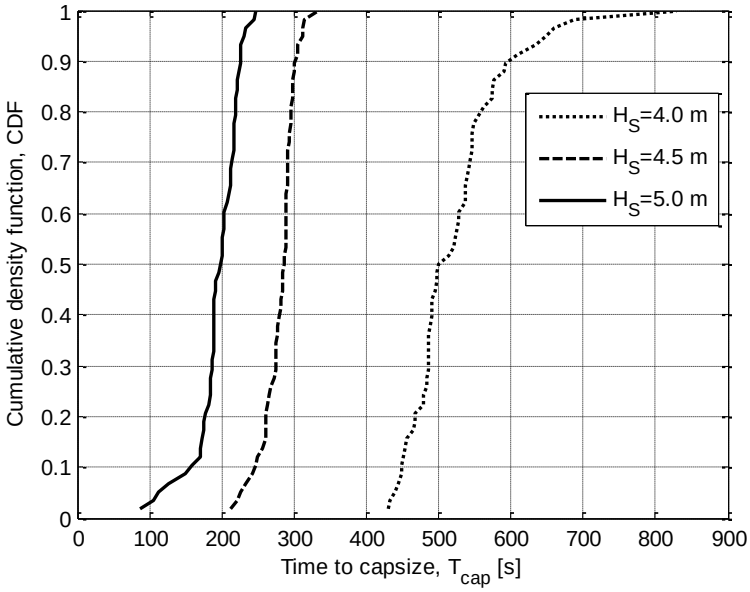

Figure 5-25 Cumulative density functions of capsize probability versus T_{cap} for H_s = 4.0 m, 4.5 m and 5.0 m (Schreuder et al. 2012).

In Hogström and Ringsberg (2012) SIMCAP was utilized in an extended investigation of the two compartment damage case in beam seas. Here, an extensive parameter study where the impact of uncertainties of input parameters of the FE collision analysis on the shape and size of the damage opening and further on the time to capsize of the struck ship was investigated.

To provide an example from the investigation, Figure 5-26 shows the damage openings for one set of simulations where the initial speed of the striking vessel, the angle of impact between the vessels and the steel to steel friction coefficient has been varied. Figure 5-27 show the capsize bands resulting from SIMCAP simulations for each of these damage openings. Three additional simulation sets where other parameters of the FE collision analysis were investigated in the same manner and the analysis of the results concluded in modelling recommendations for ship-to-ship FE collision analysis.

A general observation of the simulations is that a larger damage opening will lead to shorter time to capsize, as expected. However, a closer inspection reveals that the shape and extension of the upper part of the damage opening, leading into the vehicle deck, seem to have a significantly larger influence on T_{cap} compared to the lower part. The influences from the upper and lower parts of the opening are intrinsically connected but the lower compartments are generally flooded to the mean free surface in a relatively short time, see Figure 5-23, compared to T_{cap} and thus the lower part of the damages cannot to any significant extent explain the differences in the capsize bands of Figure 5-27. Comparing e.g. the first and fourth column of row two in Figure 5-26 and Figure 5-27 it can be seen that the first case has a significantly higher vulnerability to capsize, the capsize band is lower and e.g. the smallest T_{cap} of H_s=4 m is less than half compared to the second case. This is explained by the larger upper damage opening of the first case (in fact the total damage area is slightly larger for the second damage case). This case is supported by model tests, ITTC (2000), where it was found that a rectangular damage opening would allow the vessel to survive at higher significant wave heights than an opening with tapered sides and maximum width at the top.

A clear trend of large scatter in T_{cap} for the cases where the upper part of the damage was completely above and had a distinct clearance to the vehicle deck, could be recognized from the simulations. This is exemplified in the case of row three and column two in Figure 5-26 and Figure 5-27. It was not evident however that these cases generally had a lower capsize vulnerability; a high damage will be more rarely subjected to flooding in a seaway but the water that do flood will also be trapped on the vehicle deck, until a relatively late stage where outflow might be possible.

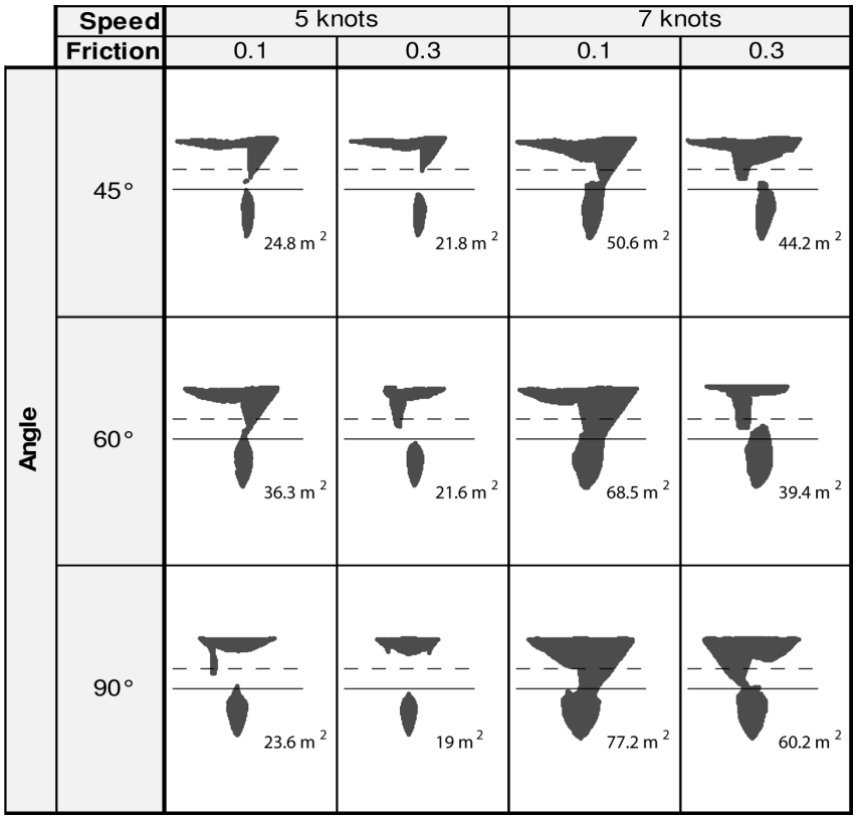

Figure 5-26 The shape of each damage opening presented along with its total area. The still waterline of the vessel is indicated with a solid line and the vehicle deck with a dashed line (Hogström and Ringsberg 2012).

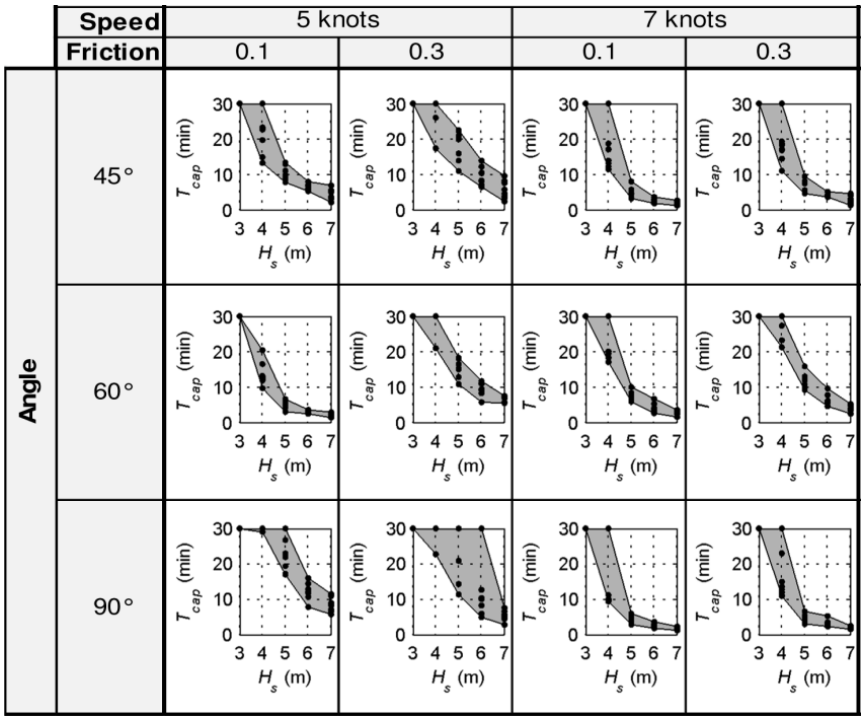

Figure 5-27 Results from SIMCAP simulations. The time to capsize is indicated for each significant wave height and for each wave seed (Hogström and Ringsberg 2012).

Influence from heading angle and significant wave height on Tcap

In Figure 5-28 the aggregate results of all simulations in the first simulation set are presented as two polar plots, for the Jonswap and P-M spectra respectively. The angle in the plots represents ship heading, the color scale represents significant wave height and the radius represents mean value of T_{cap}, including any indefinite value of 1800 s.

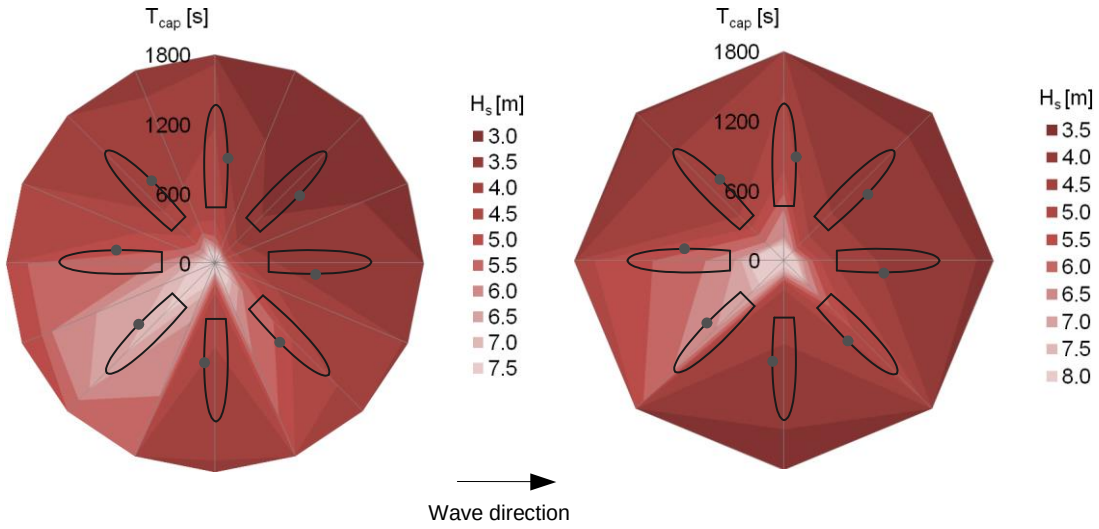

Figure 5-28 Polar plots of the results from the Jonswap (left) and P-M (right) simulations. The color scale corresponds to H_s and mean value of T_{cap} is on the radial axis. Wave direction is from left to right and the damage opening is indicated by a dot (Schreuder et al. 2012).

The ship and the starboard side damage opening is indicated in the plots and the result show that for beam seas onto the damage and quartering seas on the opposite side to the damage, the ship has the highest vulnerability to capsize. For waves on the bow onto the damage the ship is least vulnerable to capsize. This holds for both Jonswap and P-M spectra. All capsizes in this simulation set occurred toward the damage, the side with the lowest rightening lever.

Influence from KG on T_{cap}

The next simulation set consisted of simulations of the one-compartment damage in beam seas onto the waves with a Jonswap spectrum and for three different loading conditions (KG/GM values). Figure 5-29 shows the lower capsize band envelope for GM values of 1.63, 2.63 and 3.63 m, respectively. The vulnerability to capsize is significantly reduced as GM is increasing.

The damage case of this simulation set is symmetric and it is not evident that capsize would occur towards the damaged side, here also toward the waves. However, for only one out of 115 capsize simulations, the capsize occurred toward the opposite side. This can be explained as follows: If the ship is heeled away from the damage the freeboard at the damage will be increased and the flooding process will be slowed down or cancelled altogether. In connection to this, in early stages of flooding of the car deck the waves will easily shift the ship through the starboard and port equilibrium; the static GM is always negative with water on deck. As the amount of floodwater increases, more energy is needed to shift the ship between the

equilibriums. The ship could now get stuck, at a heel away from the damage, either permanently and "survive" or until a group of waves are able flood the ship further and capsize will occur opposite to the damage or until a group of waves are able to shift the ship back. An example of the latter is depicted in Figure 5-30 where T_{cap} was actually increased, compared to a lower wave height with the same wave seed, due to that the ship got stuck for about two minutes with no inflow of water on the car deck.

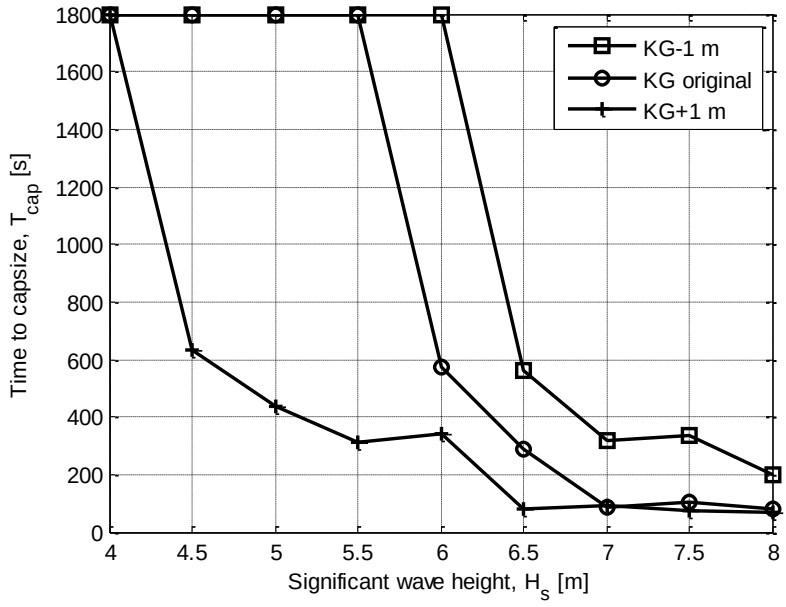

Figure 5-29 Lower capsize band envelop of capsize bands for different values of KG (Schreuder et al. 2012).

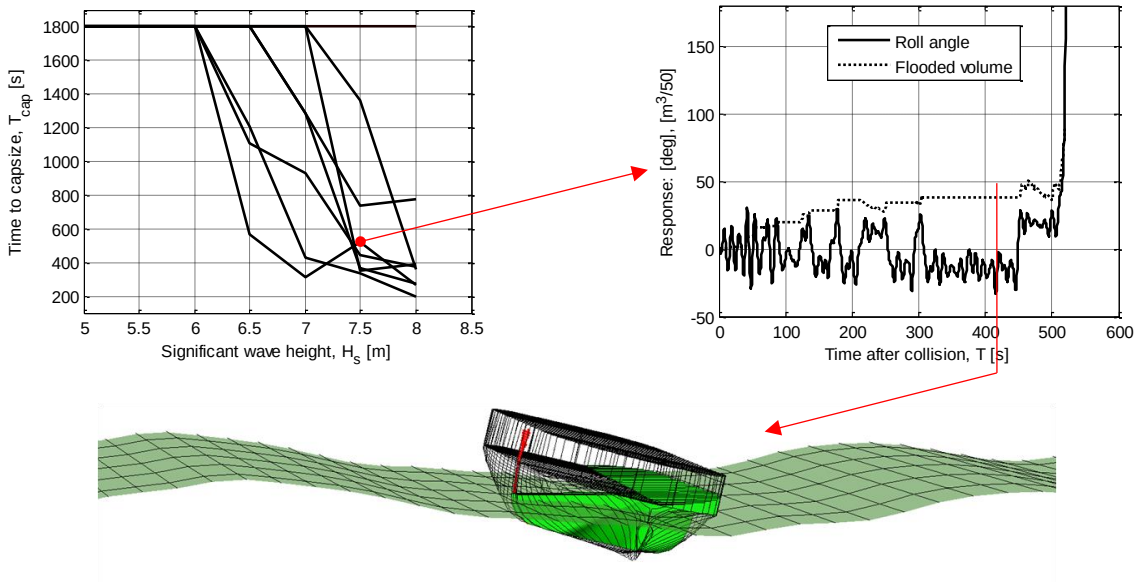

Figure 5-30 The left graph shows the capsize band of a damage case configuration. The red dot denotes a simulation which time series is shown in the right graph. Here, the ship got stuck with a list away from the damage for about two minutes (the below picture is a snap shot from simulation at time = 418 s) and T_{cap} is increased accordingly (Schreuder et al. 2012).

Sensitivity analysis

In the case study eight different wave seeds were simulated, in order to capture the impact of the randomness of the sea on the time to capsize, for each damage case configuration. The mean value of T_{cap} of these simulations was used as the expected time to capsize in the aggregate results of the study, Figure 5-28. The results presented in Figure 5-24, however, shows that the eight wave seeds result in a significant variation in the time to capsize. The question then arise weather eight simulations is enough to estimate the expected value of T_{cap} for a specific damage case configuration or if more wave seeds needs to be simulated. In an effort to answer this question a set of simulations with 50 random wave seeds, in addition to the eight seeds, for four of the wave heights as presented in Table 5-7. The result of these simulations, together with the original simulations in Figure 5-24, is shown in Figure 5-31.

Table 5-7 Parameters in the sensitivity study.

Parameter	Quantity	Value
Wave spectrum	1	Jonswap
Wave height	4	3,5-5.0 m
Spectrum seed	50	Random
KG	1	12.89 m
Heading	1	Following seas
Damage	1	2-compartment

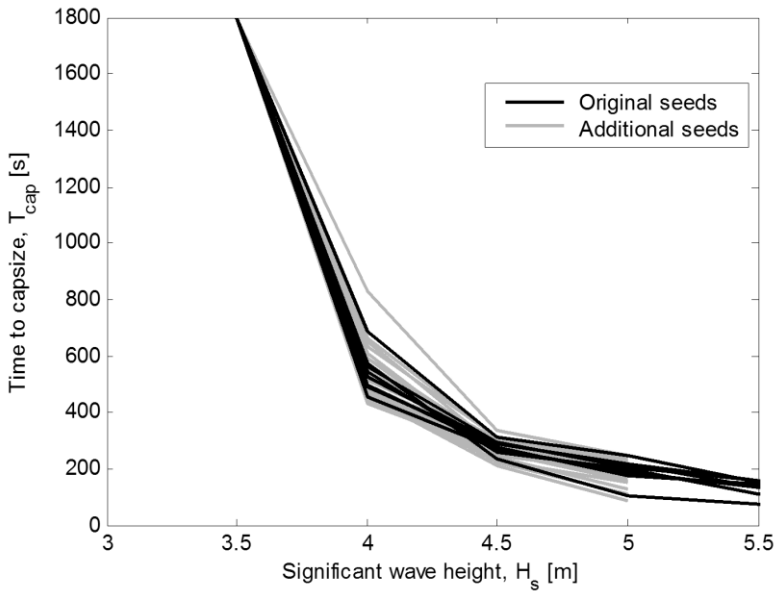

Figure 5-31 Time to capsize, T_{cap}, versus significant wave height, H_s. Illustration of the variation in T_{cap} due to different wave seeds for one collision scenario (Schreuder et al. 2012).

The result was analysed by plotting the evolution of mean and standard deviation of T_{cap}, for the wave heights 4.0, 4.5, 5.0 m, as the number of wave seeds is increased, as shown in Figure

5-32. The left column shows the "original simulation order" where the simulations, *s*, were ranked as $s = \{s_1; s_2; s_3; \ldots ; s_{58}\}$; this is denoted as "1 permutation" in the figure.

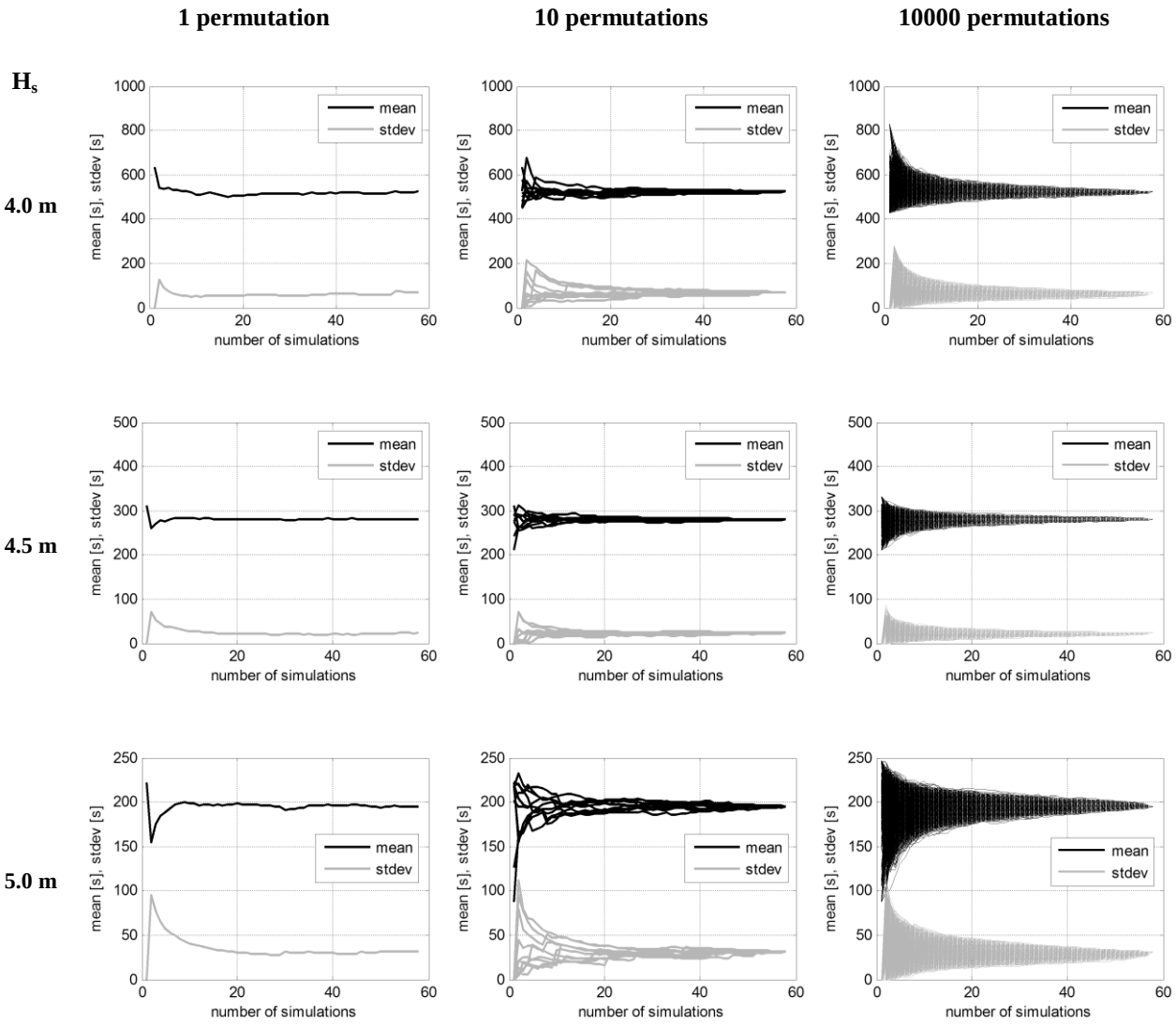

Figure 5-32 Evolution of mean value (mean) and standard deviation (stdev) of T_{cap} as the number of simulations increases. Original simulation order (left). Ten random permutations (middle). 10^4 random permutations (right), (Schreuder et al. 2012).

The simulations, *s*, are however independent and the order in which they appear in a simulation sequence affects the mean value and standard deviation of T_{cap}, when the number of simulations is smaller than 58. Thus, random permutations of *s* was made and plotted in the same manner as the original simulation order. The middle column of Figure 5-32 shows the trend after ten permutations and the right column after ten thousand permutations, which was deemed sufficient for the analysis (as the average of the mean value and standard deviation of the permutations, evaluated at eight simulations, had converged).

Now, assuming the mean and standard deviation for the 58 simulations are accurate, the average of the mean and standard deviation, of the ten thousand permutations at eight simulations, was calculated and compared with corresponding values at 58 simulations. The comparison, expressed as an error, together with the standard deviation of the averages, can be found in Table 5-8. The results of the sensitivity analysis suggest that eight wave seeds may be too few to represent the influence of the natural variation in the sea states on the time to capsize in this scenario. In the model tests and simulations described in section 4.1, where time to capsize for a similar scenario is investigated, 20 wave seeds are used. This seems more appropriate considering the significantly reduced scatter in the right column of Figure 5-32.

Table 5-8 Statistical error using 8 seeds compared to using 58 seeds.

H_s = 4.0 m			
	error of average of mean values	<0.1%	(mean of 58 simulations: 523 s)
	standard deviation of mean values	23 s	(4%)
	error of average of standard deviations	7.8%	(standard deviation of 58 simulations: 71 s)
	standard deviation of standard deviations	28 s	(39%)
H_s = 4.5 m			
	error of average of mean values	<0.1%	(mean of 58 simulations: 280 s)
	standard deviation of mean values	8 s	(3%)
	error of average of standard deviations	5.1%	(standard deviation of 58 simulations: 23 s)
	standard deviation of standard deviations	7.2 s	(31%)
H_s = 5.0 m			
	error of average of mean values	<0.1%	(mean of 58 simulations: 195 s)
	standard deviation of mean values	10 s	(5%)
	error of average of standard deviations	7.2%	(standard deviation of 58 simulations: 32 s)
	standard deviation of standard deviations	11 s	(34%)

5.4 Accident investigation

Introduction

On the 28th of September 1994 the RoPax vessel MV Estonia foundered in the Baltic Sea on her voyage from Tallinn to Stockholm. The ship sank rapidly and disappeared from the radar screens of nearby ships at 01:50 hrs. There were 852 fatalities and 137 survivors and the accident is considered to be the worst disaster at sea in post-war Europe.

In 2005 the Swedish Governmental Agency for Innovation Systems, VINNOVA, announced a call for research studies on the sinking sequence of m/v ESTONIA. A consortium headed by SSPA Sweden AB was awarded one of the finally two projects. The other members of the consortium were Safety At Sea Ltd, Maritime Research Institute Netherlands and Chalmers University of Technology.

The focus herein is neither to describe the accident itself nor the methodology or results of the project but merely to summarize the use of the SIMCAP code within the project. A very brief background is however presented in order to put the simulation studies into a context. More information about the accident and on the SSPA project can be found in the final report, Källström et al. (2008) and in the final report of the original accident investigation JAIC (1997).

Background

The approach of the research project was to collect and review available evidence such as transcripts of testimonies from survivors, video recordings from diving operations at the site of the wreck, radio communication etc. With the aid of an International Panel of Experts (IPE) different loss hypothesis, conformant with the evidence, was suggested and tested through model experiments and simulations. In the evaluation of the loss hypothesis a scenario that was deemed most probable was established. This can be summarized by:

- MV Estonia was sailing at full speed in close to head waves of above four meters of significant wave height.
- The bow visor was torn off the ship due to wave impact and the bow ramp was forced open creating a breach in the water tight integrity.
- Flooding of the car deck through the bow ramp opening was initiated resulting in a starboard side list.
- The officer on the bridge is decreasing speed and initiating a port side turn.
- The heel is increasing and the Main Engines fail at some point during the turn.
- Substantial flooding of spaces below car deck at a heel around 40°.
- Superstructure starts to flood. Ship drifting at around beam seas.
- Ship capsizes and sinks.

An illustration of this scenario, based on snap shots from simulations, is found in Figure 5-33.

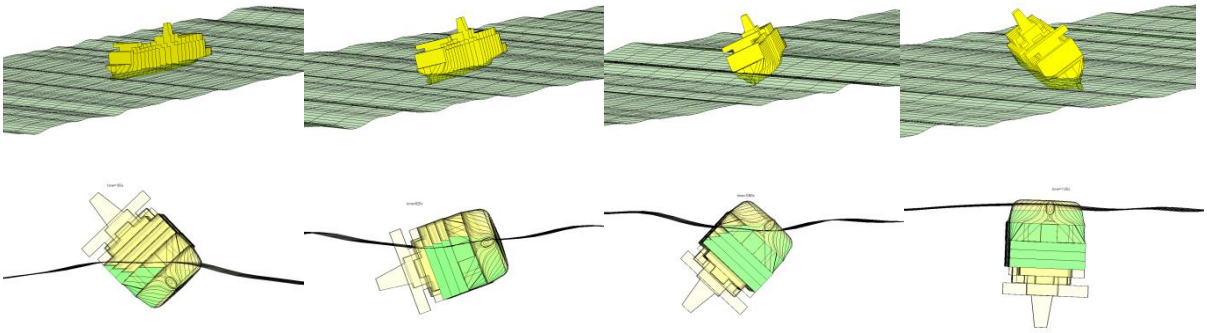

Figure 5-33 Illustration of sinking scenario with snap shots from simulations. The upper row of snap shots illustrates the initial stages of flooding through the bow ramp opening. The lower row illustrate the final stages of flooding, eventually resulting in capsize and sinking.

Two sets of SIMCAP simulations were made in order to substantiate the scenario and in an effort to reveal key physical mechanisms of flooding and capsizing. The first set of simulations concerned initial flooding through the bow ramp opening at different headings and speeds, upper part of Figure 5-33. SSPA also made model tests to establish the initial flood rates through the bow ramp opening. The second simulation set concerned later stages of flooding, with the ship at beam seas and zero forward speed, finally resulting in full capsize and sinking of the ship, lower part of Figure 5-33.

Numerical ship model

The initial loading condition of the intact ship was taken from the JAIC (1997) with a deduction for the weight of the bow visor. The hydrostatic particulars in intact condition are listed in Table 5-9. A general arrangement of the ship is shown in Figure 5-34. The two lower decks contain both machinery and accommodation spaces. The car deck and the center casing extend over two decks and the super structure includes five decks and the navigation bridge.

Table 5-9 Hydrostatic particulars of the intact condition.

Lpp	137.4 m
Beam	24.2 m
Displacement	11902.6 tonnes (w/o visor, 60t)
Draft (aft, mid, fwd)	5.65 m, 5.32 m, 4.98 m
List	1° SB
G'M	1.26 m
VCG	10.65 m
LCG	63.64 m fwd of AP

As the aim of the project was to assess the complete sinking sequence of the ship the super structure had to be modeled. The super structure of the ship is not water tight and cannot stop ship capsize or sinking. It will however slow down the process since some time is needed to

flood the large volume of the super structure. Figure 5-35 shows the traditional intact GZ curve together with a curve where the complete ship, from keel line to the top of the funnel, is assumed to be an intact buoyant volume. An intermediate curve, where the hull of the ship is represented up to deck 7, is also shown. This representation includes about 90% of the total gross volume of the ship and was used in the simulations. Thus, the uppermost decks and the funnel were assumed to be fully permeable and to flood instantly.

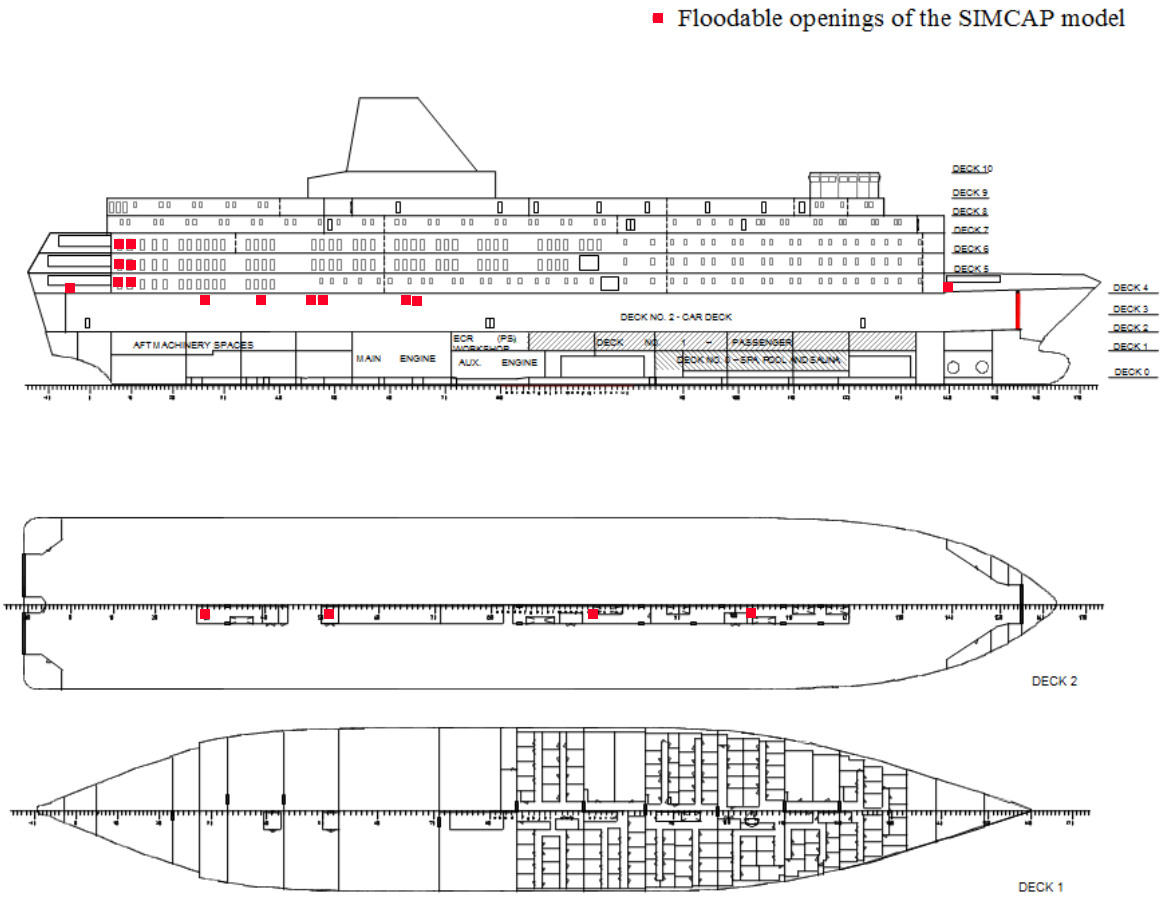

Figure 5-34 General arrangement and floodable openings of the SIMCAP model.

The decks of the super structure were modeled without internal subdivision as boxes and the car deck was modeled as one open space. These spaces had the permeability 0.95. The subdivision below the car deck was represented by seven spaces, where the actual spaces had been lumped together in larger groups. The permeability of these spaces was adjusted to obtain the total floodable volumes derived in hydrostatic calculations of a more complete model in terms of subdivision, content of tanks etc., Rutgersson et al. (2006).

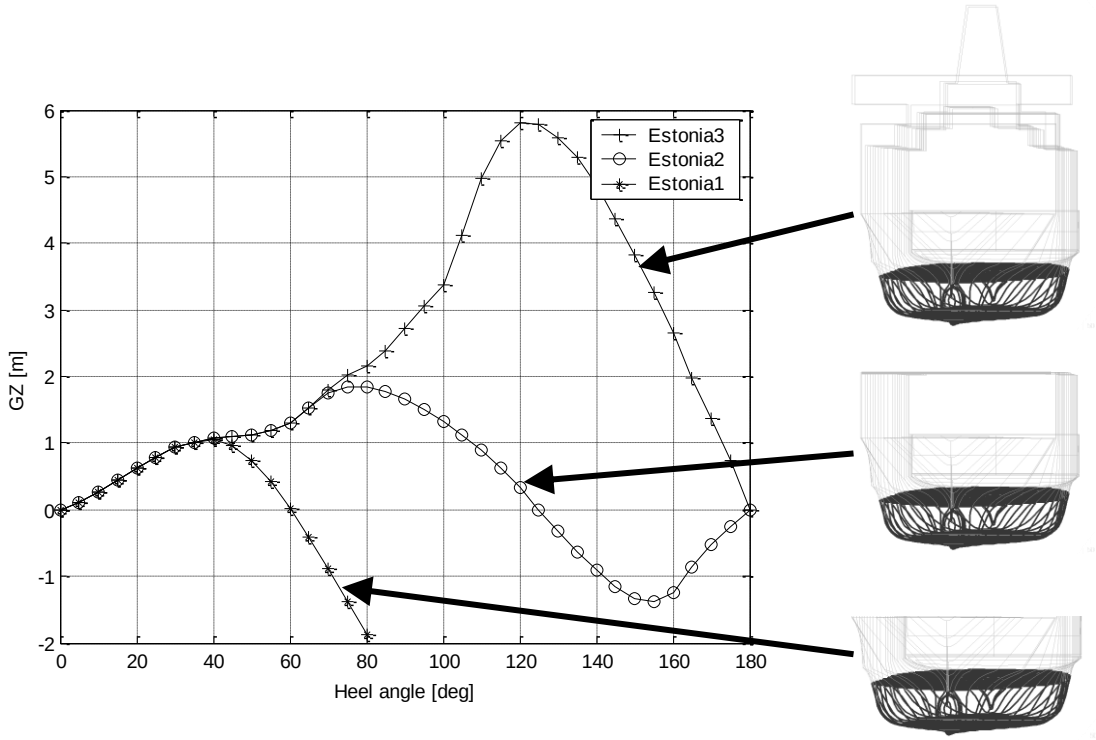

Figure 5-35 GZ curves of different representations of the ship, assumed to be fully buoyant. The lowest curve represents the GZ curve up to deck 4. The top curve include the complete ship up to the funnel top and the middle curve up to deck 7, which include about 90% of the total volume of the ship.

The floodable openings in the model were chosen with some care to obtain a representation as realistic as possible. There were many potential floodable openings that could affect the flooding process but a lack of information whether they were actually flooded or remained intact during the foundering. The openings finally represented in the numerical model were however believed to be the most important ones and appropriate for the modeled subdivision and for the purpose of the simulations.

The floodable openings are indicated in Figure 5-34. The decks of the superstructure were floodable through the two aft most windows on starboard side of each deck, which were assumed to be broken under the water pressure. All other windows were assumed to be intact due to counter acting pressure on the inside of the window as the spaces got flooded. The number of windows was chosen as to match the list development obtained from the analysis of the evidence; the list development at the late stages of flooding depends almost exclusively on the flood rates into the super structure. The car deck was floodable through the bow ramp opening and through supply and exhaust ventilators of the car deck situated forward and aft of the super structure on deck 4. The relatively small scuppers on deck 2 and some minor additional ventilation openings are omitted in the model. The machinery spaces could be flooded through starboard side ventilation ducts with openings located just below deck 4. They could also be flooded through the center casing through an elevator and a stairs opening. The accommodation spaces could be flooded through another set of elevator and stairs opening, see Figure 5-34.

The six ventilation duct openings leading to the machinery spaces have an opening area of 0.28 m^2 each. The four openings in the center casing have an opening area of 2 m^2 each. The opening through the bow ramp is 30.4 m^2. The openings through the car deck ventilators on deck 4 are 2.4 m^2 forward and aft respectively. The openings through the aft windows on the upper decks are 1.2 m^2 each. The bow ramp opening was represented by an evenly distributed grid of point openings (7 by 8 points). All other openings were represented by single points. A discharge coefficient, C_d, of 0.5 was used for all openings.

A roll decay model test, described in Allenström and Thorsson (2007), for the intact ship in zero forward speed was used to tune the linear roll damping coefficient of the SIMCAP model. Figure 5-36 show the time series of roll for the model test and simulation after tuning.

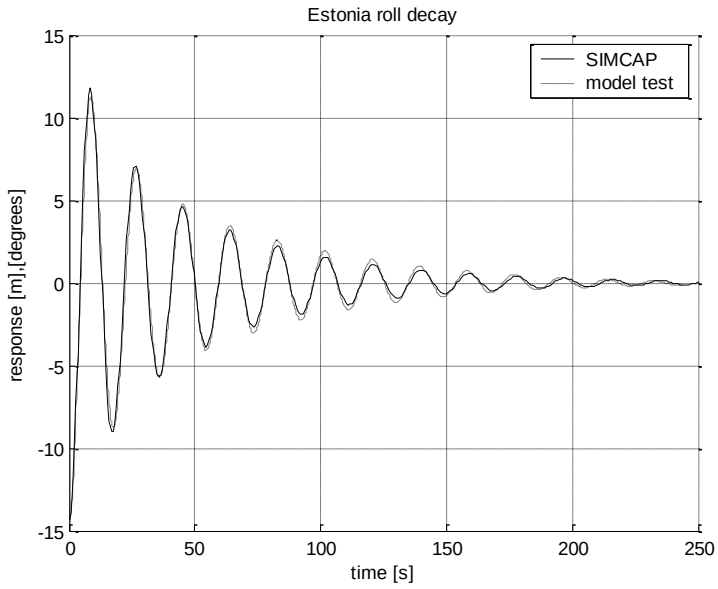

Figure 5-36 Roll decay model test and simulation.

The simulations were carried out in irregular long crested waves defined by a JONSWAP spectrum with the spectrum parameters: significant wave height, H_s=4.3 m, peak period, Tp=8.3 s and a peak enlargement factor, γ=3.3. The sea state was based on a hind cast for the location and time of the accident. The spectrum was represented by 22 evenly spaced wave components ranging from 0.45 rad/s to 1.50 rad/s. The simulations were made with an earlier version of SIMCAP, where the memory effect had not yet been implemented, and the hydrodynamic coefficients were constants in each simulation and were evaluated at the peak period (T_p) of the wave energy spectrum. The water density was set to 1.01 tonnes/m^3 in the simulations, which is the water density in the Baltic Sea.

Initial stage flooding simulations

A series of simulations were made to study the behavior of the ship assuming that the bow visor was detached and the bow ramp opened. In the simulations ship speed and heading was varied. The assumptions for these simulations were that the only way of flooding was through

the bow ramp opening and that the ship had a constant speed and heading in each run. The bow ramp was closed at the start of each simulation and fully opened after 20 seconds. The tested speeds were 5, 10 and 15 knots and the headings were head seas, 15°, 30° and 45° on starboard bow. In order to account for the effect of forward speed of the ship on the flooding, the ship speed was added to the flow velocity of the generic Bernoulli type flooding mechanism of SIMCAP.

The results from the simulations showed that a steady state mean roll angle of about 50° was reached as the volume of accumulated floodwater reached 5000 tonnes. For all simulations however, floodwater continued to accumulate on the car deck until a steady state for all motions was reached within the simulation time of 10 minutes. Figure 5-37 show the time series from one of the simulations which is qualitatively typical for all simulations. The additional floodwater volume, after some 50° of heel has been reached, only contributes to the heave of the ship. This is due to that the centroids of the ships water plane area and the surface of the floodwater are close to the same vertical line, from this time and on. In the end of the simulations, at steady state, the lower corner of the bow ramp opening is close to the mean wave elevation and water is flowing both in and out of the car deck.

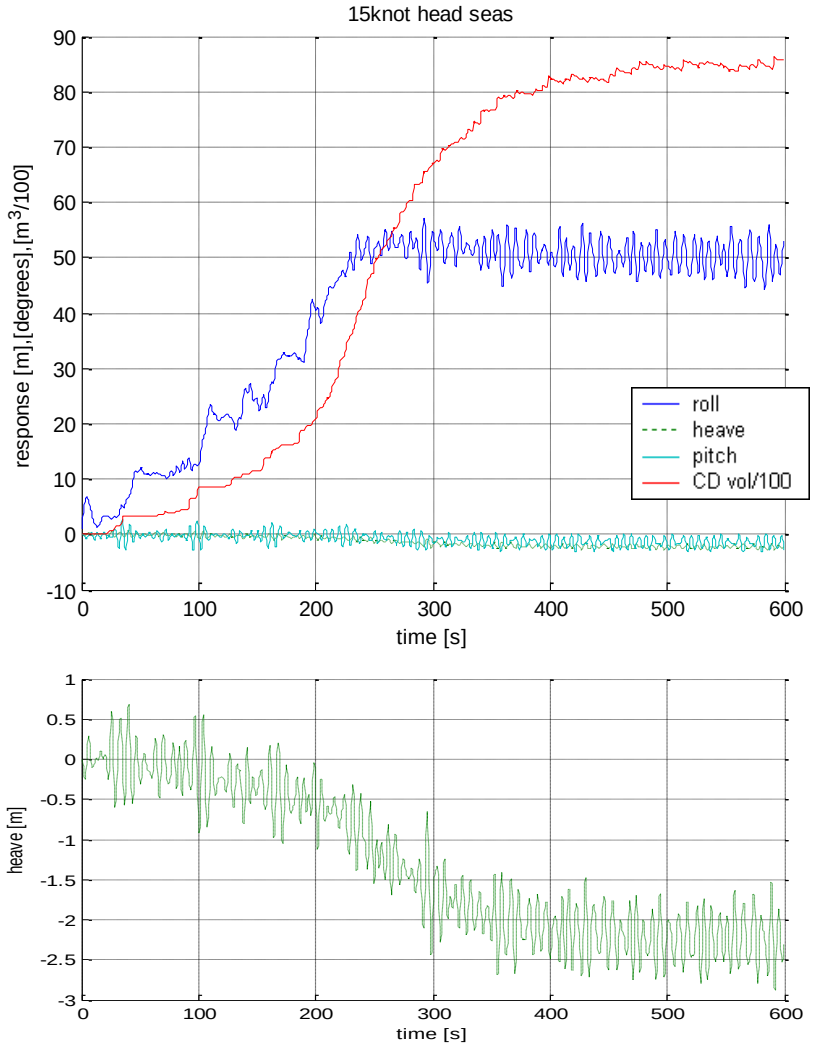

Figure 5-37 Time series of a simulation with 15 knots speed in head seas and full opening of bow ramp at time=20 s. CD is the car deck space. Heave motion in separate lower graph.

The time to flood 5000 tonnes of water on the car deck was collected for each simulation and is presented in Figure 5-38. The trends, increased inflow with increased speed and increased heading angle away from head seas, are the same as in the model tests presented in Allenström and Thorsson (2007). A quantitative comparison is however not meaningful since the setup of the model tests were different; the flooded water was immediately pumped out of the ship and no heel developed during the tests. However in in Allenström (2007) two additional model tests were made, similar to the present simulations, in head waves at 14.5 knots forward speed. These model tests showed that a steady state heel of 46-47° was reached after 3-4 minutes, which shows a reasonable agreement with the corresponding simulation in Figure 5-37 where a steady state heel was reached in close to 4 minutes.

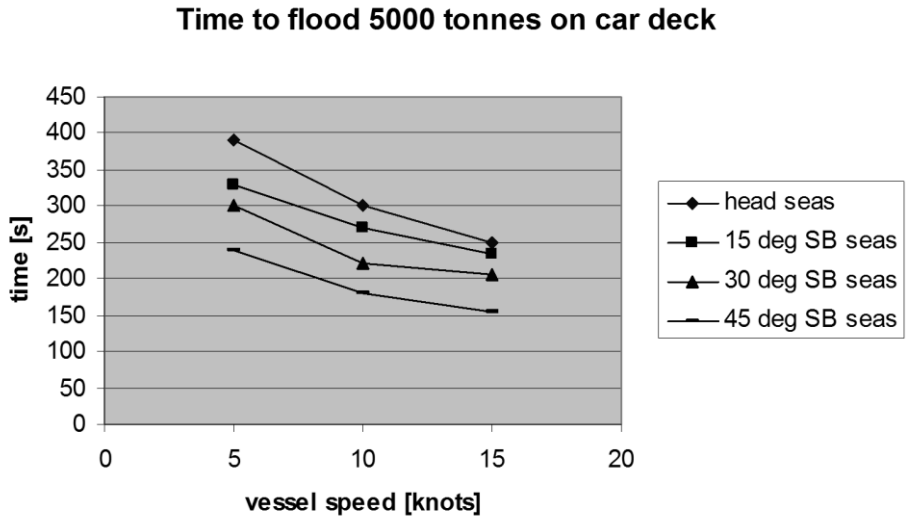

Figure 5-38 Time to flood 5000 tonnes on the car deck for each simulation case.

Final stage flooding simulation

In the initial stage simulations only the car deck was subjected to flooding and the ship reached a steady state of around 50° mean roll without capsize. Prior to this state, however, flooding would have occurred through other openings. At around 40° of heel, with 2500 tonnes of water on the car deck, flooding of the machinery spaces through the starboard side ventilation ducts, additional flooding of the car deck through the supply and exhaust ventilators on deck 4 and flooding of the lower space of the super structure will start. Within about a minute, flooding of all spaces below the car deck through the center casing, will follow. At the start of the final stage flooding simulation the car deck was assumed to be flooded with 2500 tonnes of water accumulated during the turn to port, the ship was at beam seas with zero forward speed and all openings in the model were open to flooding.

At the time of the present simulations progressive flooding had not been implemented in SIMCAP and flooding through the center casing was assumed to be based on the (F-K) wave elevation at the openings rather than the water elevation on the car deck. However, within about a minute after simulation start the floodwater on the car deck will reach these openings and the water level on the car deck will be close to the mean wave elevation, as will the water

levels of the spaces below the car deck, for the remainder of the simulation. It is thus believed that this simplification did not significantly affect the simulation result and did not affect the conclusions.

Figure 5-39 show the time series of a simulated capsize and sinking scenario where the floodwater volumes and the motions of roll and heave are plotted. The volumes of the spaces below deck 2 have been added and are represented by the dashed line. 180° of roll, full capsize, and the abrupt change of heave, when enough buoyancy is lost to sink the ship, is indicated by arrows. Eight instances in time, T0-T7, are indicated by vertical lines. The appearance of the time series and mechanisms of the scenario will be discussed in the following with the aid of snap shots from the simulation at these instances.

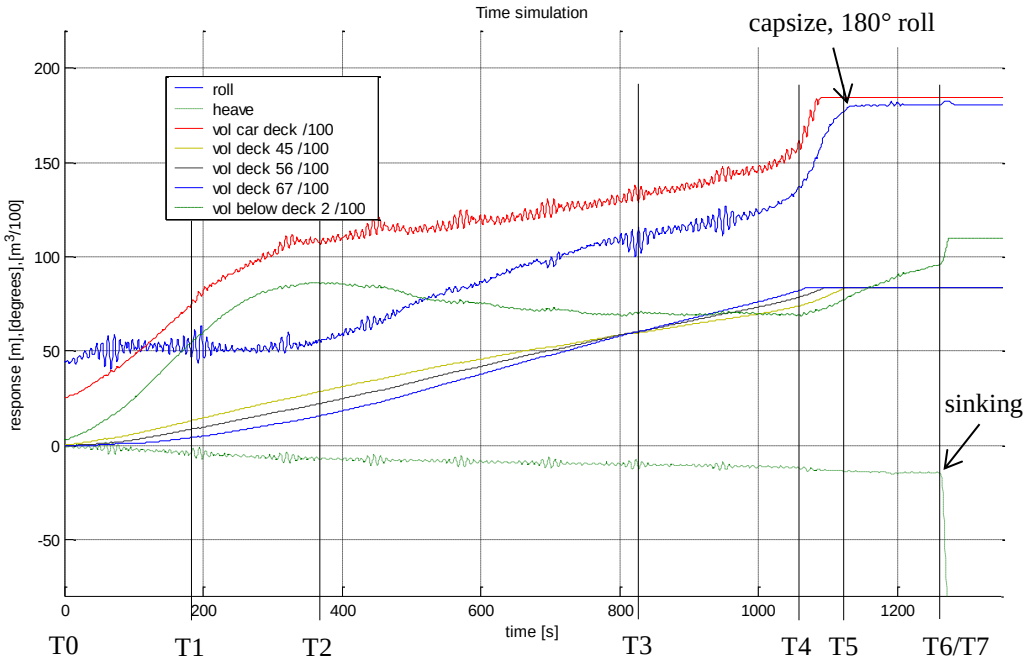

Figure 5-39 Time series of motions and flooding of a capsize and sink scenario. Decks 45, 56, and 67 is the lower, middle and upper space of the super structure respectively.

Figure 5-40 Snap shot of ship at T0, time=0 s (left) and T1, time=193 s.

Figure 5-40: At T0 flooding of deck 45 and the machinery spaces below deck 2 start immediately. The car deck is flooded both through the main ventilators on deck 4 and the bow ramp opening and the water level is close to the mean wave elevation. At T1 the ship is flooded through all floodable openings. There is a counter pressure from the inside on all windows in the super structure. The pressure head difference acting on windows on deck 45 is approximately 4 m and assumed to be too small for further breaking.

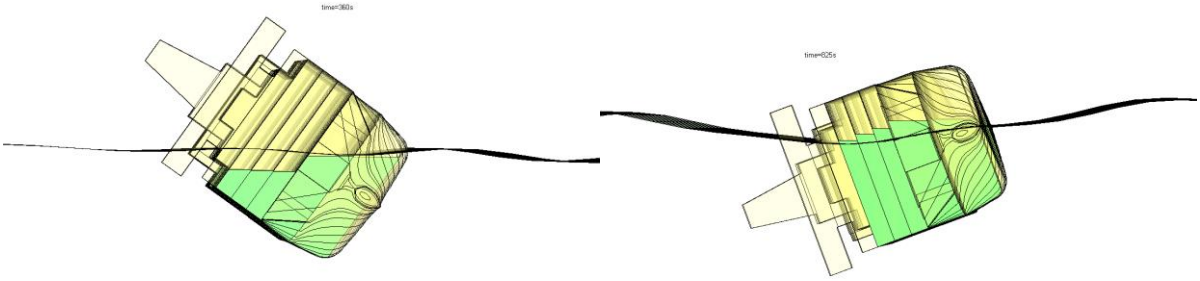

Figure 5-41 Snap shot of ship at T2, time=360 s (left) and T3, time=825 s.

Figure 5-41: At T2 the pressure heads driving the flooding of upper decks are now close to equal due to equal surface elevation within the spaces. The flood rate will be higher on a higher deck as the list increase further. There will be an outflow from the spaces below deck 2 from this point in time and on. As the list increases the lower parts of the ship will be elevated and the pressure heads will be negative. At T3 the flooded volumes of deck 45, 56, and 67 are equal. There is still a decrease of floodwater below deck 2 but the rate of out flow is very small; the elevation of the lower parts with increased list is compensated by the gradual sinking of the ship.

Figure 5-42 Snap shot of ship at T4, time=1060 s (left) and T5, time=1125 s.

Figure 5-42: From T4 and on the flood volume of spaces below deck 2 will increase again. Soon after this time the machinery space ventilation on the port side, below deck 4, will be submerged. This may create an air lock for the below spaces and the air would compress when the spaces are flooded further. The SIMCAP code however do not account for air

compression effect i.e. there is always a free escape of air in the simulations. At T5 all spaces above deck 2 are filled. The pressure head will continue to drive the flooding of spaces below deck 2.

Figure 5-43 Snap shot of ship at T6, time=1263 s (left) and T7, time=1264 s.

Figure 5-43: All reserve buoyancy is gone at T6 and the ship starts to go down to the sea bed. When the ship leaves the surface the simulated heave velocity, sinking speed, is exaggerated due to lack of viscous resistance, Figure 5-39. At T6 the ship have left the surface and the quickly rising pressure head and absence of air compression in the simulation, result in a rapid flooding of the remaining 1700 m^3 of floodable spaces below deck 2.

Summary

The above simulations were made in order to substantiate the scenario deemed as the most probable by the project consortium and in an effort to reveal key physical mechanisms of flooding and capsizing.

The initial stage flooding simulation, with different ship speeds and headings and with flooding through bow ramp opening only, showed a reasonable agreement with comparable model tests. Information about the behavior of the ship in these simulations were used in the setup of the final stage flooding simulations, where the ship was flooded through all openings deemed relevant for the scenario and at beam seas with zero forward speed. In these simulations it was found that the rate of flooding of the superstructure had a very large impact on the list development and that the assumption of two broken windows per deck resulted in a list development conformant to the evidence. Several physical mechanisms of the scenario are discussed and explained through an analysis of the time series of motions and flood volumes together with snap shots of the ship at different instances of a simulation.

The simulations herein cannot be seen as an exact description of the foundering due to both the uncertainties of factual circumstances regarding the accident and limitations in the level of details in the input to the simulations as well as the numerical model itself. The significance of the simulations is rather in the revealing and explaining of the physical mechanisms that can explain and support the possibility of this or a similar scenario.

6 Discussion

The phenomenon of damage stability in a seaway is complex and involves several mechanisms of different nature; the sea keeping problem involving non-linear and transient effects, the flooding mechanism, the behavior of the flooded water etc. In order to obtain a tool that is practical in terms of versatility and computational cost these mechanisms need to be simplified and approximated. Due to the complexity of the resulting numerical tool, evaluation of the impact of each of the adopted approximations would be very difficult, if not impossible. Instead specific scenarios, including all or most of the approximations, are used to validate the tool. Through this approach, the final result of interest, e.g. the time to capsize, time to flood or the amplitude of parametric roll, can be validated. It is clear however that caution is needed if these results are to be generalized to cases different from the specific scenarios of the validations. A few examples, central to the method, of effects that originate from the approximations adopted in SIMCAP and that could be problematic regarding the validity of the tool are discussed in the following.

The linearization of the hydrodynamic problem to obtain the radiation and diffraction forces is an approximation in SIMCAP that is inherited from the classical strip theory, which is well proven to give reasonably accurate results for design purposes and for moderate sea states. The applications of SIMCAP do however go further than standard design cases in terms of both large motions, in e.g. parametric roll assessments, and the list angles in damage simulations where the assumption of starboard/port symmetry is violated and hydrodynamic coupling effects between e.g. heave and roll is expected. Model tests of ship capsize due to water ingress however show that roll motions are significantly decreased and that the capsize process has a quasi-static nature in the final stages, see e.g. ITTC (2000). This suggests that a more accurate modeling of the hydrodynamic properties is not necessary in order to assess capsize events due to flooding.

The flooding mechanism of SIMCAP is a simplistic quasi-stationary approach where the flow is determined through the difference in pressure heads on both sides of the opening and a semi-empirical discharge coefficient which can be determined through model experiments. However, only the elevation of the incident wave is used to obtain the pressure head, disregarding the radiated and diffracted waves and waves generated through forward speed. Despite this simplification, good agreement between model tests and simulations using this approach has previously been reported in e.g. Vassalos et al. (1997).

The treatment of the floodwater within the ship, through the assumption of a horizontal surface, is very basic and the assumption is in principle violated as soon as dynamic effects such as ship motions are present. In a real, physical case of car deck flooding the viscosity will influence the behavior of the floodwater. At early stages of flooding, with a relatively small amount of floodwater, this influence will be significant. At this stage the heeling moment from the floodwater is too small to produce a steady list and the ship can roll from side to side and shallow water effects e.g. hydraulic jump will govern the behavior of the flooded water, which will be quite different from the behavior predicted by SIMCAP. During any stage of flooding the floodwater can be seen as a dynamic system in its own with

resonance properties that could lead to sloshing effects. These effects would not either be captured by SIMCAP. However, regarding the typical low roll resonance frequencies of e.g. RoRo and passenger ships and also the fact that the resonance frequency of the flooded water will be changed as list increases, excitation of the floodwater leading to resonant condition is not likely in pertinent scenarios.

To conclude, the validation studies of the damaged ships in section 4.1 and 4.2 are successful, with high degree of agreement between simulations and model tests, and constitute validation of the quantitative capacity of SIMCAP for assessment of damaged ships in waves. The validation study of parametric roll in section 4.3 shows that the phenomena can be captured by SIMCAP but also that there are large discrepancies between model tests and simulations for some of the test cases. Physical mechanisms behind these discrepancies is investigated and discussed in section 5.2. The qualitative capacity of the tool can be assessed through both the validation studies and the applied studies of chapter 5. It is shown that many physical mechanisms of interest can be captured by SIMCAP. Several of which were expected or sought for e.g. the qualities of the capsize bands and the influence of different parameters on the time to capsize but also a few that were not expected or sought for such as the tendency of a damaged ship to in some occasions get stuck with a list away from the damage, as described in section 5.3, or some qualities in the ship behavior in the parametric roll study in section 5.2. It can also be noted that even if the quantitative capacities of SIMCAP is not fully validated, the tool can be used for e.g. ranking assessments of different scenarios or designs.

Finally it is concluded that SIMCAP is a robust and versatile tool that can be used in many applications in present stage of implementation. There are also opportunities for development of the tool to further increase the applicability and validity. This is discussed in chapter 7.

7 Further work

Future work may include additional case studies similar to the validation and application studies in chapter 4 and 5. It may also include development of the tool; for general strengthening of validity or to include effects that may be present in some specific scenario of interest, such as wind or shallow water effects. Future studies will possibly also include combinations of the above and have the format of validation study followed by a parameter study, like the validation study in section 4.1 followed by the study in section 5.1.

Below follows two lists with examples of case studies and development work, that would be of interest.

Future case studies:

- Ranking study of e.g. different design solutions of water tight subdivision
- Technical accident studies.
- Studies with further statistical analysis of the results e.g. to assess the probabilistic properties of different scenarios e.g. to support development of regulations.
- Additional interdisciplinary studies e.g. continuation of the collaborative work described in section 5.3 or possibly further down in the chain of events; evacuation studies.
- Study of oil spill due to hull damage.
- Link SIMCAP to optimization tool for e.g. optimization of internal subdivision layout with some properties of the capsize band as object functions.

Future development work:

- Fully automated procedure to determine the paths of progressive flooding.
- Inclusion of effects of compressed air in damaged compartments.
- Automatic determination of roll damping coefficients with semi empirical formulations.
- For scenarios where large trim angles could be expected, longitudinal sections on the hull (buttocks or water lines) can be used to calculate the Froude-Krylov force in the ship fixed longitudinal direction and its contribution to the heave force and pitch moment.

- Introduction surge motion where the hydrodynamic coefficients could be estimated through “sway motion” of one or a few buttocks.

- More accurate calculation of the two-dimensional hydrodynamic coefficients.

- Updated hydrodynamic properties due to list and possibly sinkage and trim. Sets of added mass and kernel functions for a few representative floating conditions during a capsize event could be pre-calculated. Further hydrodynamic couplings could be introduced e.g. heave-roll and pitch-roll.

References

ABS. (2004). *Guide for the Assessment of Parametric Roll Resonance in the Design of Container Carriers*. (Updated June 2008). American Bureau of Shipping.

Allenström, B, Thorsson, S. (2007). *Manoeuvring tests and bow ramp flooding tests.* SSPA Report 4006 4100 – 1.

Allenström, B (2007). *Bow ramp flooding tests with complete car deck*. SSPA Report 4006 4100 – 2, May 2007.

Belenky, V., de Kat, J. O., Umeda, N. (2008). *Toward Performance-Based Criteria for Intact Stability.* Marine Technology, **45**(2): 101-123.

Brunswig, J., Pereira, R., Daewoong, K. (2006) *Validation of parametric Roll Motion Predictions for a Modern Container Ship Design.* Proc. 9th Int. Conference on Stability of Ships and Ocean Vehicles, Rio de Janeiro, Brazil.

Bergholtz, J, Rutgersson, O, Schreuder, M. (2008). *WP2.1 Review of evidence Report No. 2 Conceivable course of events*. Department of Shipping and Marine Technology, Chalmers, Technical Report.

Bulian, G., Francescutto, A. (2008). *Theoretical Prediction and Experimental Verification of Multiple Steady States for Parametric Roll.* Proc. 10th Int. Ship Stability Workshop, Daejeon, Korea.

Cummins, W.E. (1962). *The Impulse Response Function and Ship Motions*, Schiffstechnik, Vol. 9.

Faltinsen, O. M. (1990). *Sea Loads on Ships and Offshore Structures*. Cambridge, UK, Cambridge University Press. ISBN 0-521-45870-6.

Fossen, T. I. (2005). *A Nonlinear Unified State-Space Model for Ship Maneuvering and Control in a Seaway.* Journal of Bifurcation and Chaos.

Gao, Z., Gao, Q., Vassalos, D., (2011). *Numerical Simulation of Flooding of a Damaged Ship.* Ocean Engineering, **38**, 1649-1662.

Hogström, P. (2012). *RoPax Ship Collision – a Methodology for Survivability Analysis.* PhD Thesis, Chalmers University of Technology.

Hogström, P., Ringsberg, J., (2012). *An extensive study of a ship's survivability after collision – A parameter study of material characteristics, non-linear FEA and damage stability analyses.* Marine Structures, Volume 27, Issue 1, Pages 1-28

Hua, J., Palmquist, M. (1995). *A Description of SMS – A Computer Code for Ship Motion Simulation.* KTH, TRITA-FKT, Report 9502, ISSN 1103-270X, Stockholm, Sweden.

Hua, J., Palmquist, M., and Lindgren, G. (2006). *An Analysis of the Parametric Roll Events Measured Onboard the PCTC AIDA.* Proc. of the 9th Int. Conference on Stability of Ships and Ocean Vehicles, Rio de Janeiro, Brazil.

ITTC. (2002). *Specialist committee for the prediction of extreme motions and capsizing*. *Final report and recommendations to the 23rd ITTC.* Proceedings of the 23rd ITTC. Jersey City, New Jersey, U.S.A. The Society of Naval Architects and Marine Engineers. 2:619-748. International towing tank committee.

ITTC (2008). *The Specialist Committee on Stability in Waves—Final Report and Recommendations to the 25th ITTC*. Proc. 25th ITTC, vol II, Fukuoka, Japan.

ITTC (2011). *The Specialist Committee on Stability in Waves—Final Report and Recommendations to the 26th ITTC*. Proc. 26th ITTC, vol II, Rio de Janeiro, Brazil.

The Joint Accident Investigation Commission of Estonia, Finland and Sweden (JAIC). (1997). *Final Report on the Capsizing on the 28 September 1994 in the Baltic Sea of the Ro-Ro Passenger Vessel m/v ESTONIA.* Edita Ltd.

Jasionowski, A., Vassalos, D. (2001). *Numerical Modelling of Damage Ship Stability in Waves.* Proceedings of the 6th International Ship Stability Workshop, Trieste, Italy.

Jasionowski, A., Vassalos, D. and Guarin, J. (2003). *Time based survival criteria for passenger Ro-Ro vessels*. SNAME Marine Technology **40**(4): 278-287.

Journeé, J.M.J., (1993). *Hydromechanic Coefficients for Calculating Time Domain Motions of Cutter Suction Dredges by Cummins Equation*. Report 968, Delft University of Technology.

Journée, J.M.J., Adegeest L.J.M. (2003). *Theoretical Manual of Strip Theory Program "SEAWAY for Windows"*. Report 1370, Delft University of Technology.

de Kat, J. O., Brouwer, R., McTaggart, K. A., Thomas, W. L. (1994). *Intact Ship Survivability in Extreme Waves: New Criteria from a Research and Navy Perspective.* Proc. 5th Int. Conference on Stability of Ships and Ocean Vehicles, Vol. 1, Florida, USA.

de Kat, J. O., Kanerva, M., van't Veer, R., Mikkonen, I. (2000). *Damage Survivability of a New Ro-Ro Ferry.* Proceedings of the 7th International Conference on Stability of Ships and Ocean Vehicles, Launceston, Australia.

de Kat, J. O., Paulling, J. R. (2001). *Prediction of Extreme Motions and Capsizing of Ships and Offshore Marine Vehicles,* Proceedings of OMAE 2001 Conference, The 20th International Conference on Offshore Mechanics and Arctic Engineering, Rio de Janeiro, Brazil, 3-8 June.

Källström, C., Allenström, B., Ottosson, P., Vassalos, D., Jasionowski, A., Rutgersson, O., Schreuder, M., Bergholtz, J., Blok, J.J. and van Daalen, E.F.G., (2008). *Final Report-Research Study on the Sinking Sequence of MV Estonia,* Göteborg Sweden. SSPA Research Report No. 134, ISBN 91-86532-47-2.

Lewandowski, E. M. (2004). *The Dynamics of Marine Craft: Maneuvering and Seakeeping.* Advanced series on Ocean Engineering – Vol. 22, World Scientific.

Lloyd, A .R. J. M. (1989). *Seakeeping: Ship Behaviour in Rough Wheather*, Ellis Horwood Limited, Southhampton, Great Britain.

Matusiak, J. (2003). *On the effects of wave amplitude, damping and initial conditions on the parametric roll resonance.* Proc. 8th Int. Conference on Stability of Ships and Ocean Vehicles, Madrid, Spain.

MSC (2008a). *FSA – RoPax ships*, MSC 85/17/2, IMO, Maritime Safety Committee.

MSC (2008b). *FSA – RoPax ships: Details of the Formal Safety Assessment,* MSC 85/INF.3, IMO, Maritime Safety Committee.

Neves, M.A.S., Rodriguez, C.A., and Vivanco, J.E.M. (2009). *On the limits of stability of ships rolling in head sea.* Proc. IMechE Vol. 223 Part M: Journal of Engineering for the Maritime Environment.

Newman, J.N. (1977). *Marine Hydrodynamics*, MIT press.

Paulling, J.R. (2006). *Parametric Rolling of Ships – Then and Now.* Proc. of the 9th Int. Conference on Stability of Ships and Ocean Vehicles, Rio de Janeiro, Brazil.

Rask, I., (2010). *Benchmark data on time to capsize for a free drifting model*. E.U. research project FLOODSTAND, D4.1a, FP7-RTD- 218532.

Ruponen, P. (2006). *Model Tests for the Progressive Flooding of a Box-Shaped Barge*, Helsinki University of Technology, Ship Laboratory, Report M-292, 88 p.

Ruponen, P., Kurvinen, P., Saisto, I., Harras, J. (2010). *Experimental and Numerical Study on Progressive Flooding in Full-Scale.* Transactions RINA, Vol 152, Part A4, International Journal of Maritime Engineering.

Rutgersson, O., Schreuder, M., Bergholtz, J. (2006). *WP2.1 Review of evidence and forming of loss hypothesis*. Department of Shipping and Marine Technology, Chalmers, Technical Report.

Råde, L., Westergren, B. (1988). *BETA - Mathematics Handbook.* Studentlitteratur, Lund, Sweden, ISBN 91-44-25052-5

SAFEDOR (2005-2009). *Design, Operation and Regulation for Safety.* Integrated project funded by the European Commission, Project No. IP-516278.

Salvesen, N., Tuck, E.O., Faltinsen, O. (1970). *Ship Motions and Sea Loads.* SNAME Transactions, Vol 78.

Santos, T. A., Guades Soares, C. (2003) *Investigation into the Effects of Shallow Water on Deck on Ship Motions.* Proc. 8th Int. Conference on Stability of Ships and Ocean Vehicles, Madrid, Spain.

Schreuder, M. (2005). *Time simulation of the behaviour of damaged ships in waves*. Shipping and Marine Technology. Gothenburg, Sweden. Chalmers University of Technology. Licentiate Thesis.

Schreuder, M. (2008). *WP4.1-4.3 Numerical simulations of foundering scenarios*. Department of Shipping and Marine Technology, Chalmers, Technical Report.

Schreuder, M., Hogström, P., Ringsberg, J., Johnson, E., Janson, C-E. (2012). *A Method for Assessment of the Survival Time of a Ship Damaged by Collision.* Transactions - Society of Naval Architects and Marine Engineers, **119**(1), 603-619.

Soares, D.G., Jasionowski, A., Jensen, J., McGeorge, D., Papanikolaou, A.D., Pöyliö, E., Sames, P., Skjong, R., Skovbakke Juhl, J. and Vassalos, D. (2009). *Risk-based ship design*. Editor: Papanikolaou, A. D. Berlin Heidelberg, Germany. Springer-Verlag.

Spanos, D., Papanikolaou, A. (2001) *Numerical study of the damage stability of ships in intermediate stages of flooding*, Proceedings of the 5th International Ship Stability Workshop, Trieste, Italy.

Spanos, D., Papanikolaou, A. (2007). *On the Time to Capsize of a Damaged RoRo/Passenger Ship in Waves*, Proceedings of the 9th International Ship Stability Workshop, Hamburg, Germany.

Spanos, D., Papanikolaou, A. (2009a). *SAFEDOR International Benchmark Study on Numerical Simulation Methods for the Prediction of Parametric Rolling of Ships in Waves.* NTUA-SDL Report Rev 1.0.

Spanos, D., Papanikolaou, A. (2009b). *Benchmark Study on Numerical Simulation Methods for the Prediction of Parametric Roll of Ships in Waves*. Proc. 10th Int. Conference on Stability of Ships and Ocean Vehicles, St Petersburg, Russia

Spanos, D. and Papanikolaou, A. (2011). *Numerical simulations for characterizing Time to Capsize.* E.U. research project FLOODSTAND, D4.3, FP7-RTD- 218532

Tagg, R. and Tuzcu, C. (2003). *A performance-based assessment of the survival of damaged ships: final outcome of the EU research project HARDER*. SNAME Marine Technology **40**(4): 288-295.

Turan, O. (1993). *Dynamic Stability Assessment of Damaged Passenger Ships Using a Time Simulation Approach*. PhD Thesis, Department of Ship and Marine Technology, University of Strathclyde, Glasgow.

Umeda, N. et al. (2008). *Comparison Study on Numerical Prediction Techniques for Parametric Roll.* Proc. Of the 27th Symposium on Naval Hydrodynamics, Seoul, Korea.

Van't Veer, R., de Kat, J., Cojeen, P., (2004). *Large Passenger Ship Safety: Time to Flood Simulations.* Marine Technology, Vol. 41, No. 2, pp.82-87.

Vassalos, D., Turan, O. (1994). *A Realistic Approach to Assessing the Damage Survivability of Passenger Ships.* Transactions of the Society of Naval Architects and Marine Engineers 102, pp 367-394.

Vassalos, D., Conception, G., Letizia, L. (1997). *Modelling the Accumulation of Water on the Vehicle Deck of a Damaged Vessel.* Proc. 3rd Int. Ship Stability Workshop, Hersonissos, Greece.

Vidic-Perunovic, J., & Jensen, J. J. (2009). *Parametric roll due to hull instantaneous volumetric changes and speed variations*. Ocean Engineering, Vol. 36(12-13), pp 891-899.

Zaraphonitis, G., Papanikolaou, A. D., Spanos, D. (1997). *On a 3-D Mathematical Model of the Damage Stability of Ships in Waves*. Proc. 6th Int. Conference on Stability of Ships and Ocean Vehicles, Varna, Bulgaria.

Appendix 1

The calculation of the 3-D hydrodynamic coefficients in SIMCAP is done either following the ordinary strip theory (OST) or the modified strip theory (MST), as presented in Journée and Adegeest (2003). OST and MST only differ in respect to how forward ship is handled. In the equations below OST is present when the boxed terms are excluded and MST when they are included. In both methods forward speed is accounted for through the convection of momentum along the length of the ship, but at different levels of mathematical detail, Salvesen et al. (1970). As a result, the effect of forward speed is only present in the off-diagonal terms of the damping matrix for OST. OG=KG-d, U=ship speed, x is herein the coordinate in the ship fixed system. a_{ij} and b_{ij} are the sectional 2-D hydrodynamic coefficients and are obtained through an in-house code (Hua and Palmqvist 1995) where the Lewis conformal mapping technique is utilized. a_{ij} and b_{ij} are calculated in a co-ordinate system with the origin at the center line and at the still water surface of the intact ship. A correction is needed for the transformation to a system with origin at the center of gravity of the ship, at the distance OG.

$$A_{33} = \int_L a_{33}\, dx$$

$$A_{35} = -\int_L x \cdot a_{33}\, dx + \boxed{\frac{-U}{\omega_e^2}\int_L b_{33} dx}$$

$$A_{53} = -\int_L x \cdot a_{33}\, dx + \boxed{\frac{U}{\omega_e^2}\int_L b_{33} dx}$$

$$A_{55} = \int_L x^2 \cdot a_{33}\, dx + \boxed{\frac{U^2}{\omega_e^2}\int_L a_{33} dx}$$

$$A_{22} = \int_L a_{22}\, dx$$

$$A_{24} = \int_L a_{24}\, dx + OG\int_L a_{22}\, dx$$

$$A_{42} = \int_L a_{42}\, dx + OG\int_L a_{22}\, dx$$

$$A_{26} = \int_L x \cdot a_{22}\, dx + \boxed{\frac{U}{\omega_e^2}\int_L b_{22} dx}$$

$$A_{62} = \int_L x \cdot a_{22}\, dx + \boxed{\frac{-U}{\omega_e^2}\int_L b_{22} dx}$$

$$A_{44} = \int_L a_{44}\,dx + 2 \cdot OG \int_L a_{42}\,dx + OG^2 \int_L a_{22}\,dx$$

$$A_{46} = \int_L x \cdot a_{42}\,dx + OG \int_L x \cdot a_{22}\,dx + \boxed{OG\frac{U}{\omega_e^2}\int_L b_{22}dx + \frac{U}{\omega_e^2}\int_L b_{24}dx +}$$

$$A_{64} = \int_L x \cdot a_{24}\,dx + OG \int_L x \cdot a_{22}\,dx + \boxed{\frac{-U}{\omega_e^2}\int_L b_{24}dx - OG\frac{U}{\omega_e^2}\int_L b_{22}dx}$$

$$A_{66} = \int_L x^2 \cdot a_{22}\,dx + \boxed{\frac{U^2}{\omega_e^2}\int_L a_{22}dx}$$

$$B_{33} = \int_L b_{33}\,dx$$

$$B_{35} = -\int_L x \cdot b_{33}\,dx + U \int_L a_{33}\,dx$$

$$B_{53} = -\int_L x \cdot b_{33}\,dx - U \int_L a_{33}\,dx$$

$$B_{55} = \int_L x^2 \cdot b_{33}\,dx + \boxed{\frac{U^2}{\omega_e^2}\int_L b_{33}dx}$$

$$B_{22} = \int_L b_{22}\,dx$$

$$B_{24} = \int_L b_{24}\,dx + OG \int_L b_{22}\,dx$$

$$B_{42} = \int_L b_{42}\,dx + OG \int_L b_{22}\,dx$$

$$B_{26} = \int_L x \cdot b_{22}\,dx - U \int_L a_{22}\,dx$$

$$B_{62} = \int_L x \cdot b_{22}\,dx + U \int_L a_{22}\,dx$$

$$B_{44} = \int_L b_{44}\,dx + 2 \cdot OG \int_L b_{24}\,dx + OG^2 \int_L b_{22}\,dx$$

$$B_{46} = \int_L x \cdot b_{42}\, dx - U \int_L a_{42}\, dx + OG \int_L x \cdot b_{22}\, dx - OG \cdot U \int_L a_{22} dx$$

$$B_{64} = \int_L x \cdot b_{24}\, dx + U \int_L a_{24}\, dx + OG \int_L x \cdot b_{22}\, dx + OG \cdot U \int_L a_{22} dx$$

$$B_{66} = \int_L x^2 \cdot b_{22}\, dx + \boxed{\frac{U^2}{\omega_e^2} \int_L b_{22} dx}$$

Appendix 2

This appendix contains the derivation of the equations in (3.20). Regular waves have been used in the derivations and irregular waves can be obtained through superposition without loss of validity. The figure below show an effective section, in beam seas, with draught d_e and half beam b_e.

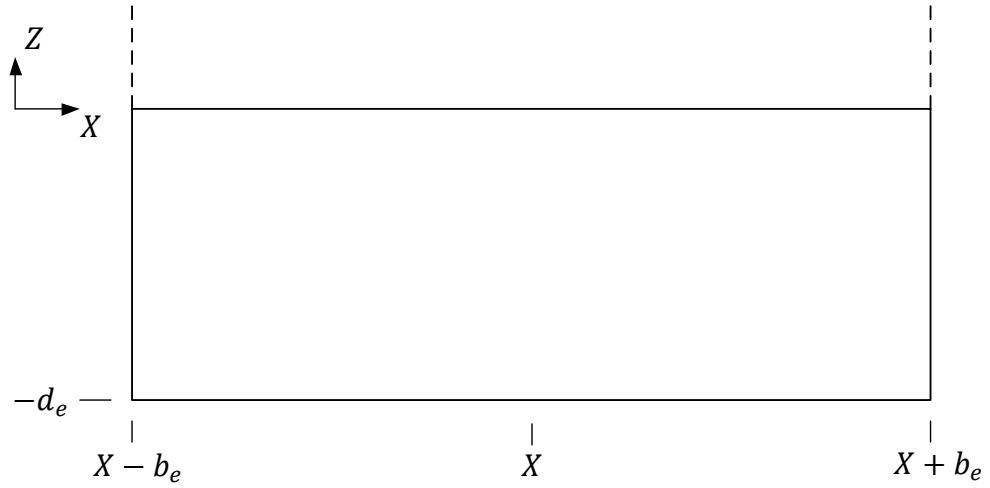

Assuming beam seas the horizontal acceleration components of the incident wave at the two vertical boundaries of the section are:

$$\hat{\xi}\omega^2 \, e^{kZ} \sin(k(X \pm b_e) - \omega t)$$

and the spatial mean value is:

$$\bar{a}_h = \frac{\hat{\xi}\omega^2}{d_e} \int_{-d_e}^{0} e^{kZ} \cdot dZ \cdot \left(\frac{\sin(k(X - b_e) - \omega t) + \sin(k(X + b_e) - \omega t)}{2} \right)$$

$$= \frac{\hat{\xi}\omega^2}{2 \cdot d_e} \left[\frac{e^{kZ}}{k} \right]_{-d_e}^{0}$$

$$\cdot [\sin(kX - \omega t) \cos kb_e - \cos(kX - \omega t) \sin kb_e + \sin(kX - \omega t) \cos kb_e$$

$$+ \cos(kX - \omega t) \sin kb_e] = \frac{\hat{\xi}\omega^2}{2 \cdot d_e} \cdot \frac{1 - e^{-kd_e}}{k} [2 \sin(kX - \omega t) \cos kb_e]$$

$$= \frac{1 - e^{-kd_e}}{k \cdot d_e} \cdot \cos kb_e \cdot \hat{\xi}\omega^2 \sin(kX - \omega t) = \frac{1 - e^{-kd_e}}{k \cdot d_e} \cdot \cos kb_e \cdot a_h$$

For a general heading angle b_e and a_h shall be scaled by $\sin(\mu + \eta_6)$, see figure below, and thus we arrive at the first equation of (3.20).

Assuming beam seas the vertical acceleration component of the incident wave at the horizontal boundary of the section is:

$$-\omega^2\hat{\xi}e^{kZ}\cos(kX-\omega t)$$

with a spatial mean value of:

$$\begin{aligned}\bar{a}_v &= \frac{-\omega^2\hat{\xi}e^{-kd_e}}{2\cdot b_e}\int_{X-b_e}^{X+b_e}\cos(kX-\omega t)\cdot dX = \frac{-\omega^2\hat{\xi}e^{-kd_e}}{2\cdot b_e}\left[\frac{\sin(kX-\omega t)}{k}\right]_{X-b_e}^{X+b_e}\\ &= \frac{-\omega^2\hat{\xi}e^{-kd_e}}{2\cdot kb_e}[\sin(k(X+b_e)-\omega t)-\sin(k(X-b_e)-\omega t)]\\ &= \frac{-\omega^2\hat{\xi}e^{-kd_e}}{2\cdot kb_e}[\sin(kX-\omega t)\cos kb_e+\cos(kX-\omega t)\sin kb_e\\ &-(\sin(kX-\omega t)\cos kb_e-\cos(kX-\omega t)\sin kb_e)]\\ &= \frac{-\omega^2\hat{\xi}e^{-kd_e}}{2\cdot kb_e}[2\cos(kX-\omega t)\sin kb_e]\\ &= e^{-kd_e}\cdot\frac{\sin kb_e}{kb_e}\cdot\left(-\omega^2\hat{\xi}\cos(kX-\omega t)\right) = e^{-kd_e}\cdot\frac{\sin kb_e}{kb_e}\cdot a_v\end{aligned}$$

For a general heading angle b_e shall be scaled by $\sin(\mu+\eta_6)$, see figure below, and thus we arrive at the second equation of (3.20).

The figure below show a top view of an effective section (bold line) in a general heading angle $\mu+\eta_6$. Here a_h from the first derivation is projected in-plane of the section and b_e from both derivations is projected in-plane of the wave propagation. Thus the two derivations are extended to hold for general heading angles.

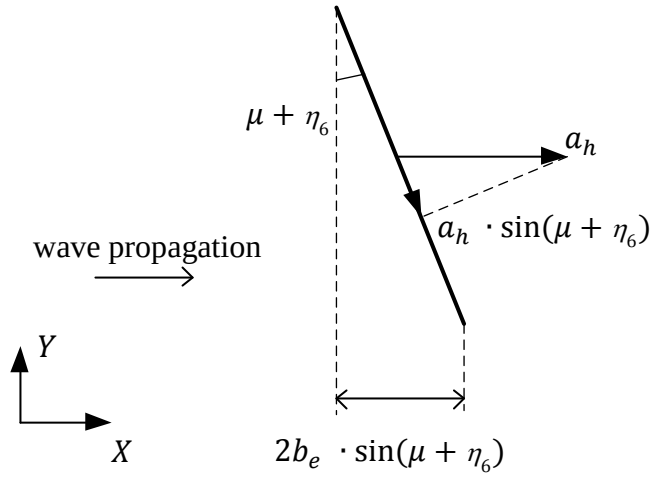

The derivation of the third and fourth equation of (3.20) will be similar.